Politecnico di Torino

Politecnico di Torino

MSc in Automotive Engineering

A.A. 2023/2024

July 2024

3D-CFD Simulation methodologies for the assessment of HVAC aeroacoustics performance

Supervisors

Prof. Federico MILLO

Andrea BIANCO

Paolo BIGLIANI

Candidate

Vito Francesco LAGRAVINESE

Abstract

With the advent of electrification as a continuously growing trend in the automotive industry, unprecedented changes are shaping the vehicle evolution. The new concepts at the basis of vehicle design not only follow the transition towards a sustainable mobility, but lead also to major changes in user experience and comfort inside the vehicle. The electrification changed completely the spectrum of noise emissions from vehicles and tractors, cutting-off all the engine-related noises. The noise reduction presents a unique opportunity to delve deeper into the study of aeroacoustics phenomena, to better understand their impact on the cabin occupants and the driving or working experience. With a major noise source switched off, other noises unveil themselves, as for example the ones coming from the Heating, Ventilation, and Air Conditioning (HVAC) system, and could cause significant disturbances inside the cabin.

Especially in tractors and industrial vehicles, it is crucial to provide a high comfort level. Computer Aided Engineering (CAE) becomes crucial in the investigation of aeroacoustics phenomena during vehicle development, when physical prototypes are not yet available but possible noise sources and countermeasures can be identified through 3D-CFD analysis, which in this project is performed with Simcenter Star-CCM+. The aim of this thesis, which was carried out in GammaTech Engineering in collaboration with CNH-Industrial, is to investigate proper methodologies to predict noise generation and propagation in HVAC ducts, exploring a wide range of possibilities, from direct noise computation to hybrid methods that are capable of decoupling aerodynamics and acoustics.

More in detail, a simplified HVAC duct geometry, for which experimental data were available from literature, was analysed with different simulation strategies. At first, the Direct Noise Computation (DNC) method was adopted to assess the capability of the 3D-CFD methodology to correctly reproduce experimental data, using the most detailed numerical approach available. In this context, the DNC led to results in good agreement with experimental evidence. Then, the project shifted the focus on the adoption of hybrid methods, with the aim to describe the aeroacoustics behaviour in the far-field, and obtaining a significant reduction of simulation time and computational effort. Both the hybrid methods, based on Lighthill model and Perturbed Convective Wave model, provided an important speed up during simulations, and led to results showing good agreement with experimental ones in terms of Sound Pressure Level (dB) in the far-field.

Table of Contents

List of Tables

List of Figures

Symbols

APE

Acoustic Perturbation Equation

BEV

Battery Electric Vehicles

CAA

Computational Aeroacoustics

CAE

Computer Aided Engineering

CFD

Computational Fluid Dynamics

DES

Detached Eddy Simulation

DNC

Direct Noise Computation

EEA

European Environment Agency

EU

European Union

EV

Electric Vehicles

GHG

Greenhouse Gases

HPC

High Performance Computing

HVAC

Heating, Ventilation and Air Conditioning

ICE

Internal Combustion Engine

IEA

International Energy Agency

ISO

International Organization for Standardization

LES

Large Eddy Simulation

OEM

Original Equipment Manufacturer

PCW

Perturbed Convective Wave

PIV

Particle Image Velocimetry

RANS

Reynolds Averaged Navier-Stokes

TVB

Total Variation Bounded

Chapter 1

Introduction

1.1 Mobility status, challenges and future trends

At current days, the landscape of mobility has undergone a shift towards sustainable transition, moved by urbanisation trends, environmental imperatives, and the needs to overcome the fossil fuels dependency. The climatic crisis is significantly propelled by domestic transportation sector which, according to European Environment Agency (EEA) [1], is responsible for more than 20% of the EU's total greenhouse gas (GHG) emissions, as figure 1.1 illustrates.

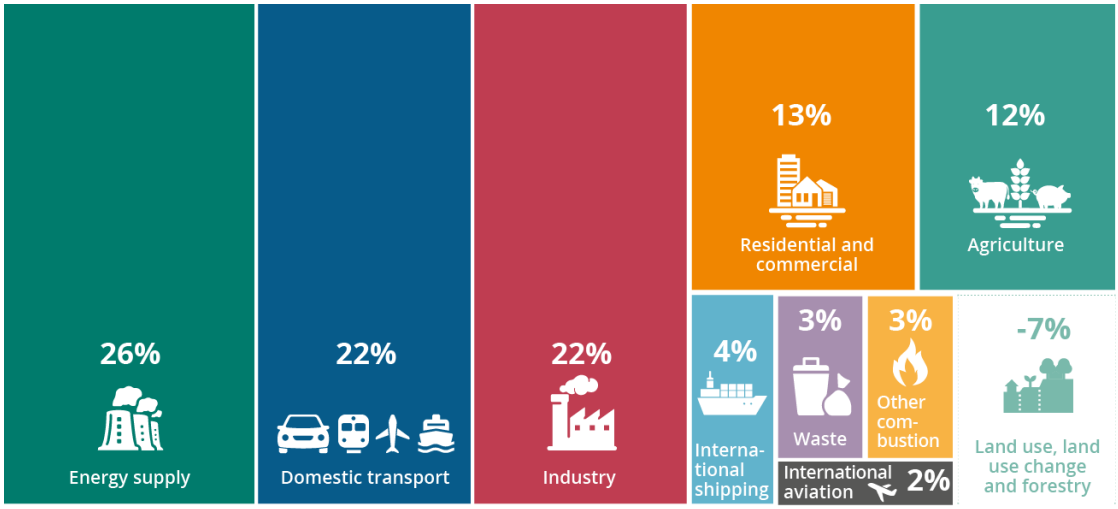

Figure 1.1: Shares of GHG emissions updated at 29 Aug 2023 from [2]

Most cities are affected by congestion, air pollution and noise pollution, which are detrimental not only for the environment but also for people and their quality

of life. To give an extent of the actual situation, the EEA refers that the passenger transport increased by almost 21% between 2000 and 2019, with the passenger car as the main transport mode for a share of 60.6% of the entire road transport sector, as can be observed in figure 1.2.

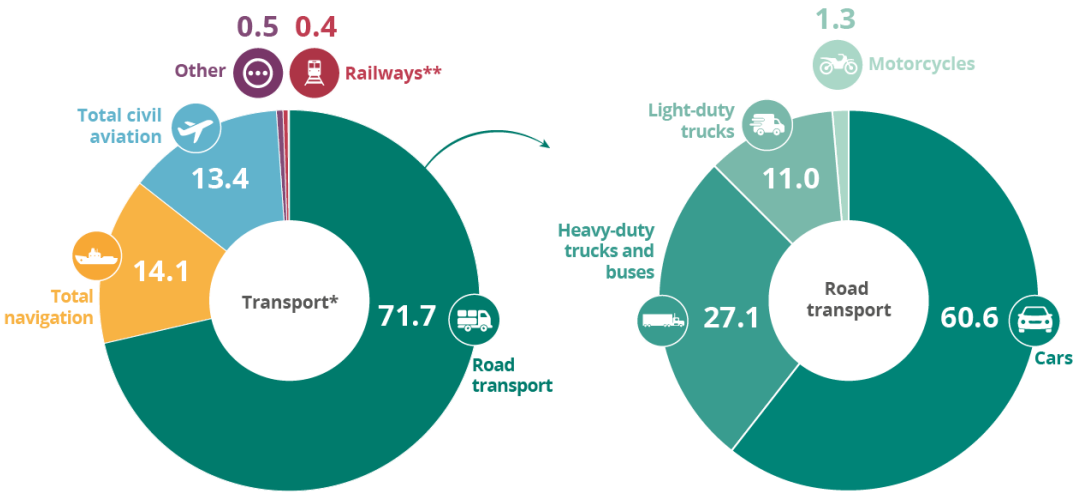

Figure 1.2: Shares of road transports GHG emissions updated at 29 Aug 2023 from [2]

This growth led directly to an increase in exhaust emissions and noise pollution, with the latter as a major cause for chronical high level of annoyance for 18.4 million people [1]. The most recent data available were from 2017, when more than 95 million people were exposed to road traffic noise levels of at least 55 dB in on daily basis, as it can be observed in figure 1.3. The cited report [1] expects that for 2030 the share of people impacted by transport noise should be reduced by 30% compared to 2017.

According to most researchers, institutions, Original Equipment Manufacturers (OEMs) and customers, it is necessary to accelerate the transition towards the mobility of the future, characterized by a more efficient commuting network, electric vehicles and alternative fuels, since the actual transportation sector is not sustainable on the long run. Shifting towards a more sustainable mobility, especially from the tank-to-wheel perspective, it has put the focus of researchers and OEMs on Battery Electric Vehicles (BEV). The "Global Electric Vehicles Outlook 2024" form the International Energy Agency (IEA) [2] refers that around 14 million electric vehicles were sold in 2023, amounting for the 18% of the new cars that have been sold during the year. Morover, the same report expects a further growth in 2024, up to 17 millions of new electric vehicles on the roads. In figure 1.4 it is

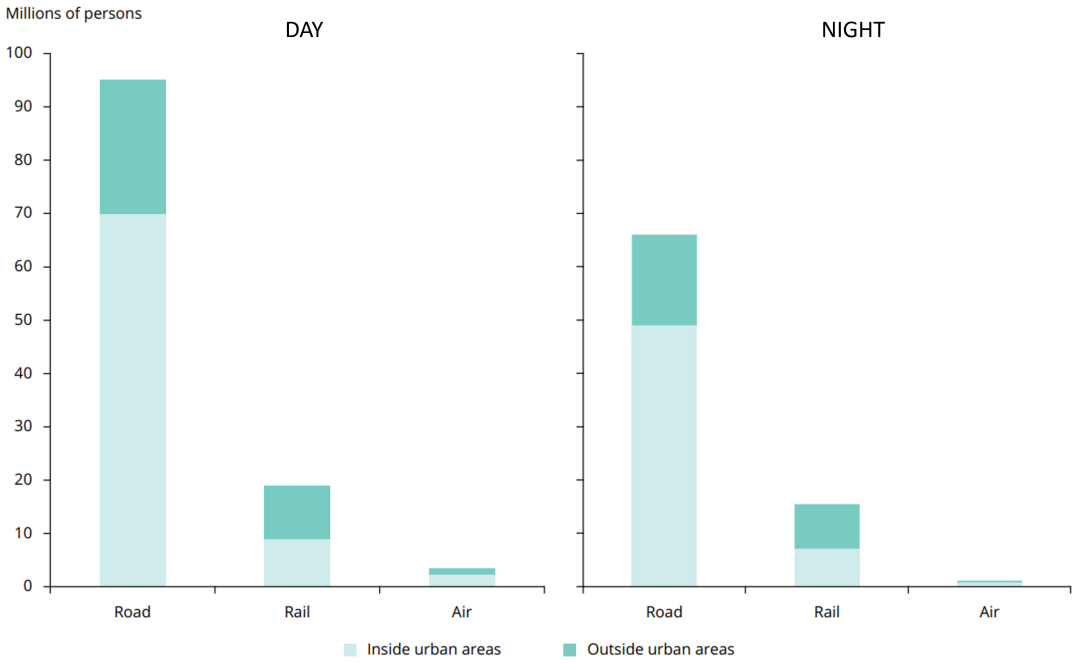

Figure 1.3: Estimated number of people exposed to unhealthy noise levels from transport in EU in 2017 (day on left, night on right) from [1]

possible to compare the sales of electric car between China, US, EU, and the rest of the world.

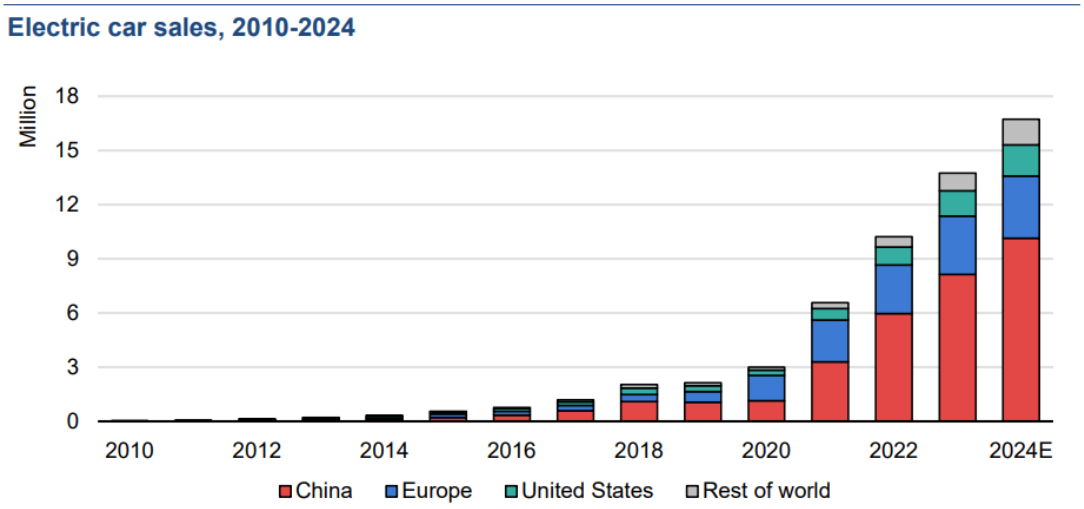

Figure 1.4: Electric cars sales, 2010-2023 from [3]

The growing diffusion of electric vehicles has a direct effect not only on the production processes but also on the research and development sector, because the EVs bring with them specific necessities related to the propulsion systems, which indirectly acts on the other fields of the vehicle design. Among many technological innovations and subsequent effects that come with electric vehicles, the vehicle noise mitigation is the major interest for this thesis project. In fact, the introduction of electric motors in place of Internal Combustion Engines (ICEs), has led to a major reduction in vehicle noise production, both outside and inside the cabin.

New electrical vehicles and tractors are featured with improved noise insulations from the outside but, considering the subsequent absence of internal combustion engines, HVAC sounds have now taken the lead inside the cabin and are crucial in the design process. When dealing with interior vehicle noise at design stages, it is necessary to follow the International Organization for Standardization (ISO) rules. Specifically, the ISO 5128:2024 [4] regulates the acoustics measurements of interior vehicle noise, especially in terms of noise exposure over time and its effects on driver distraction or fatigue. Therefore, from a production point of view, it is necessary to provide compliancy with standards since the early design stages, to guarantee proper level of acoustic comfort to the cabin occupant. For this purpose, the 3D-CFD simulation in the aeroacoustics field helps in assess the noise issue and predict the dB values reached inside the cabin.

1.2 3D-CFD state-of-the-art for aeroacoustics analysis

To understand how the noise develops in HVAC systems, it is of paramount importance to properly comprehend how the airflow behaves inside the system cavities, ducts, and rotating parts. Figure 1.5 presents a simplified layout of an HVAC system for a passenger car from Tautz [5]. The air intake system conveys both the flows from the outside and from the recirculating system into a fan, which pushes the flow through a diffuser and, downstream of it, the HVAC unit is located. According to the needs, the HVAC unit is capable of providing cool or hot air inside the vehicle cabin, through the air outlets. The picture shows throttle flaps (coloured in red) and the impeller (coloured in green) which can be distinguished as the components with major responsibilities in noise generation inside the system. The thesis project moves towards this direction, with the aim to investigate one of the noise sources of the system, which is a simplified version of an air outlet with a flap, and its acoustic emission levels in terms of Sound Pressure Level (SPL).

Experimental measurements and Computer-Aided Engineering (CAE) moves in parallel towards this purpose, giving the possibility to predict and verify the airflow behaviour inside the system. CAE related to the fluid dynamics, known

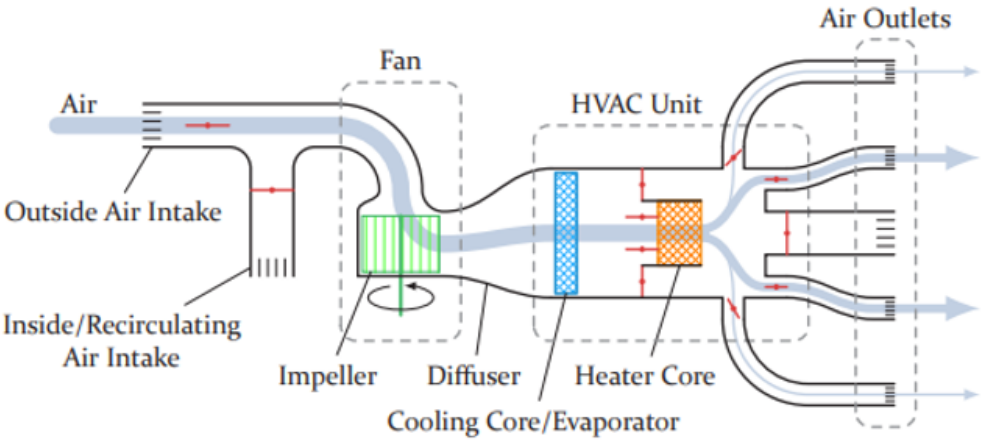

Figure 1.5: Simplified HVAC system layout from [5]

as Computational Fluid Dynamics (CFD) has evolved rapidly during years, in parallel with the availability of faster and powerful computational architectures. The importance of CFD (and CAE in general) in design stages has grown through years, thanks to an always improving accuracy and reliability of the simulations, which help in reducing the number of prototypes and test phases, thus reducing costs, and speeding the entire process up. The immediate effect of these aspects is a faster implementation of design improvements, which can increase the quality of the product. The growth of 3D-CFD has also impacted the aeroacoustics analysis, with the development of new and uprising methodologies completely dedicated to the noise investigation, known as Computational Aeroacoustics (CAA), which is crucial to investigate the phenomena developing inside the HVAC systems. To introduce the thesis project, it is necessary to present an overview of the state-of-the-art of 3D-CFD aeroacoustics analysis and to introduce the most recent studies on the matter, which have been taken as benchmark for the methodology proposed in the following dissertation.

The thesis project follows the researchers work carried out by a consortium of the German car manufacturers [6], which has been further analysed in subsequent years by other research groups. Jaeger et al. [6] provided a deep analysis on the behaviour of the flow in a simplified HVAC duct, featured with a flap and correlated with experimental results obtained with Particle Image Velocimetry (PIV) measurements, illustrated in figure 1.6. They relied both on finite volume code and on Lattice-Boltzmann code to provide a comparison between the two. The researchers investigated the hydrodynamic behaviour (1.7) and extrapolated the values of sound pressure level up to 1000 Hz at different probes position 1.8.

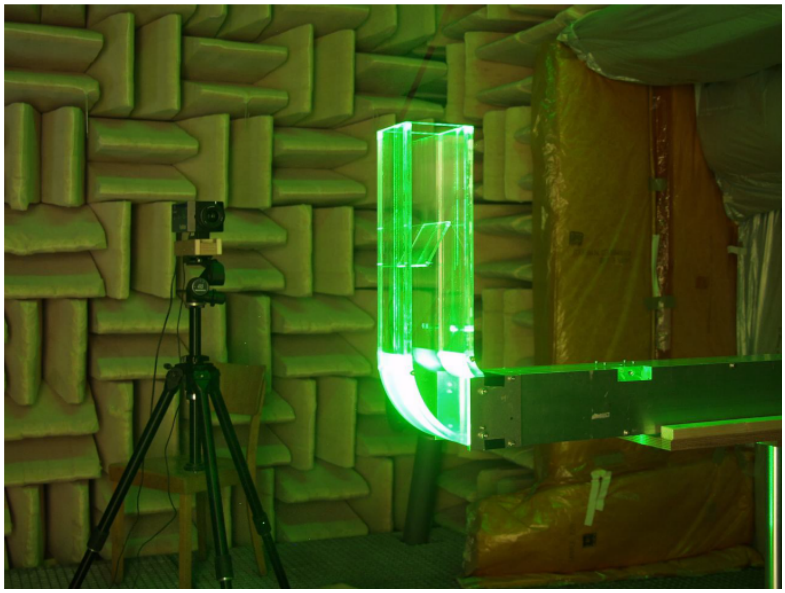

Figure 1.6: PIV experimental setup [6]

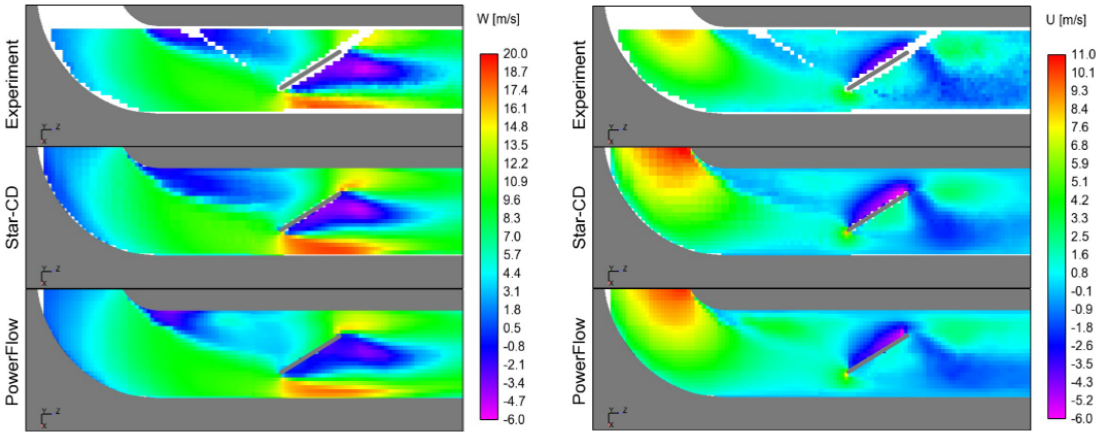

Figure 1.7: Time-averaged velocity components from [6]

However, these acoustic results are heavily influenced by the effect of the hydrodynamic terms on the pressure perturbation. In terms of correlation between experiments and simulation results obtained by Jaeger et al., the CFD curves underestimate the experiments, except for the Lattice-Boltzmann code for microphone 1, which highly overestimates the results, as observed in figure 1.8.

Further studies on the same experimental test case extended the analysis on the far-field region, implementing a hybrid approach in CAA simulation [7], [8].

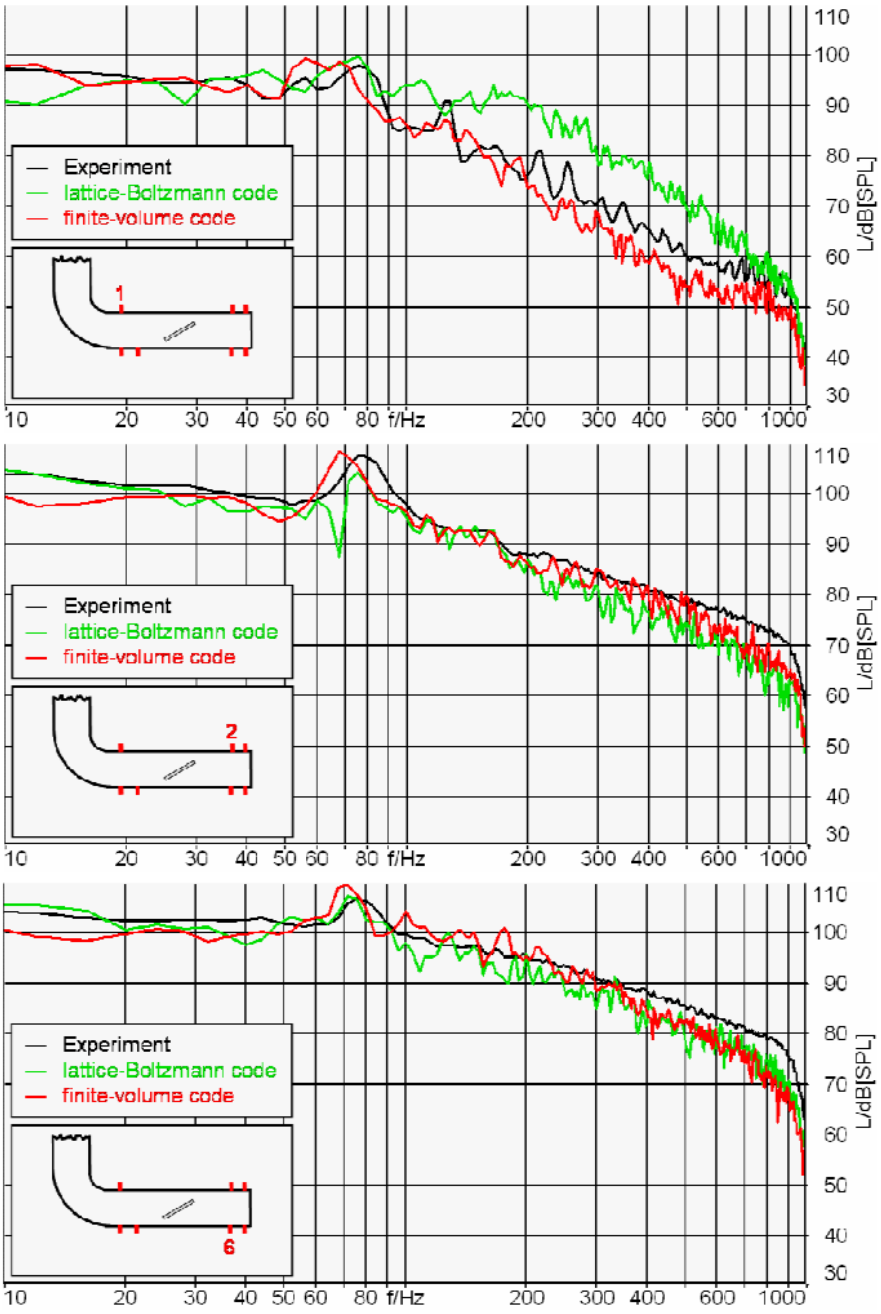

Figure 1.8: SPL results from [6]

Simulation activities carried out by Caro et al. [7] reached up to 2000 Hz in spectral resolution and, by exploiting the hybrid approach with the Lighthill's analogy, the decoupling of the acoustic perturbation from the hydrodynamic one was made

possible. The results were compared with experimental ones, which were obtained from a setup of 289 probes positions at a distance of 1 meter from the duct exit.

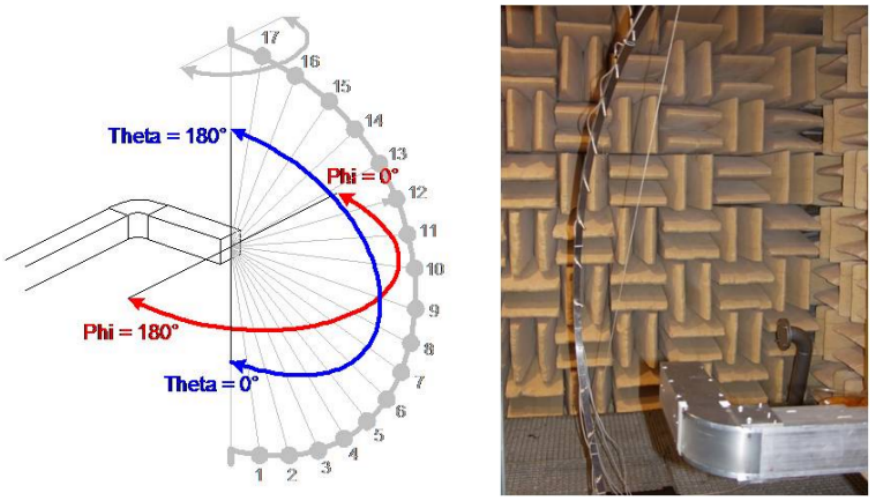

Figure 1.9: Experimental measurements in the far field from [7]

To perform aeroacoustics analysis, they relied on a model built on Actran Environment (where the CFD results were exported), which featured a detailed acoustic mesh to represent results up to 2000 Hz. The results obtained via Actran were closer to the experimental ones as it can be observed in figure 1.10, except for the description at frequencies below 100 Hz and after the peak at 1600 Hz, where major discrepancies are evident.

Kierkegaard et al. [8], followed an approach closer to the one adopted in this thesis project, since they started from a direct noise computation and then switched to the implementation of a hybrid method, with the aim to demonstrate that the results obtained with the latter were less affected by hydrodynamic pressure perturbation effects, thanks to the decoupling between hydrodynamic and aeroacoustics offered by the hybrid approach. For the DNC they adopted a Large Eddy Simulation (LES) and simulated two different time intervals of 0.04s and 0.3s, obtaining the results in figure 1.11. Overall, the results from DNC showed a closer agreement with the experiments over the entire frequency range. However, the spectral resolution was not high enough to have a precise comparison. For the hybrid approach, Kierkegaard et al. [8] relied on the Acoustic Perturbation Equation (APE) which was applied on the same mesh in the same simulation environment, without relying on any external software dedicated to the acoustics. The SPL results obtained are presented in figure 1.12.

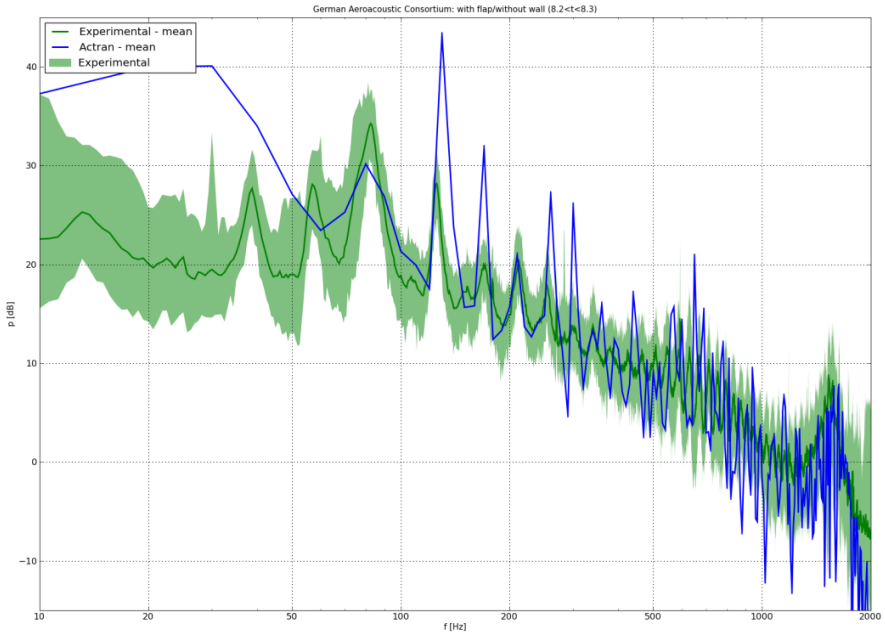

Figure 1.10: SPL results from [7]

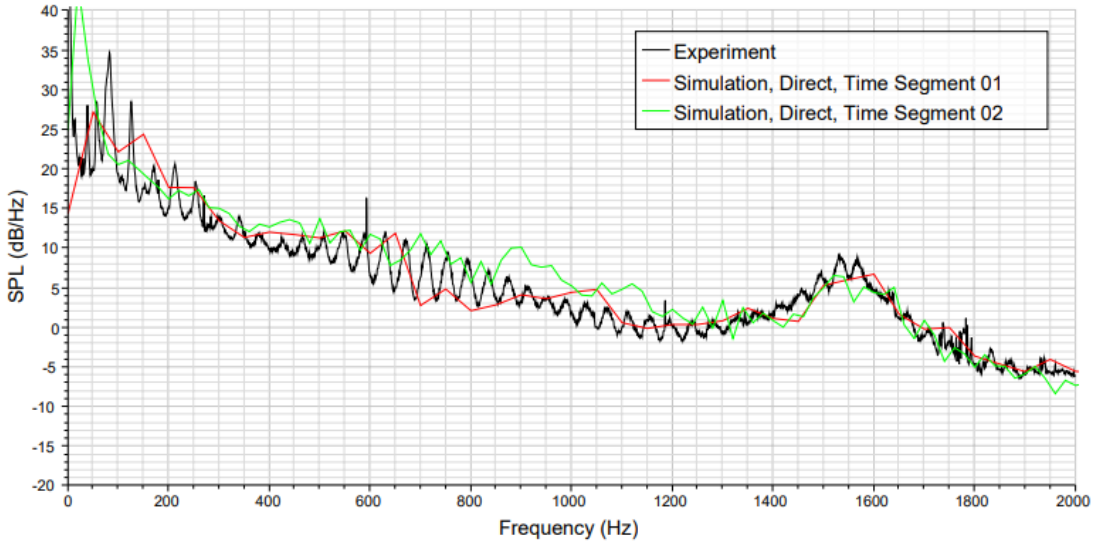

Figure 1.11: SPL results from DNC setup from [8]

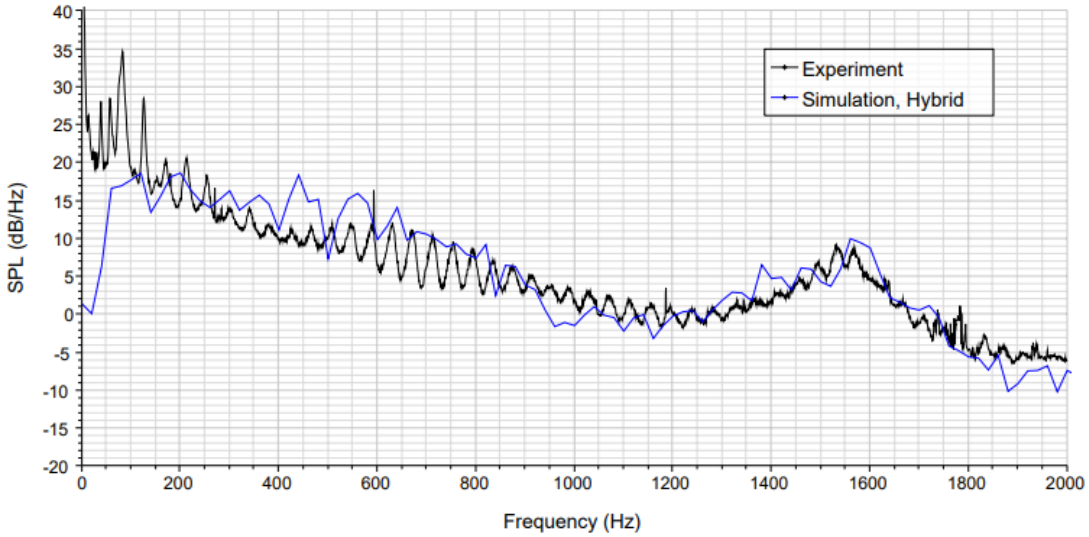

Figure 1.12: SPL results from APE setup from [8]

1.3 Thesis outlook

3D-CFD aeroacoustics simulation can rely on many different methodologies. In this thesis project, both a Direct Noise Calculation (DNC) approach and two hybrid approaches are investigated, to understand the differences both in terms of results produced and resource requirements for simulation. Following the steps of previous literature works, an initial investigation with DNC has been run to properly investigate the hydrodynamic behaviour of the airflow inside the duct and analyse the sound pressure level up to 1000 Hz. Once the results obtained have been properly uniformed with the literature reference, a switch towards hybrid methods has been done, where the highest desired frequency was set to 2000 Hz. The two hybrid methods investigated in the thesis project are the ones that involve the Lighthill Model and the Perturbed Convective Wave Model (PCW), which allow for an important speed-up while giving significative results to properly describe the acoustic behaviour in the far-field. The adoption of hybrid methods is gaining importance in the 3D-CFD analysis field because, by allowing a complete decoupling between the fluid dynamics analysis and the aeroacoustics analysis, it allows to process differently both the aspects at the same time, without any interference and with specific settings tuned accordingly to the different needs.

More in detail, chapter 2 follows all the steps involved in simulation setup for each methodology. All the strategies adopted since the early steady-state analysis will be presented in detail, alongside the crucial improvements adopted on-the-fly both in terms of mesh refinements and in model settings. Chapter 3 deals with

the results obtained from DNC, Lighthill Method, and PCW Method, with proper comparison with literature references and among the tested methodologies, with the aim to assess the fidelity with literature and to subsequently validate the developed methodologies. Finally, the main outcomes of the study are summarised in the conclusions.

Chapter 2

Methodology

2.1 Overview of the geometry

The thesis project revolves around a case study that has been deeply analysed in literature and it started in 2009 under the supervision of a consortium of German manufacturers [6]. Therefore, the geometry and the experimental data involved in this methodology development came from this study. The reference geometry is a simplified HVAC duct composed by a straight duct, 90 degrees bend and straight exit with a flap inside of it, as the geometrical measurements in figure 2.1 illustrate.

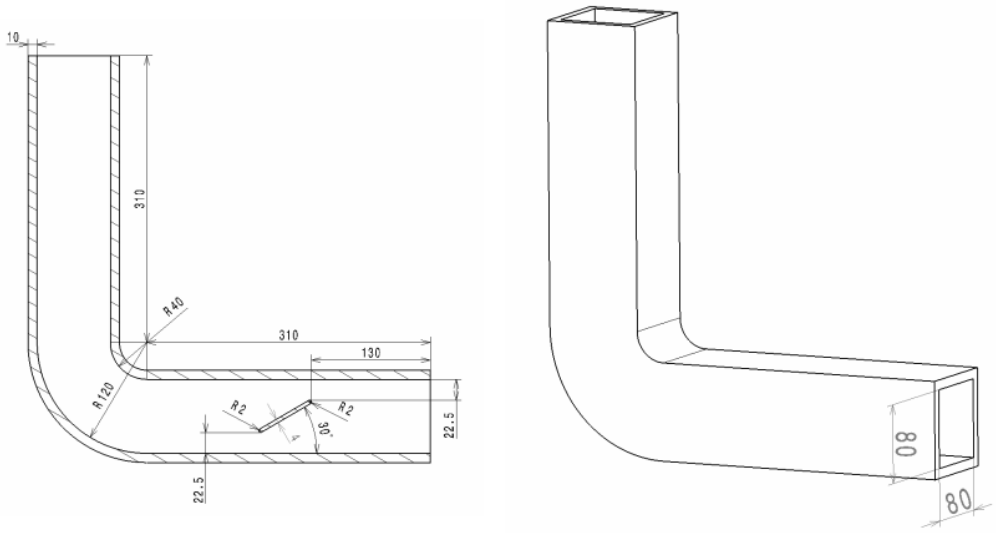

Figure 2.1: Geometry measurements from [6]

Two versions of the duct were analysed in the study, one in acrylic glass which

was also used to perform PIV analysis, and one in aluminium sheet panels for microphones measurements. The figure 2.2 shows the entire experimental setup.

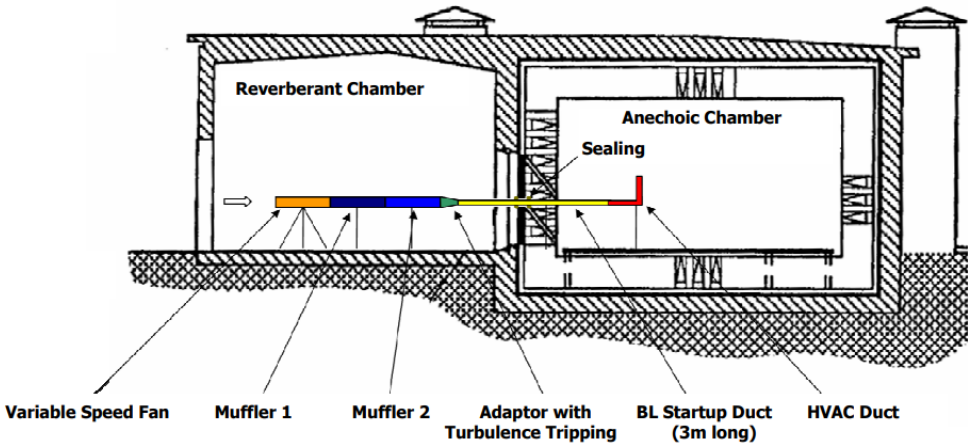

Figure 3. Experimental Setup

Figure 2.2: Experimental Setup from [6]

As shown in figure 2.2, the experimental piping has been divided into two different chambers: a reverberant chamber and an anechoic chamber. The first one contained the fan to maintain the air flow with an average inlet speed of 7.5 m/s, two mufflers to reduce the noise generated by the fan, an adaptor with turbulence tripping to allow a faster laminar-turbulent transition. The goal here was to isolate the components that generate higher noises from the proper test chamber, which is the anechoic one, that was separated by a sealing from the reverberant one. The flow connection was guaranteed by a long startup duct (3 meters) which has the main function to allow the flow to fully develop. The last element of the experimental setup was the simplified HVAC duct, the reference geometry taken as a test case. The presence of a long startup duct implied that the flow arrived at the simplified HVAC duct in a fully developed stage, with the velocity and the other parameters that are likely to differ from the fan suction side. Therefore, in simulation stages, a dedicated short simulation with a periodic boundary has been prepared to simulate the flow development and obtain realistic values for the actual inlet conditions at test case. Further details will be provided in section 2.4.

The study provided the geometric measurements for the duct (2.1), allowing a high-fidelity reproduction in the integrated 3D-CAD environment of Simcenter Star CCM+, as illustrated in figure 2.3. The pipe section is square, therefore a crucial geometrical parameter like the hydraulic diameter Dh can be determined, since it is necessary for the estimation of important fluid properties as will be

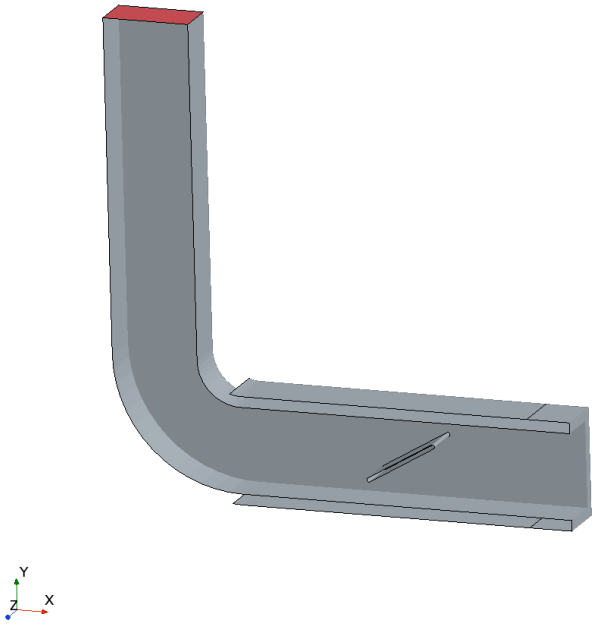

Figure 2.3: CAD Half-duct geometry designed in Star-CCM+

presented later. The square section implies a hydraulic diameter equal to the squared side, 80 mm. The geometry features a sharp edge that has been reproduced in CAD geometry and were subject of crucial analysis in mesh sensitivity. The duct geometry is characterised by symmetry along the y-axis. This aspect helps in reducing the domain size, taking only half of the duct into account, thus reducing the total amount of cells, which will reduce the computational resource required. For simulation purposes, as the image 2.4 shows, an outlet environment plenum shaped as a semi-sphere was added to the duct. However, due to symmetry only a quarter of sphere was considered.

From the image it can be noticed that only the duct's portion after the elbow was inserted in the plenum domain. This choice has been made to reduce the number of cells, because it was expected that the aeroacoustics effects behind the duct could be considered negligible, compared to the predominant acoustics phenomena that were expected on the exit side of the duct. On the counter side, particular attention is required when dealing with the flat surface of the plenum, which will be referred to as "Plenum base", ensuring that no reflection occurs and that waves are properly dissipated towards the boundary.

Figures 2.5 and 2.6 recall the experimental setup already discussed in chapter 1 section 1.2. The first shows the HVAC duct implemented for PIV analysis, which was used to investigate the flow behaviour inside the duct and its interaction with

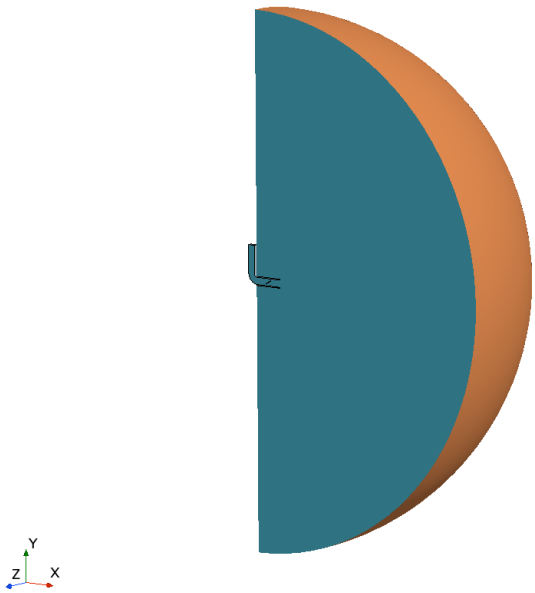

Figure 2.4: CAD Plenum Geometry designed in Star-CCM+

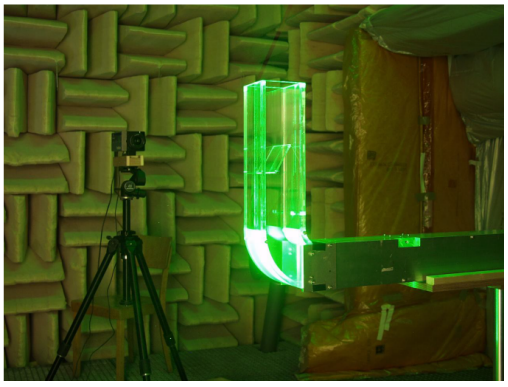

Figure 2.5: PIV experimental setup from [6]

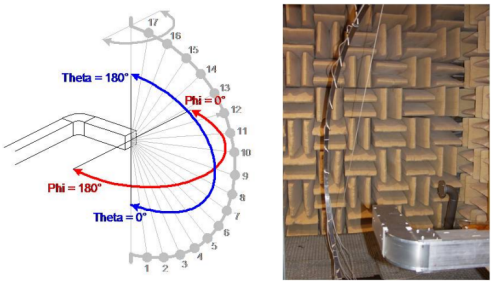

Figure 2.6: Microphones experimental setup from [7]

the elbow and the flap. The latter presents the tool adopted to evaluate the acoustic pressure waves in the far field. For that purpose, the test case has been provided by multiple probes, to also get the possible directionality of the sound pressure waves. The instrument adopted during the experiments was an arch with 17 probes position with an angular distance of 10 degrees each, to cover a 180° range. The arch was positioned at a radial distance of 1m from the centre of the duct's exit and was rotated over an angular span of 180°, to cover again 17 positions equally

spaced by an angular distance of 10 degrees. In the experiment, the simplified HVAC duct was positioned horizontally, therefore the angle that controls the arch position is referenced as phi, while the angle that controls the microphones' position within the arch is referenced as theta. The final experimental setup emulates a matrix of 17x17 microphones around the duct exit, on a virtual sphere of 1m radius, generating 289 probes locations. Such a matrix allows to cover enough positions to determine the acoustic waves propagating from the duct and to have a complete spatial description of them. Also, the experimental setup in figure 2.5 was provided by a dedicated microphones' setup, made by 7 probes inserted inside the duct, as can be observed in figure 2.7.

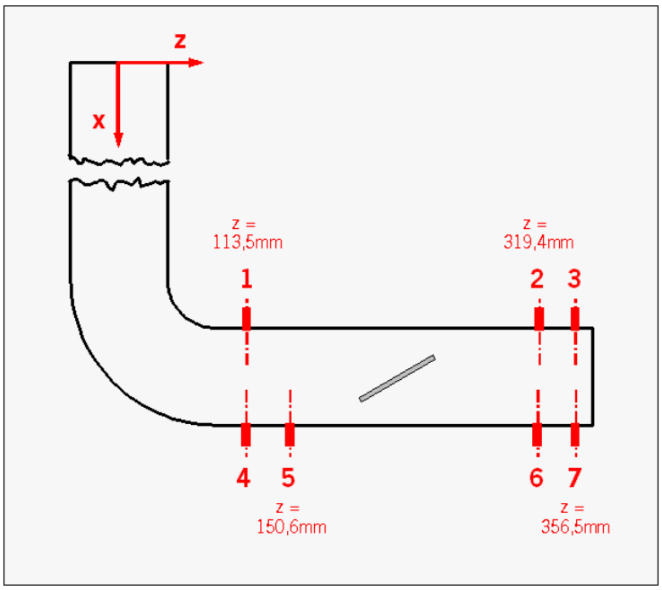

Figure 2.7: Experimental probes' position from [6]

Microphones' distribution is coherent with experimental tests setup, both for the DNC and the hybrid approach. About the DNC setup, the 7 probes are expected to capture mainly hydrodynamics effect, since they have been placed inside the duct, on the upper and lower surface, according to figure 2.7. The microphones have been replicated in Star-CCM+ environment as it is presented in figure 2.8. For the hybrid simulations setup, the layout in figure 2.6 is replicated with smaller modification related to the differences concerning the half-domain size and the duct orientation, since the duct in the simulation environment the duct is vertically oriented. A total of 17 theta-positions is present, while the number of phi-positions is 9, including the one on the exact symmetry plane. Overall, the total number of microphones is 153, covering a virtual quarter of sphere with 1 meter radius.

As it can be observed, picturing a virtual sphere that surrounds the duct exit,

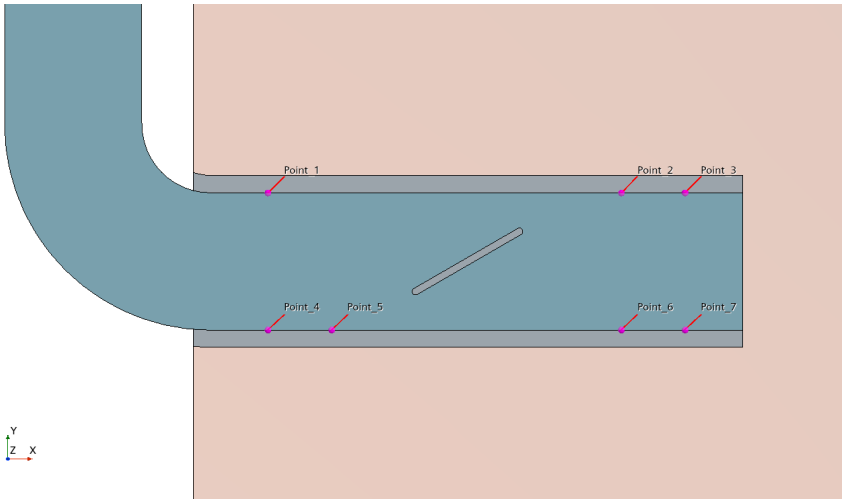

Figure 2.8: Probes position in Star-CCM+

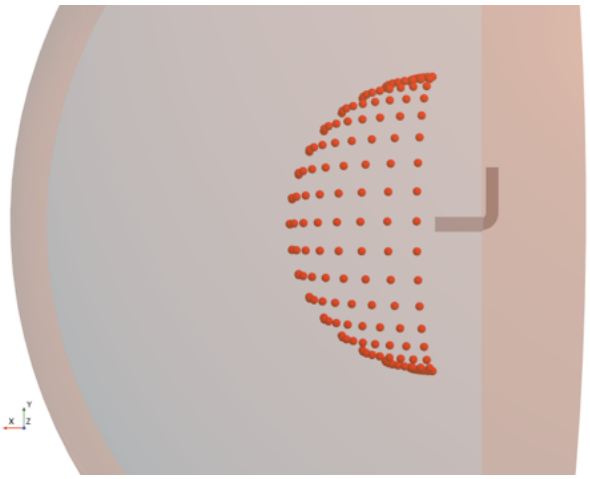

Figure 2.9: Side view of microphones positions

the microphones are closer at poles and distant at the equator. This means that each microphone covers a different portion of area on the virtual spheric surface. This consideration will be crucial in post-processing analysis, and it will be proper disserted in chapter 3.

2.2 Aeroacoustics methodology background

The simulations methodologies adopted in the thesis project are briefly described in this section. First, the Direct Noise Computation (DNC) is presented. Then, the two

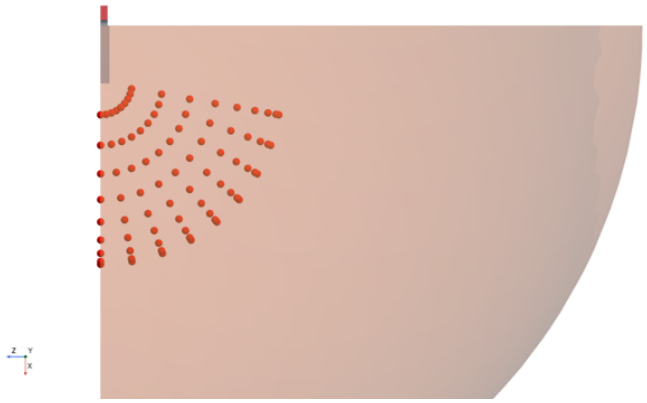

Figure 2.10: Top view of microphones positions

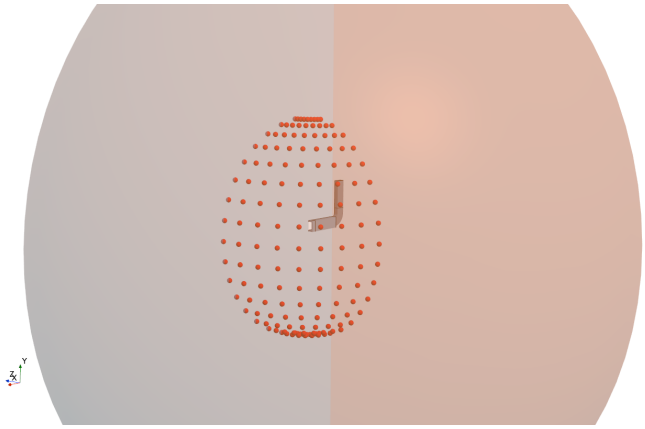

Figure 2.11: Perspective view of microphones positions

hybrid methods based on the Lighthill Model and the Perturbed Convective Wave (PCW) model are illustrated alongside their main features related to aeroacoustics analysis.

2.2.1 DNC methodology background

The DNC approach is very reliable for the aeroacoustics analysis in the near-field but it is conditioned by some drawbacks for the far-field analysis. DNC requires to solve the entire flow field to calculate the acoustics generated by aerodynamics, thus it is very expensive from a computational point of view. Nevertheless, it gives high accuracy and fidelity if high numerical resolution is properly guaranteed to capture the acoustic pressure perturbations and its transient effects. As specified by Bailly et al. [9] the application of DNC is suggested for compressible flows

applications and to investigate the pure physics of the transient phenomena. In this thesis project, DNC has been applied on a low Mach number flow, even though more efficient methodologies are available for this specific case study, as the hybrid methods that were adopted afterwards. For this reason, it has been applied only in the very near-field and with a target frequency up to 1000 Hz, according to what has been done in reference literature by Jaeger et al. [6]. The main parameter related to aeroacoustics that will be monitored at probes is:

$$p' = p - p_{mean} \tag{2.1}$$

where

- p is the static pressure value.
- p_{mean} is the field mean pressure, which is the time-averaged value of the pressure fluctuation at probes. It is evaluated through monitors pointing at virtual probes in STAR-CCM+ environment.
- p' is the difference term that expresses the acoustic perturbation.

By monitoring this parameter it is possible to evaluate the aeroacoustics phenomena in the domain, as follows in the next chapters.

2.2.2 Hybrid methods methodology background

The adoption of Hybrid Methods based on Lighthill's Analogy and Perturbed Convective Wave Model reshape completely the approach to aeroacoustics simulation thanks to the complete decoupling between aerodynamics and aeroacoustics and the numerous advantages offered when performing unsteady simulations for incompressible flows at low Mach numbers ($Ma < 0.2$) [**10**].

The Lighthill Wave model solves the equation related to the transport of the Lighthill pressure p^l which comes as the sum of the hydrodynamic pressure term p^h and the acoustic pressure term p^a:

$$p^l = p^h + p^a \tag{2.2}$$

The key concept of the Lighthill's analogy is that in the far-field, the Lighthill pressure p^l can be approximated with the acoustic pressure term pa, meaning that the hydrodynamic term can be considered negligible. The transport equation for the Lighthill pressure p^l is shaped as follow according to Siemens Star-CCM + User Guide [10]:

$$\frac{1}{{c_0}^2}\frac{\partial^2 p^l}{\partial t^2} - \nabla^2 \cdot \left(p^l + \tau \frac{\partial p^l}{\partial t}\right) = \nabla \cdot h \tag{2.3}$$

where h represents the divergence of the fluctuating component of the Lighthill Stress tensor:

$$h = \nabla \cdot [b_s \rho(\mathbf{v} \times \mathbf{v} - \overline{\mathbf{v} \times \mathbf{v}})] \tag{2.4}$$

where:

- p^l is the Lighthill pressure
- c_0 is the speed of sound in the far-field
- t is the time
- v is the velocity
- b_s is the Noise Source Weighting Coefficient
- ρ is the gas density

and τ is he noise source damping term which is defined as follows:

$$\tau = b_d \frac{\Delta x}{\pi c_0} \tag{2.5}$$

The Perturbed Convective Wave Model takes a different approach and solves a wave equation for an acoustic potential from which every quantity related to aeroacoustics is derived. The model equation has been developed starting from the Linearized Perturbed Compressible Equation [11], which leads to the following wave equation for the acoustic potential ϕ:

$$\frac{D^2\phi^a}{Dt^2} - {c_0}^2 \Delta \left(\phi^a + \tau \frac{\partial \phi^a}{\partial t} \right) - \frac{1}{\rho} \nabla \phi^a \cdot \nabla {p_{inc}}^f = -\frac{1}{\rho} \frac{D{p_{inc}}^f}{Dt} + S_{\phi^a} \tag{2.6}$$

where:

- c_0 is the speed of sound
- t is the time
- ρ is the gas density
- ${p_{inc}}^f$ is the incompressible pressure fluctuation
- S_{ϕ^a} is the external noise source that could be taken into account in the model
- τ is the noise source damping term

where the noise source damping term is defined as:

$$\tau = b_d \frac{\Delta x}{\pi c_0} \tag{2.7}$$

where:

- b_d is the acoustic damping coefficient
- δx is the cubic root of the cell volume

From the acoustic potential ϕ^a it is possible to derive the acoustic pressure p^a, the acoustic density ρ^a and the acoustic velocity v^a as follows:

$$p^a = \rho \frac{D\phi^a}{Dt} \tag{2.8}$$

$$\rho^a = \frac{p^a}{{c_0}^2} + \rho \tag{2.9}$$

$$v^a = -\nabla \phi^a \tag{2.10}$$

Taking into account that:

$$p_p = p^a + {p_{inc}}^f \tag{2.11}$$

where p_p is the overall pressure perturbation term, it is possible to obtain the complete decoupling between aeroacoustics and fluid dynamics. In fact, by deriving the acoustic pressure from the acoustic potential and considering as known the pressure perturbation from simulation results, it is possible to determine the incompressible pressure fluctuation at every time instant.

2.3 Project workflow

The workflow adopted in this study is shown in figure 2.1, which is generally valid both for simulations involving DNC as well as for simulations performed with hybrid models. The only difference is related to the target parameter in the loop, since the DNC approach requires a mesh tuning based on the so-called "mesh frequency cut-off", while hybrid approaches are based on a mesh tuning related to the "Taylor microscale". This difference will be properly described in the sections dedicated to the specific approaches (2.4 and 2.6).

As emerges from the workflow, the crucial aspect when setting up a 3D-CFD simulation is the proper calibration of the mesh size for every component of the domain. Implementing a proper mesh is mandatory to study all the phenomena involved, otherwise the simulation cannot lead to results representative of the real

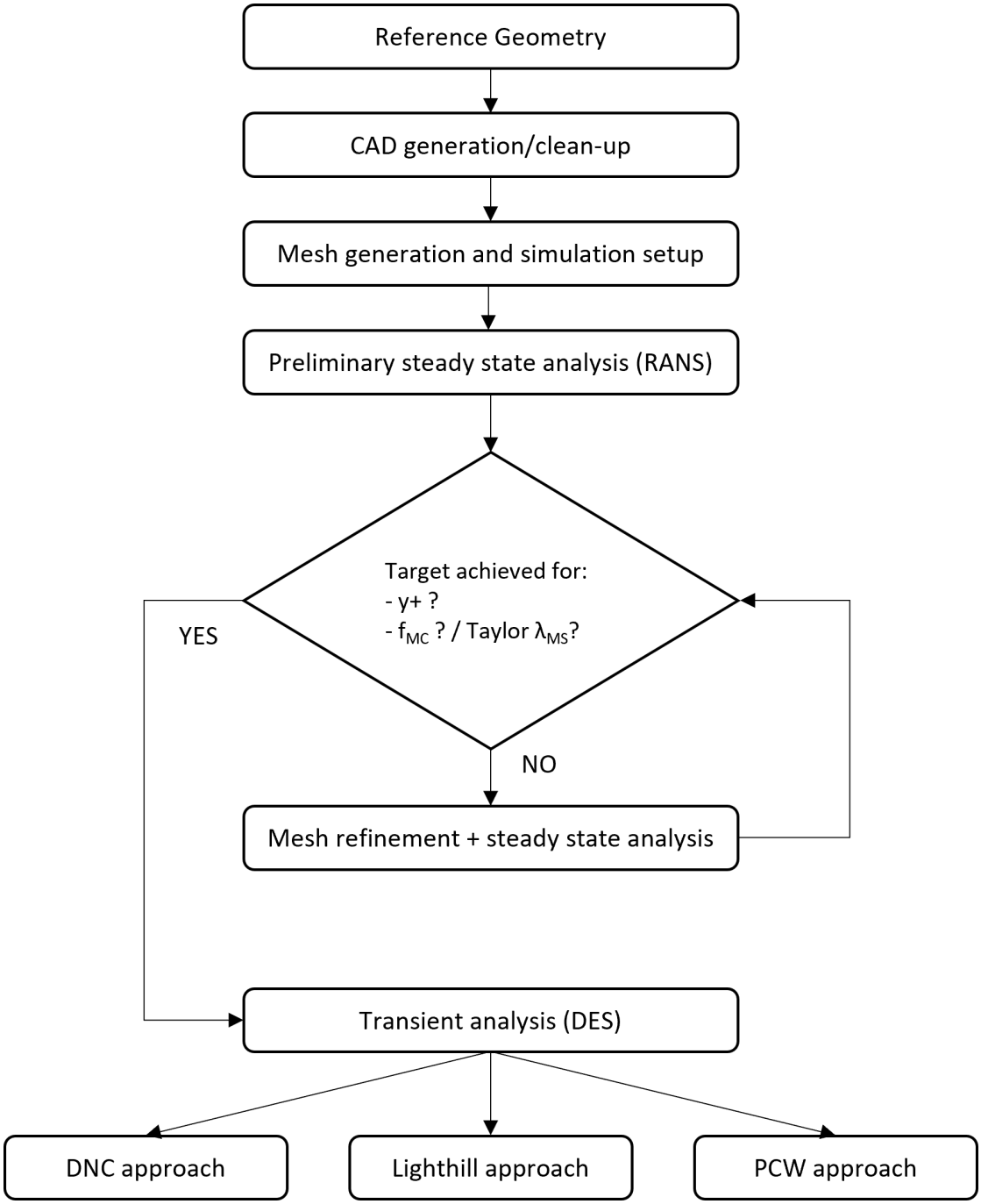

Figure 2.12: Project workflow

phenomena. Moreover, a proper mesh optimization helps in reducing the estimated computational time and adapt the simulation processes to an industrial context

where it is possible to exploit advanced HPC systems but the time dedicated to the product development is generally reduced. Therefore, during the methodology development process, a deep focus has been given to the stages that involve the mesh preparation.

The workflow depicts the ideal process to follow when implementing the methodology standard developed during the thesis project. Once the geometry has been introduced and prepared for meshing stages, the mesh calibration loop is iterated until the required target is achieved. Once the results obtained from the steady-state simulation are considered as reliable, the focus is shifted to the transient analysis. However, the methodology development itself faced further mesh modification after several Detached Eddy Simulations (DES), both for DNC and hybrid methods. This was because some issues related to the mesh developed in steady-state could be discovered only with the results provided by the unsteady simulations. This aspect illustrates the importance of the methodology development, because it allows to understand properly every small detail related to the chosen approach and gives the opportunity to whoever applies the methodology to save time during simulation stages.

2.4 Steady-state analysis for DNC

The first step in the simulation workflow, provided that a CAD of the geometry is available, is to prepare the mesh and the simulation setup for the steady-state Raynolds Averaged Navier-Stokes (RANS) analysis. During this phase, and the CAD surfaces were assigned to regions to set all the boundaries and define their properties. The steady-state analysis is necessary because it offers the possibility to refine at best the mesh prior to run the unsteady simulation, with the goal to provide the latter with a mesh that is calibrated to get all the targeted results, and minimise the necessity to run multiple unsteady simulations.

The target of the analysis was to produce uniformed results with the reference literature from Jaeger et al. [6] test case. Therefore, the first stages of the project targeted the achievement of obtaining reliable results with DNC approach up to a resolution of 1 kHz. It is important to remark that this approach gives more details about the hydrodynamics phenomena happening in the simplified HVAC duct, because the probes are inserted inside the duct, rather than in the far-field. A test with DNC has been considered necessary first to check the accuracy in the flow description inside the duct, and then to understand the resource requirements that come with this approach and so to understand how it can be adopted in daily work. It is known that performing a direct noise calculation requires significant resources, therefore every strategy when performing the prior steady-state analysis is properly calibrated to optimize the setup for the unsteady simulation. The key

guiding principles when setting up a mesh for DNC are the following ones:

- Guarantee a detailed mesh description where turbulences develop.
- Ensure a proper description at boundary layers.
- Guarantee an accurate description at the outlet jet-flow region to properly simulate the jet development.
- Setting up a slow volume mesh cells growth to avoid spurious waves with numerical origin.
- Provide wave dissipation at outlet boundaries, which is necessary to avoid reflections that could pollute acoustic results

Several tuning steps have been taken to find the optimum compromise for steady-state simulation and the adopted setup is properly described in the section 2.4.1.

2.4.1 Mesh preparation

To obtain the desired mesh for DNC calculation a procedure by steps has been followed, starting with a first tentative mesh and implementing further refinements with the aim to ensure the mesh frequency cut-off value at 1 kHz. First, the polyhedral cell type has been chosen, since it guarantees less distortions, a higher cell quality, a better gradients approximation, and a higher convergence behaviour. Some drawbacks are linked to the polyhedral cells since they cannot be aligned with the flow direction and they can introduce higher dissipation when compared to trimmed cells. However, the priority was to avoid a 1:2 cell size transition, which is a feature of the trimmed mesh.

As it can be observed in the figures 2.13 and 2.14, different mesh sizes has been adopted in the domain and each one of them is properly calibrated for a specific function:

- Inside the duct, a sufficiently small mesh size of 4 mm was adopted in the bulk region (the straight portion of the duct upstream the bend), to describe the flow entering the domain.
- A finer mesh was used to proper describe the flow behaviour in detachment and recirculation areas, with a cell size of 0.8 mm.
- Outside the pipe, a fine mesh of 1 mm was adopted in a cone-shaped volume to describe the jet development, which is a length of 10 times the hydraulic diameter (around 0.8 m).

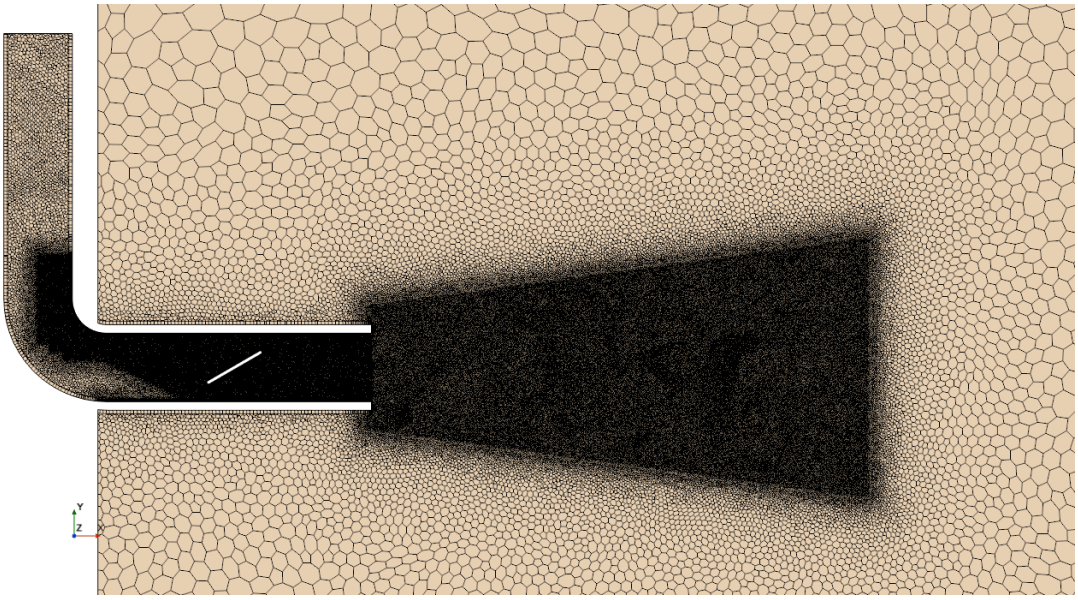

Figure 2.13: Duct and jet development area mesh refinement

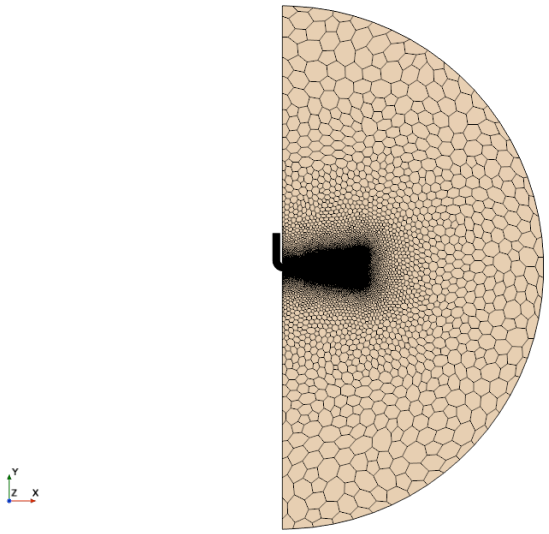

Figure 2.14: Plenum mesh

- The remaining portion of the domain required a bigger cell size that gradually increase, to allow the dissipation of pressure waves and to reduce the computational time required.

The figure 2.15 shows that a very smooth mesh size transition wass guaranteed

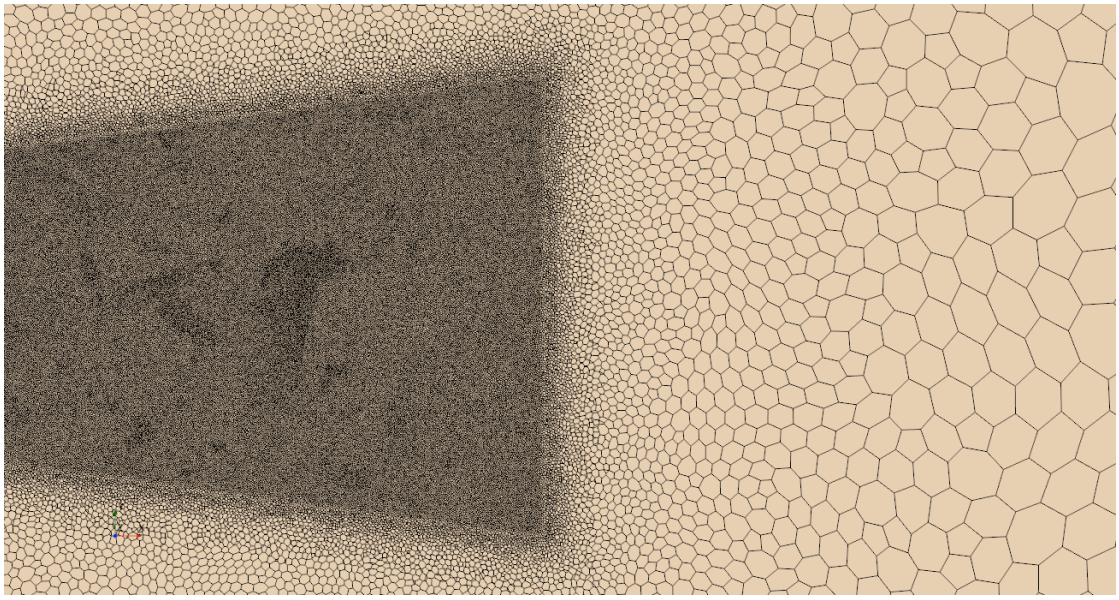

Figure 2.15: Mesh transition at the end of refinement area

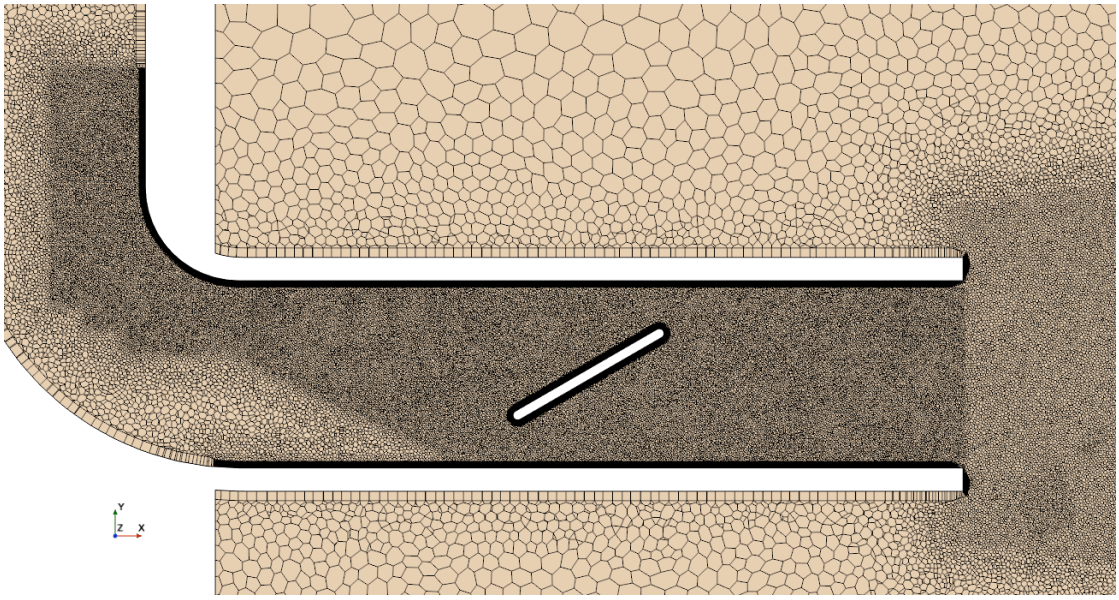

Figure 2.16: Duct mesh

when moving from the jet development zone towards the plenum outlet. To this purpose, it was mandatory to maintain low values of surface growth rate (not higher than 1.1) and volume growth rate (not higher than 1.05). For what concerns the refinement inside the duct, it is important to control the number of refined cells

as much as possible, because a small extension of the refinement can increase a lot the number of cells and so the required resources during simulation. The figure 2.16 shows clearly that the refinement inside the duct started just before the region where the flow was observed to detach from the elbow. The image 2.17 shows an image of the flow velocity inside the duct, where the detachment point right after the elbow is clearly visible.

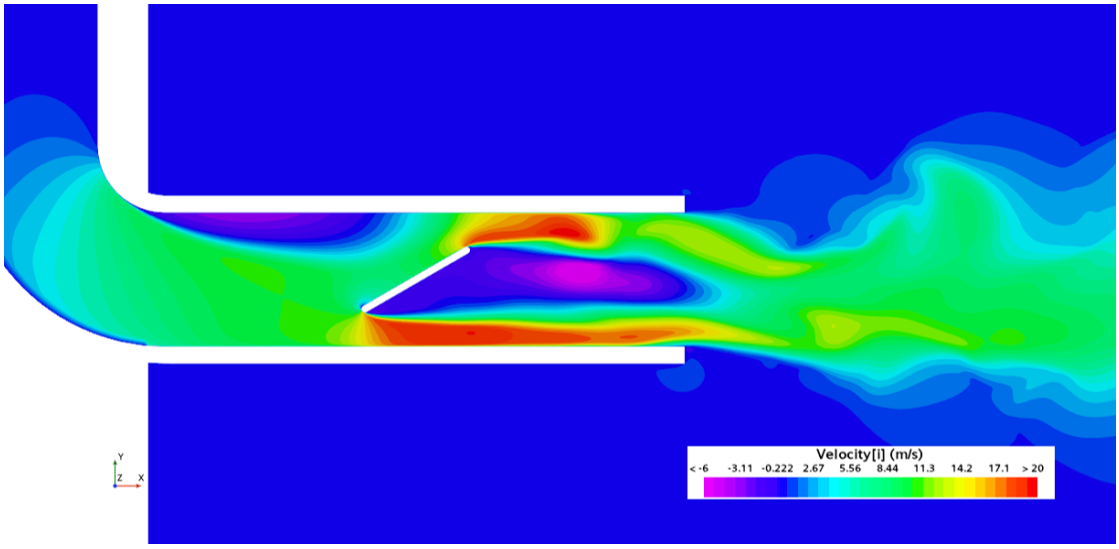

Figure 2.17: Velocity results from steady-state analysis prior to DNC

For this reason, the lower part of the elbow was excluded from the refinement since it is less important for the turbulence generation. Then, from the flap to the end of the duct the refinement was mandatory to get a proper flow development description. The tables below resume the main mesh parameters about the surface mesh and the volume mesh and for what concerns the boundary layers, specific considerations follow in the dissertation.

For what concerns the custom controls, a high percentage compared to base was indicated for the plenum surfaces, since it was necessary to force a mesh growth towards the boundaries. However, the low values of surface growth rate and volume growth rate allow to have a smooth transition, and, at the same time, sufficiently large cells close at outlet boundaries. A slight difference in mesh size between duct refinement area and jet development area helps in reducing the total number of cells and so the computational time required, while ensuring a good mesh frequency cut-off, as the image 2.18 shows.

A crucial aspect during mesh preparation is the prism layer setting. The mesh should be prepared for the subsequent DNC simulations which relies on Detached Eddy Simulation (DES), meaning that a pure RANS approach is adopted at walls,

Base mesh options	
Cell type	Polyhedral Cells
Base Size	4E-3 m
Target Surface Size	100%
Minimum Surface Size	10%
Surface Growth Rate	1.1
Volume Growth Rate	1.05
Minimum Face Quality	0.2
Surface Curvature	36 Pts/circle
Surface Proximity	1.0 m search floor, 2 points in gap
Maximum Tet Size	10000% of base
Core Mesh Optimization	4 cycle, 0.8 quality treshold

Table 2.1: Base mesh options for steady-state for DNC approach

Custom controls	
Duct refinement, volumetric control	8E-4 m
Jet development area, volumetric control	1E-3 m
Symmetry plane on duct, surface control	100%
Plenum base and sphere, surface control	5000%
Symmetry plane on plenum, surface control	5000%

Table 2.2: Mesh custom controls for steady-state for DNC approach

and a pure Large Eddy Simulation (LES) at core. It means that the description of the flow behaviour in the boundary layer is crucial for the entire simulation. However, it is necessary to guarantee a proper trade-off between accuracy and computational requirements, therefore two different strategies have been adopted: a high y+ approach on the bulk region and a low y+ approach on the refinement area inside the duct. The near wall layer thickness for the low y+ approach has been properly tuned accordingly to the following procedure:

First, the Reynolds Number Re is evaluated

$$Re = \frac{D \cdot U}{\nu} \tag{2.12}$$

where:

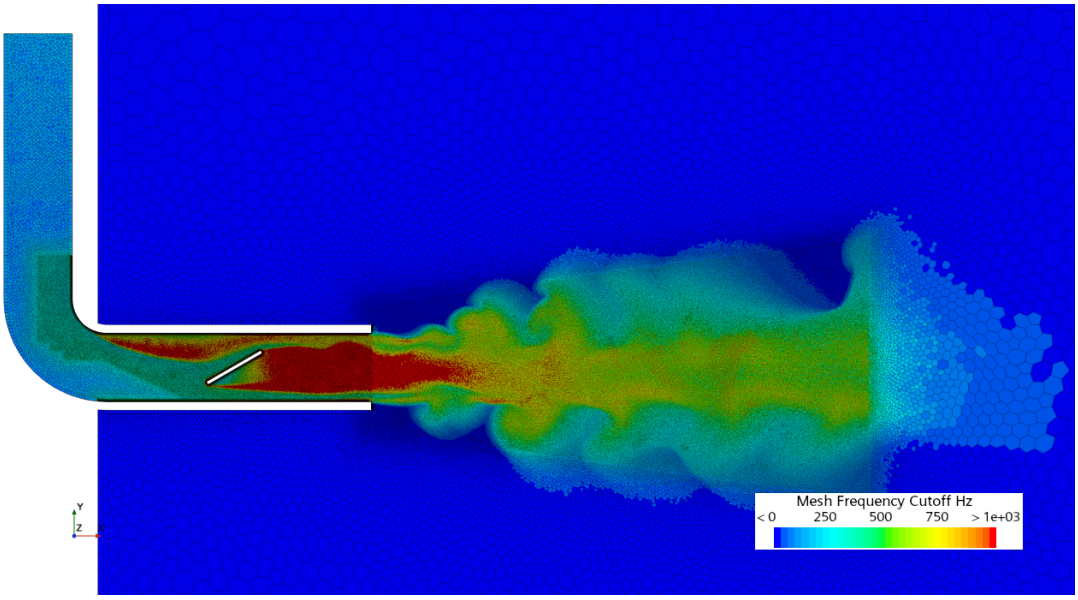

Figure 2.18: Mesh Frequency Cutoff

- ν is the kinematic viscosity of the flow
- D is the hydraulic diameter of the duct
- U is the average velocity at inlet

Then, the skin friction coefficient C_f is evaluated

$$C_f = [2\log_{10}(Re) - 0.65]^{-2.3} \tag{2.13}$$

$$Re < 10^9 \tag{2.14}$$

which allows to evaluate the wall shear stress τ_w, useful to estimate the friction velocity

$$\tau_w = \frac{1}{2} \cdot \rho U \cdot C_f \tag{2.15}$$

$$\upsilon_\tau = \sqrt{\frac{\tau_w}{\rho}} \tag{2.16}$$

where ρ is the fluid density Finally, the near wall prism layer thickness y_1 is evaluated after establishing a desired value of $y+$

$$y_1 = 2\frac{y^+ \cdot \nu}{\upsilon_\tau} \tag{2.17}$$

Inlet Velocity	7.5 m/s
Hydraulic Diameter	0.08 m
Kinematic Viscosity at 25°C	1.5520E-05 m^2/s
Air Density at 25°C	1.1839 kg/m^3
Desired minimum y^+	0.45

Table 2.3: Parameters for near wall layer thickness calculation for DNC approach

The values adopted are reporting in the following table:

The high y+ approach requires a y+ value at walls between 20 and 300, while a low y+ approach imposes a value between 0 and 5. In tuning stages the desired value for the y+ has been subjected to an iterative process and, as it can be observed in the table 2.3, it is very close to zero. For this steady-state analysis, following the needs related to computational constraints, a y+ value between 1.5 and 3 was maintained where the low y+ approach was targeted. To have high fidelity, an elevated number of layers with a slow Growth Ratio was required and for this test case a total of 15 layers with 1.1 Growth Ratio have been selected. Another zone of interest is the behaviour of the boundary layer at edges, where it is important to ensure a proper description of the flow. For test cases like this, a sharp edge represents a critical zone where the prism layers could collapse, worsening the results of the simulation. This issue can be controlled by a proper tuning of some parameters such as the Prism Layer Reduction Percentage, the Gap Fill Percentage, the Boundary March Angle, and the Minimum Thickness Percentage. The following table resumes the prism layer setup for the low y+ approach:

Prism layers parameters for low y+ approach	
Number of Layers	15
Near Wall Thickness	8.48E-5 m
Total Thickness	2.69E-3 m
Growth Ratio	1.1
Prism Layer Reduction Percentage	1
Gap Fill Percentage	45
Minimum Thickness Percentage	1
Boundary march angle	50 deg

Table 2.4: Prism layers parameters for low y+ approach for DNC

The figures 2.19 and 2.20 show some details of the boundary layer for the refinement area, as the lower tip of the flap and a portion of the bottom wall of the duct in figure 2.19 and the sharp edge at the top corner of the duct in figure 2.20. In the first one it can be observed how the growth ratio between layers was respected and how the mesh transition between the boundary layers cells and the core cells appeared smooth and regular. It is important to guarantee that no abrupt mesh changes are generated in this area, since a fast and irregular transition can corrupt the final results. in the latter, the mesh behaviour at the sharp edge has been controlled to guarantee at least 2 boundary layers at the corner. The low y+ approach is extended over the vertical edge of the duct, to extended the surface subjected to detailed description and to guarantee a smooth transition between low and high y+ approaches.

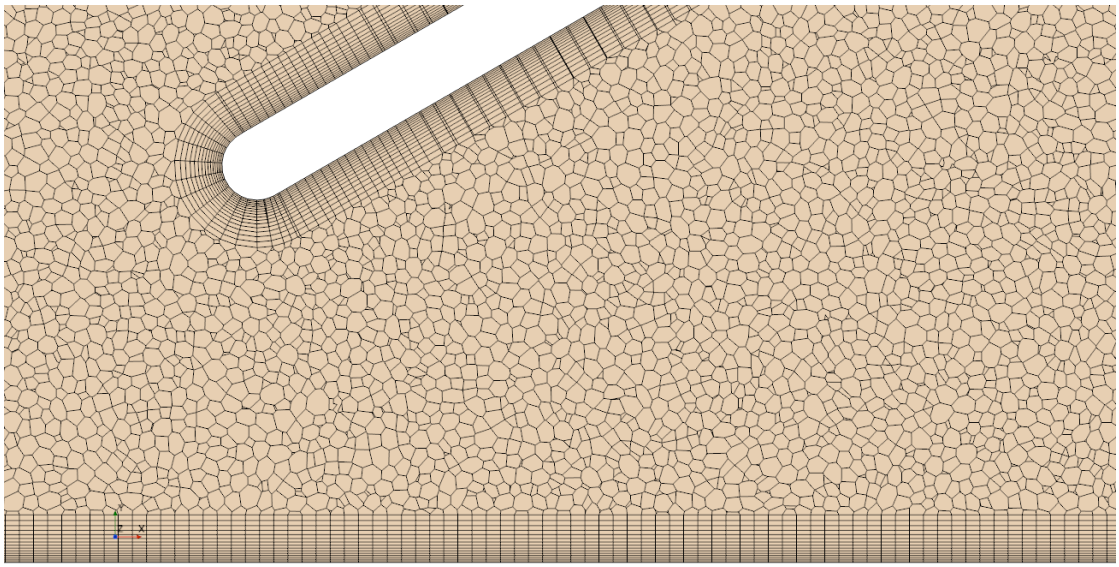

Figure 2.19: Zoom on the lower tip of the flap

For what concerns the high y+ approach, no specific requirements are present for the portion of the duct between the inlet and the elbow, where a single layer is sufficient to describe the flow behaviour at walls. The following table resumes the main parameters that differ from the low y+ ones.

The image 2.21 shows the y+ values for both the approaches. It can be observed that the desired values have been obtained, particularly for the refinement zone.

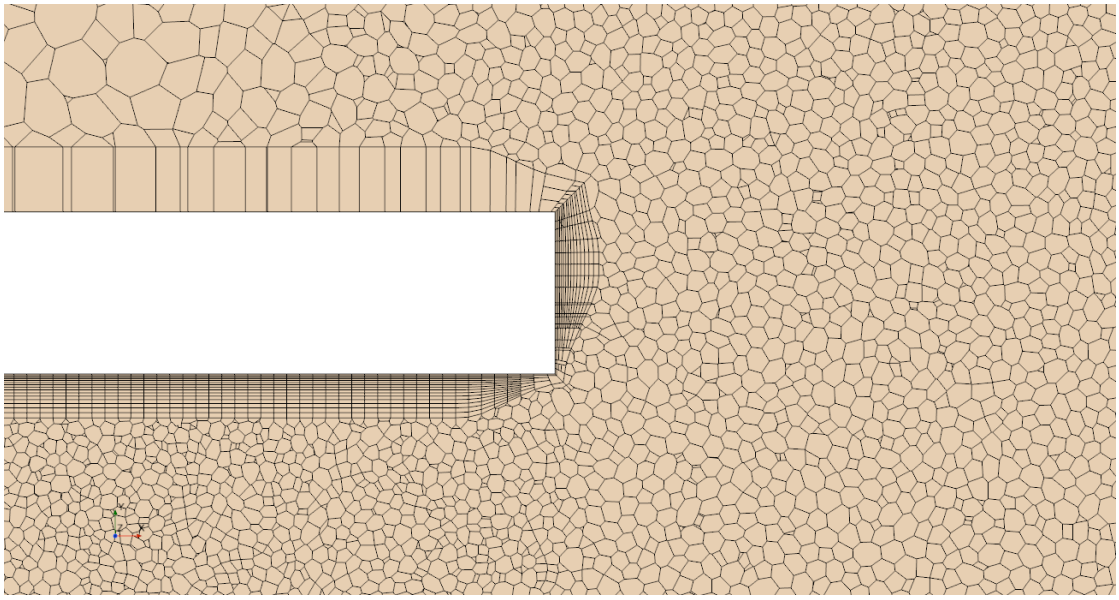

Figure 2.20: Zoom on the top edge corner of the duct

Prism layers parameters for high y+ approach	
Number of Layers	1
Near Wall Thickness	4E-3 m

Table 2.5: Prism layers parameters for high y+ approach for DNC

All these considerations bring the total number of cells to 17.5M, which will have a considerable impact on the resource requirements, confirming that the main drawback for DNC is the number of cells and the refinement necessities in the jet development area.

2.4.2 Physics Models

The physics models introduced in the steady-state setup are the ones in the picture 2.22. The setup relied on the RANS approach and the chosen turbulence model was SST (Menter) K-Omega. To prepare for the aeroacoustics analysis, the following models have been introduced to gather all the information related to the aeroacoustics behaviour of the test case: Aeroacoustics, Curle, Noise Source Models,

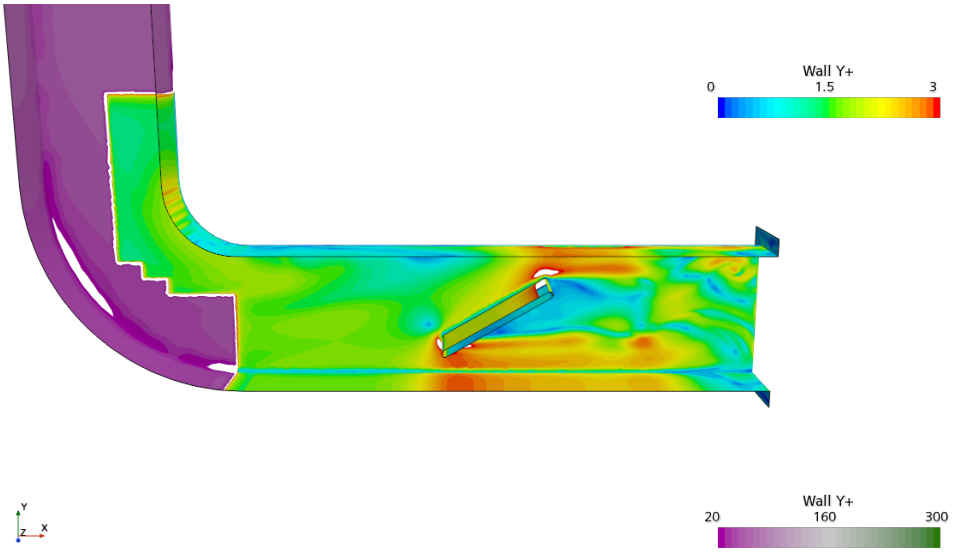

Figure 2.21: Zoom on the top edge corner of the duct

Proudman. The goal of the steady-state simulation is to provide a reliable mesh for the following unsteady simulation and it is useful to get a general idea about the acoustic behaviour in the steady-state reference. The chosen specifications for the physics models are presented in table 2.6.

Physics conditions		
Gas >Air	Dynamic Viscosity	Sutherland's law
	Specific Heat	Polynomial in T
	Thermal Conductivity	Sutherland's law
Gradients	Limiter Method	Venkatakrishnan
	TVB Gradient Limiting	No
	Acceptable Field Variation	0.005
Segregated Flow	Convection	2^{nd} order
Segregated Fluid Temperature	Convection	2^{nd} order
SST K-omega	Convection	2^{nd} order

Table 2.6: Physics models settings for steady-state analysis

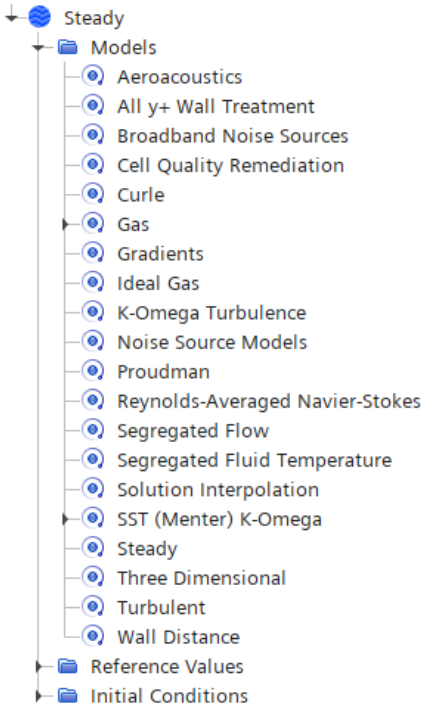

Figure 2.22: Steady-state RANS physics models

The main indication that comes from these properties is that a 2nd order convection is generally preferred to enhance the reliability of the simulation. As Gradients, the chosen limiter method was Venkatakrishnan and no specifications were made about the Total Variation Bounded (TVB) gradient limiting. The following table illustrates the initial conditions chosen for the specific test case.

Initial conditions	
Static Temperature	298.15 K
Pressure	0.0 Pa
Turbulence Specification	Intensity + Length Scale
Turbulence Intensity	0.1
Turbulent Length Scale	0.0056 m
Turbulent Velocity Scale	0.75 m/s
Velocity	[0.0, -7.5, 0.0] m/s

Table 2.7: Physics initial conditions for steady-state analysis for DNC

The pressure value reported in table 2.7 is the relative gauge pressure, therefore it indicates the delta compared to the ambient pressure, therefore it is set to 0 Pa. The turbulence specification is chosen as Intensity + length scale according to literature [12], [13] and because it is possible to evaluate these parameters from geometrical considerations, since no specific information is provided by the experimental data. The turbulence intensity I can be initially estimated to 10%, while the turbulent length scale l_m can be considered the 7% of the hydraulic diameter Dh for developed flows:

$$l_m = 0.07Dh \tag{2.18}$$

where Dh is 0.08 m, hence the internal side of the pipe square section.

2.4.3 Solvers

The solver settings are reported in table 2.8, while a proper tuning will be adopted in the DNC approach. The Segregated Flow implicit scheme was SIMPLE and the under-relaxation factor for K-Omega solver was set to 0.8.

Segregated Flow	Implicit Scheme	SIMPLE
	Velocity Under-Relaxation Factor	0.7
	Pressure Under-Relaxation Factor	0.3
Segregated Energy	Fluid Under-Relaxation Factor	0.9
K-Omega Turbulence	Under-Relaxation Factor	0.8

Table 2.8: Solver settings for steady-state analysis for DNC

2.4.4 Boundaries

Once the physics models and solvers were set, CAD surfaces were assigned to regions and the boundaries were defined. First, a symmetry plane was defined where the geometry has been halved. Then, it was necessary to define the properties at walls, which are all the surfaces of the Simplified HVAC duct. The duct's surfaces were set as adiabatic no-slip smooth walls, to emulate as close as possible aluminium sheet panels. The inlet and outlet boundaries have been subjected to various tests and configurations to obtain a reliable description of the flow behaviour.

The final boundary conditions setup is illustrated in figure 2.23 and it was featured with a freestream inlet boundary, which has been initialised with results obtained by a prior steady-state simulation where the inlet boundary was set to velocity inlet, as reported in the workflow in figure 2.24. This has been done to

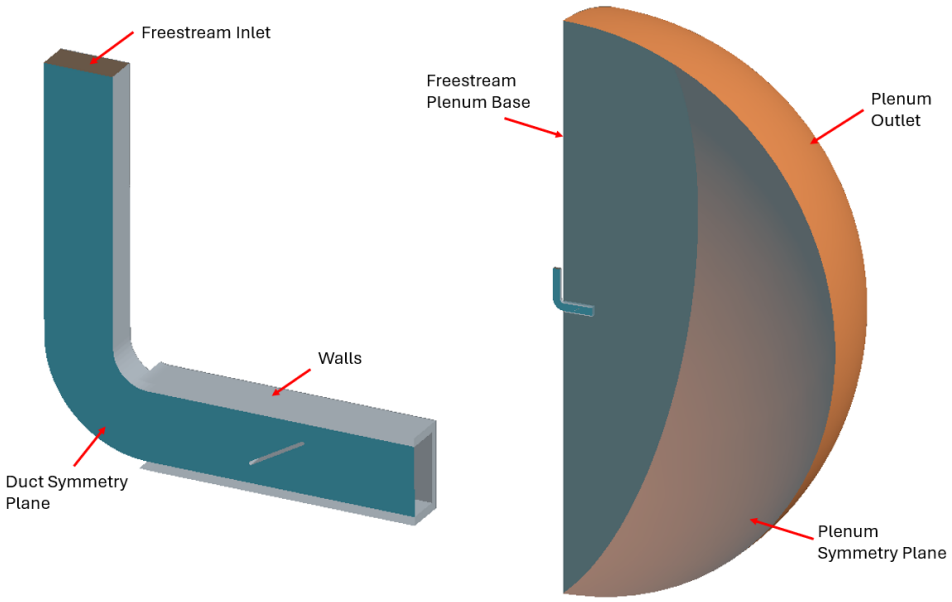

Figure 2.23: Boundary conditions for steady-state analysis for DNC

prepare at best the unsteady simulations, since for DNC calculations it is better to adopt a freestream, exploiting its capabilities of letting acoustic waves pass through, without being reflected back into the computational domain. The same approach has been chosen with the plenum base (the plane that defines the beginning of the plenum, in which the duct is inserted), that was set as a pressure outlet on the prior steady-state simulation and then updated to freestream, to let waves pass through. The plenum outlet instead was set as a pressure outlet and further techniques will be adopted to damp acoustic waves in the unsteady simulation and avoid reflections.

Figure 2.24 shows the steps followed when setting up the proper flow boundaries for the steady-state simulation. In both the steps followed the turbulence specification was set as Turbulence Intensity + Turbulent Length Scale, according to the initial conditions. Table 2.9 resumes the main parameters for the chosen boundaries.

For the plenum, a reasonable value for turbulence intensity and turbulent length scale was chosen, considering that the fluctuations reduce moving towards the outlet boundaries. For this reason a turbulence intensity not higher than 5% was expected, while the turbulent length scale was considered quite higher due to the fact that the flow velocity reduces moving towards the end of the plenum.

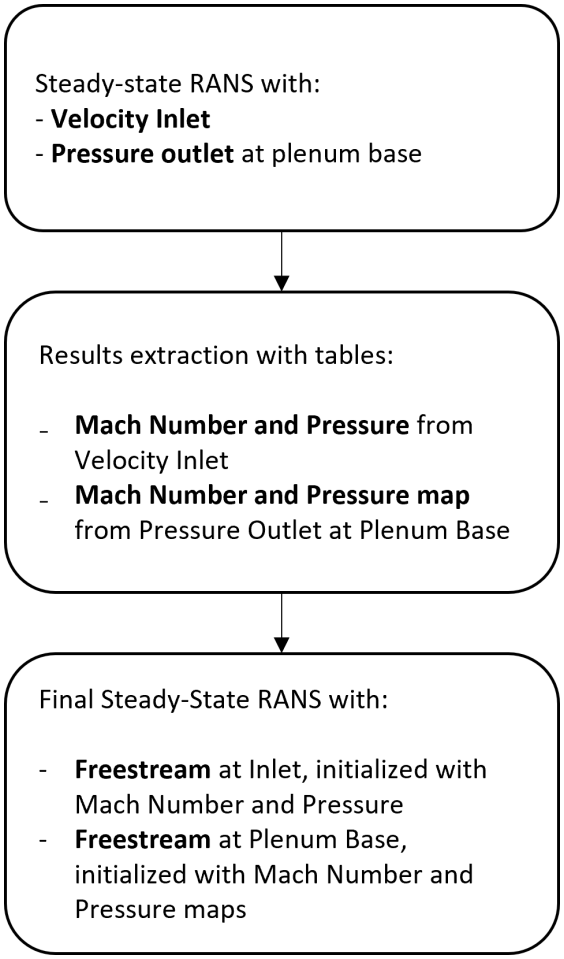

Figure 2.24: Steady-state Boundary Conditions for Inlet-Outlet

2.5 DNC

The results obtained from the steady-state RANS simulation have been taken as a starting point for setting up a DNC simulation, which required specific settings for physics conditions, solvers, stopping criteria and everything related to the live monitoring during the simulation and the post-processing stages. As stated before, the goal of the DNC simulation is to verify if the developed geometry is aligned with literature results. First, it is necessary to discuss the main stages of the DNC methodology.

Inlet Freestream	
Mach Number	0.02167
Pressure	100.1436 Pa
Static Temperature	298.15 K
Turbulence Intensity	0.1
Turbulent Length Scale	0.0056 m
Plenum Base Freestream	
Mach Number	From Initialization Table
Pressure	From Initialization Table
Static Temperature	298.15 K
Turbulence Intensity	0.05
Turbulent Length Scale	0.01 m
Plenum Sphere Pressure Outlet	
Pressure	0.0 Pa
Static Temperature	298.15 K
Turbulence Intensity	0.05
Turbulent Length Scale	0.01m

Table 2.9: Boundary conditions for steady-state analysis for DNC method

2.5.1 Physics Models

The physics models have been updated to properly set up an unsteady simulation. The figure 2.25 shows the updated models on the control panel of Star-CCM+:

The Gas model and the Segregated Fluid Temperature model featured the same settings of the steady-state simulation, while the other common models as Gradients and Segregated Flow have been updated and present some parameters that are crucial to avoid issues of numerical origin during the simulation. To help in wave dissipation and to avoid reflection, the Sponge Layer model has been adopted, which will combine with the non-reflecting boundary property and the mesh coarsening to damp at best the acoustic waves. The table 2.10 resumes the main physics models properties.

The Gradients Limiter Method has been changed to Modified Venkatakrishnan because it offers higher accuracy since it can be less dissipative than the default Venkatakrishnan, especially for DES simulations related to Aeroacoustics. For the

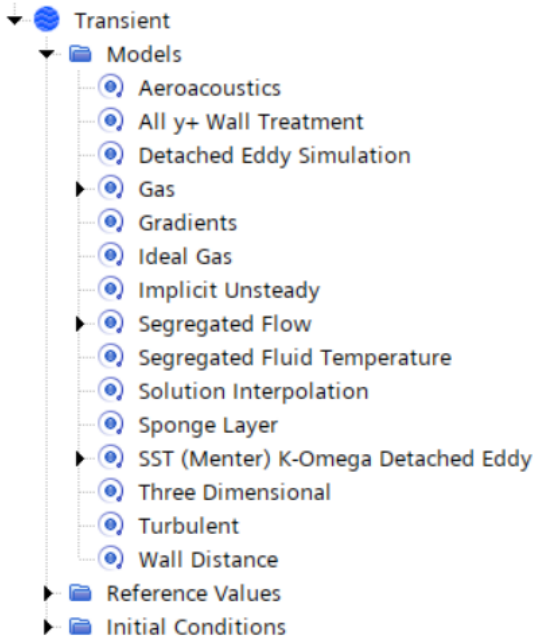

Figure 2.25: Physics Models for DNC simulations

same purposes the TVB Gradient Limiting was enabled since it helps in achieving high-fidelity simulations when DES is adopted for Aeroacoustics analysis. By enabling this parameter the gradients are less limited and the overall accuracy is increased. The Acceptable Field Variation is set to 0.15 to preserve robustness while increasing accuracy.

The convection scheme for Segregated Flow has been switched to MUSCL 3rd-order because it better controls the numerical dissipation and is 3rd order accurate, meaning that it is robust for unsteady flow simulations. The Upwind Blending Factor was set to 0.15 because it needs to be sufficiently low to not reduce accuracy since by tuning this value it is possible to regulate the trade-off between accuracy and robustness of the scheme. The test case has been subjected to the Odd-Even Decoupling phenomena, as will be explained in the results chapter. This phenomena consists in the generation of spurious acoustic waves from sources that are purely numerical and non-physical. To remove these numerical waves, the Unsteady Flux Dissipation Correction was enabled and matched by a proper tuning of the Limiting Acoustic-CFL. The latter has been performed on-the-fly while monitoring since it acts by reintroducing some numerical dissipation which avoids the waves generation from numerical source. However, it is necessary to properly monitor and tune the Limiting Acoustic-CFL since a higher value can damp the sound waves that are targeted during the simulation, thus reducing its accuracy.

The sponge layer model was adopted to suppress potential spurious waves that

Physics conditions		
Gas >Air	Dynamic Viscosity	Sutherland's law
	Specific Heat	Polynomial in T
	Thermal Conductivity	Sutherland's law
Gradients	Limiter Method	Modified Venkatakrishnan
	TVB Gradient Limiting	Enabled
	Acceptable Field Variation	0.15
Segregated Flow	Convection	MUSCL 3^{nd}-order/CD
	Positive Rate Limit	0.2
	Flow Boundary Diffusion	Enabled
	Unsteady Flux Dissipation Correction	Enabled
	Upwind Blending Factor	0.15
	Limiting Acoustic-CFL	4.0
Segregated Fluid Temperature	Convection	2^{nd} order
Sponge Layer	Relative Amount of Suppression	90
	Sponge Layer Thickness	1.59 m
	Boundary Distance Method	Implicit Tree
SST K-omega	Convection	2^{nd} order
	Formulation Option	DDES

Table 2.10: Physics models settings for DNC

could reflect on the outlet boundary surface. Its effect was combined with the mesh coarsening and the boundary conditions. The pressure outlet boundary offers the possibility to enable a non-reflecting condition, however it is highly directional and so it can be less efficient if, as the test case, the plenum outlet surface is spherical. The target of the sponge layer is to completely damp the waves after a certain distance, which corresponds to the Sponge Layer Thickness. That distance was measured starting from the boundary to which the Sponge Layer is applied.

The figure 2.26 shows the area in which the sponge layer was active and reports the Sponge Layer Damping Coefficient which has been evaluated according to the

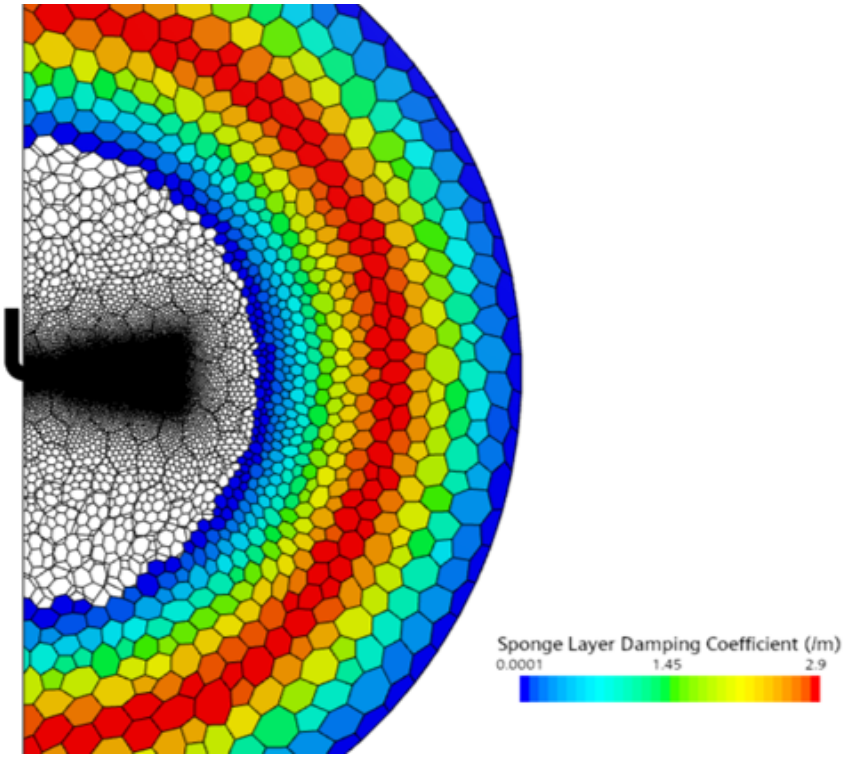

Figure 2.26: Sponge Layer Damping Coefficient

following procedure:

$$\sigma_{sl}(d) = \sigma_{max} \left\{ 1 - cos \left[2\pi \left(1 - \frac{d}{w} \right) \right] \right\} \tag{2.19}$$

where w is the Sponge Layer Thickness reported in table 2.10 and d is the boundary distance, while σ_{max} is the Maximum Damping Coefficient, obtained as:

$$\sigma_{max} = -\frac{c}{w} \log \left(1 - \frac{\alpha}{100} \right) \tag{2.20}$$

where α is the Relative Amount of Suppression reported in table 2.10.

To set up the initial conditions, the solution from steady-state RANS simulation was exported as an XYZ table and introduced in the simulation environment for the DNC. The exported parameters are:

- Pressure
- Specific Dissipation Rate
- Static Temperature

- Turbulent Kinetic Energy
- Velocity on its three components (x, y, z)

Therefore, the Turbulence Specification for the initial condition has been switched from Turbulence Intensity + Length Scale to K + omega.

2.5.2 Solvers

The solver settings should be calibrated right after the Physics conditions, because they are strictly related. Major changes have been introduced if compared to the steady-state setup and all the modifications are presented in the table 2.11.

Physics conditions		
Implicit Unsteady	Time-Step	4.0E-5 s
	Temporal Discretization	2^{nd}-order
Segregated Flow	Implicit Scheme	SIMPLEC
	Velocity Under-Relaxation Factor	1
	Pressure High-Accuracy Temporal Discretization	Optimized 2^{nd}-order (5)
	Pressure Under-Relaxation Factor	1
Segregated Energy	High-Accuracy Temporal Discretization	Optimized 2^{nd}-order (5)
K-omega Turbulence	Under-Relaxation Factor	0.8

Table 2.11: Solvers settings for DNC

First, it is necessary to guarantee a sufficiently small time-step which can be tuned properly according the following procedure:

$$\Delta t \leq \frac{1}{15F} \tag{2.21}$$

where F is the desired frequency of 1000 Hz. However, to be conservative and to reduce numerical dissipation, a smaller value has been chosen with a proper monitoring of the Convective Courant Number to ensure a value of order one around the turbulent area of the flow, as can be appreciated in the figure 2.27.

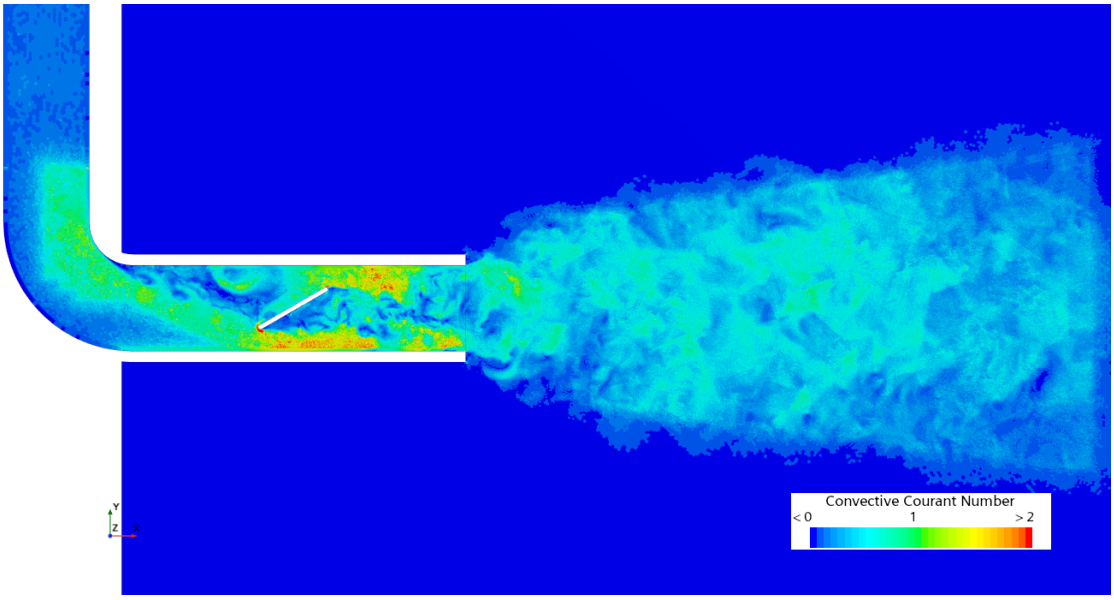

Figure 2.27: Convective Courant Number

About the Segregated Flow Under-Relaxation factors both for Velocity and Pressure, a value of 1 is chosen since the mesh has been proved to be accurate. The High-Accuracy Temporal Discretization was selected to increase the simulation accuracy at very low costs per time step.

2.5.3 Boundaries

The boundary typologies have been already prepared in the steady-state RANS simulation, with a Freestream on both the inlet and the plenum base and a pressure outlet on the plenum sphere. However, after several unsteady simulations, a major change has been adopted for the inlet boundary conditions. In fact, to better uniform with the experimental setup, where a 3 meters long duct was placed before the Simplified HVAC Duct, a short-simulation with periodic boundaries has been prepared to obtain a fully-developed flow. A simple straight duct with the same section as the test geometry has been designed and featured with periodic boundaries. Then, at inlet, the same conditions of the steady-state setup were imposed, to obtain a fully-developed flow which has been used to initialise the final unsteady simulation. The plenum base instead has been directly initialized with a XYZ table extracted from the steady-state simulation. For the pressure outlet at the plenum sphere, the same parameters of the steady-state simulations have been adopted and the Unsteady Non-Reflecting option has been enabled. The latter avoids waves reflection but only if the tangential direction of the waves is

null or very small. For this reason, the Sponge Layer Option was enabled on this boundary. The following table 2.12 resumes all the boundary conditions.

Inlet Freestream	
Mach Number	From Initialization Table
Pressure	From Initialization Table
Static Temperature	From Initialization Table
Turbulence Intensity	0.1
Turbulent Length Scale	0.0056 m
Plenum Base Freestream	
Mach Number	From Initialization Table
Pressure	From Initialization Table
Static Temperature	298.15 K
Turbulence Intensity	0.05
Turbulent Length Scale	0.01 m
Plenum Sphere Pressure Outlet	
Pressure	0.0 Pa
Static Temperature	298.15 K
Turbulence Intensity	0.05
Turbulent Length Scale	0.01 m
Sponge Layer Option	Enabled
Pressure Outlet Option	Unsteady Non-Reflecting
Unsteady Non-Reflecting Length Scale	10.0 m

Table 2.12: Boundary Conditions for DNC

2.5.4 Reports, Monitors and Stopping Criteria

It is important to ensure that the simulation can be monitored on-the-fly and that the important parameters can be monitored and stored to be post processed. Therefore, it is crucial to properly set reports and monitors to control not only these aspects but also if the simulation is converging properly. For this purpose it

is important to setup stopping criteria that control the convergence at each time step.

Some reports were adopted to monitor the CFL, to understand whether the mesh and the solver settings were properly tuned or if they needed updates to catch on convergence. Other reports were needed to check the main flow properties at inlet, properly averaged on mass flow rate, as the pressure, the velocity, the turbulent kinetic energy and the specific dissipation rate. Some reports were required to check on the performance of the simulation and evaluate the computational time. Finally, a report per each probe was set up, to monitor the pressure useful for aeroacoustics evaluation. For each report, a specific monitor and plot were created to store these parameters at each time-step.

The monitors related to the pressure probes are also used to set up the stopping criteria and ensure convergence. All the stopping criteria are included in the table 2.13

Continuity Criterion	Relative Change 0.1	AND Logical Rule Stop Inner Iterations
Energy Criterion		
Tke Criterion		
X-Momentum Criterion		
Y-Momentum Criterion		
Z-Momentum Criterion		
p1 Monitor Criterion	Asymptotic Limit |Max - Min| = 1.0 Pa Number of Samples: 3	AND Logical Rule Stop Inner Iterations
p2 Monitor Criterion		
p3 Monitor Criterion		
p4 Monitor Criterion		
p5 Monitor Criterion		
p6 Monitor Criterion		
p7 Monitor Criterion		
Maximum Inner Iterations	8	OR Logical Rule
Maximum Physical Time	2.0 s	OR Logical Rule

Table 2.13: Stopping Criteria for DNC

2.6 Steady-state analysis for Hybrid approach

To prepare for the simulation stages with the two hybrid approaches, a new steady state simulation was prepared because numerous updates must be implemented compared to the DNC setup. First, the focus of this test was shifted to the far-field noise analysis and the target frequency has been increased to 2 kHz. Therefore, it was necessary to revisit the mesh calibration procedure, with different zones of interest and new strategies to be adopted. The experience gained with the DNC setup and simulation stages helped in introducing many improvements in the steady-state setup, which were expected to affect the further unsteady simulation. The first difference to consider is that the main noise source that affects the far-field is considered to be the surface dipole, since the flow Mach number is much smaller than 0.2 [**10**]. Consequently, the detailed description of the jet development downstream of the duct, where quadrupole noise source are present, was not useful anymore and it was substituted by an area with sufficiently small cells to guarantee the waves propagation up to the microphones. This change of perspective helped in reducing the number of cells. Performing simulations with hybrid approach is expected to be way more efficient than DNC, therefore it was possible to extend the mesh refinement area inside the duct upstream the elbow. Moreover, both the aeroacoustics simulations with the hybrid methods presented in the thesis project share the same steady-state simulation as the initialisation source, since the requirements in terms of mesh are the same. The key guiding principles when setting up a mesh for aeroacoustics simulations with Lighthill or PCW are the following ones:

- Guarantee a very detailed mesh at boundaries, where the noise is produced since the contribution of the turbulent fluctuations can be neglected, as per Tautz [12].
- Ensure a proper description of the flow at edges and at detachment areas since they are crucial for noise generations.
- Guarantee a sufficiently small mesh size to allow waves propagation without any numerical diffusion phenomena.
- Setting up a slow mesh growth up to the outlet boundaries to avoid spurious waves from numerical origin.

Some tuning steps have been taken to find the optimum compromise for steady-state simulation and the procedure is properly described in the following sections. The unsteady simulations with hybrid approach are a lot faster than the DNC approach, therefore it was possible to adopt mesh modifications on-the-fly, without performing again the steady-state precursor analysis.

2.6.1 Mesh preparation

To have a proper mesh for aeroacoustics simulations for cases with low Mach number, as the simplified HVAC duct here presented, it is essential to guarantee the highest accuracy at walls and at edges with the goal to satisfy a very low y+ approach, with y+ values preferably lower than one. Prior to mesh calibration at boundaries, it is necessary to set the proper mesh size both for the core region of the duct and the wave propagation region outside of it, up to the ducts. As stated before, the highest desired frequency f the simulation should capture was set to 2000 Hz, and this value was used to define the proper cell size Δx, while monitoring the Taylor Microscale λ. The mesh size calibration procedure is driven by two equations:

$$\Delta x \leq \lambda \tag{2.22}$$

$$PPW = \frac{(c/f)}{\Delta x} \tag{2.23}$$

where:

- PPW expresses the Points per Wavelength, which is recommended to be $PPW \geq 15$
- c is the sound speed in the far-field

Once a proper value of cell size was obtained from the equation 2.23, the base size was defined. This value guarantees the wave propagation from the duct exit and up to the microphones without spurious and undesired effects. A volumetric control was set up to guarantee this size for both the volume mesh and the surface mesh. The volumetric control was designed as a sphere with a radius that extends 0.1m further than the microphones, to ensure that the mesh coarsening started with some delay. Then, the mesh coarsening increased up to the pressure outlet. To calibrate the mesh size inside the duct, the control on the equation 2.22 was adopted. While running the steady-state RANS simulation, the Taylor Microscale was evaluated inside the duct. As a general rule, the Taylor Microscale is estimated in the bulk region (the core mesh portion far from the walls and before the bend) and, if its value is smaller that the cell size estimated with the equation 2.22, the mesh size inside the duct is set equal or smaller than the Taylor Microscale. However, for this specific test case, the check was done in the turbulent region where the noise generation at surfaces was expected, to ensure the most accurate description. This decision was coupled with the necessity to have a very smooth transition between boundary layer cells and core cells and with the fact that the mesh refinement derived from the DNC setup was set to 0.8 mm. Consequently,

the Taylor Microscale was used to check if the current refinement was good enough in the areas which were more responsible for noise generation.

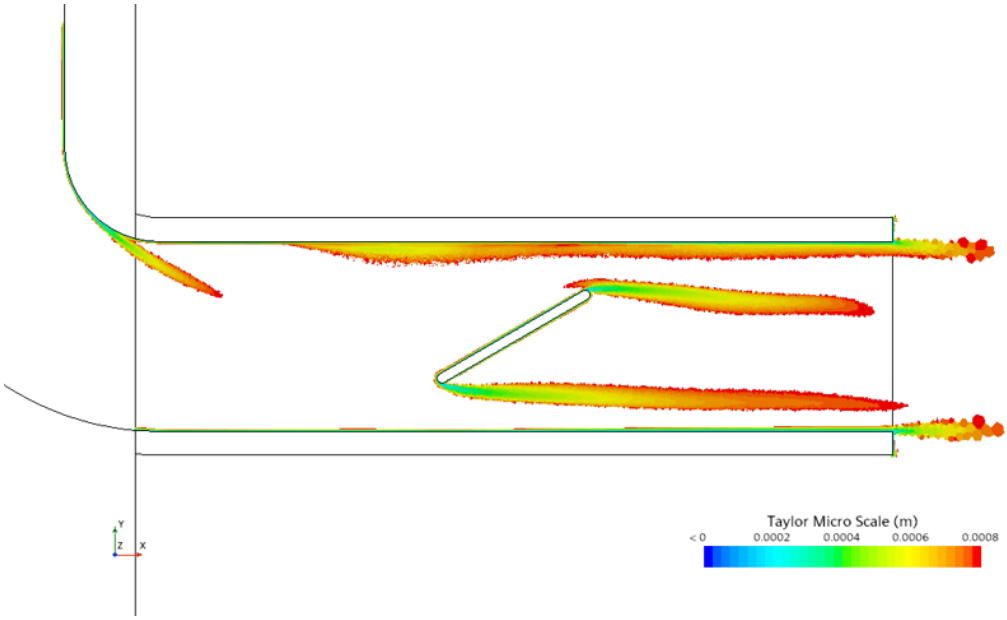

Figure 2.28: Taylor Microscale

The figure 2.28 represents the values of λ up to 0.8mm, while the higher ones are clipped out. It means that the only spots where the inequality 2.22 is not respected are the ones closer to the flap tips and to the top and bottom surfaces. Consequently, around the flap and the surfaces a further refinement of the prism layers will be adopted, thus ensuring a very accurate mesh.

The polyhedral cell type is maintained for the same reasons stated in section 2.4.1 and, overall, no major adjustments have been made to the base mesh options, which are resumed in the table 2.14. For what concerns the duct, it was not necessary to adopt mesh updates when switching from DNC to steady-state for hybrid simulations. However, many updates have been introduced on-the-fly during unsteady simulations, and so they will be explained in section 2.7.

The custom controls have been updated since there is no need for a dedicated refinement in the jet development area. Figure 2.29 shows the new refinement area outside the duct, which is introduced as a volumetric control, as can be observed in table 2.15. Overall, the number of cells amounts to 5.96 millions, which is an important reduction compared to the DNC test case.

For what concerns the prism layers, no further changes were adopted on the steady-state simulation setup, while major changes will be introduced on the fly during simulations with Lighthill Model and PCW Model.

Base mesh options	
Cell type	Polyhedral Cells
Base Size	4E-3 m
Target Surface Size	100%
Minimum Surface Size	10%
Surface Growth Rate	1.1
Volume Growth Rate	1.05
Minimum Face Quality	0.2
Surface Curvature	36 Pts/circle
Surface Proximity	1.0 m search floor, 2 points in gap
Maximum Tet Size	10000% of base
Core Mesh Optimization	1 cycle, 0.4 quality treshold

Table 2.14: Base mesh options for steady-state for Hybrid Methods

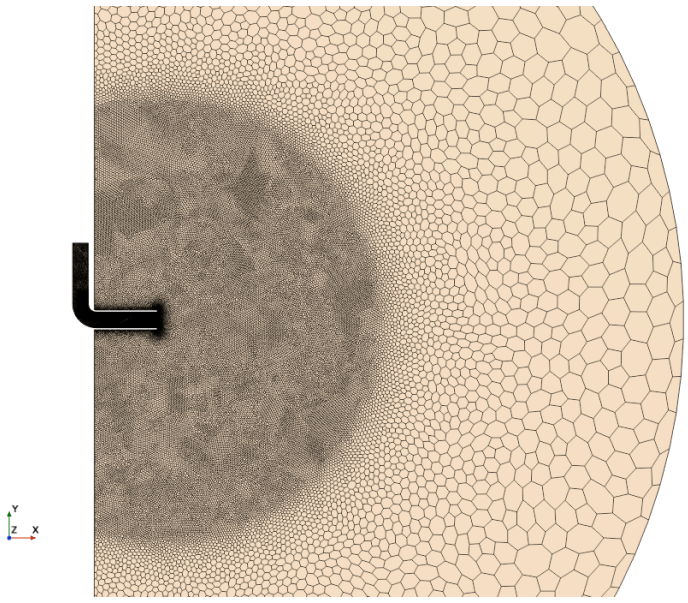

Figure 2.29: Mesh refinement on Plenum for Hybrid Methods

2.6.2 Physics Models and Solvers

The same physics models and solvers as the previous steady-state analysis were adopted since no major changes were needed for the purposes of a steady-state

Custom controls	
Duct refinement, volumetric control	8E-4 m
Wave propagation area, volumetric control	0.01 m
Symmetry plane on duct, surface control	100%
Plenum base and sphere, surface control	5000%
Symmetry plane on plenum, surface control	5000%

Table 2.15: Mesh custom controls for steady-state for Hybrid Methods

analysis. For the physics models, table 2.6 resumes the setup, while for the solvers the section 2.4.3 can be taken as reference.

2.6.3 Boundaries

The boundaries have been updated according to the needs of the acoustics models for hybrid simulations. Contrary to the DNC case, for Lighthill and PCW models the velocity inlet and the pressure outlet are considered non-reflective by default. Therefore, there is no need for sponge layers, non-reflecting options and freestreams. Hence, the inlet boundary was switched back to velocity inlet and it was initialised with the fully developed flow condition used in DNC setup. Both the base and the sphere of the plenum were featured with the outlet pressure boundary. The table 2.16 resumes the boundary conditions.

2.7 Hybrid Methods

To examine the aeroacoustics behaviour of the simplified HVAC duct in the far-field with a frequency resolution of 2000 Hz, several tests have been carried out both with Lighthill Model and PCW Model, starting from the steady-state analysis in section 2.4. As stated before, after the first attempts with the hybrid methods, some important changes at mesh level inside the duct have been adopted. These changes were motivated by the early results obtained during unsteady simulations, because many discrepancies have been obtained when compared to experimental results, as it will be demonstrated in the next chapter. The hybrid methods are characterised by an important speed-up when compared to DNC, bringing results around five times faster, and this allowed them to perform many tests to ensure the highest mesh resolution possible to get optimum results. In terms of setup, both methods share the same mesh and boundary settings, while they slightly differ in terms of physics models and solvers, due to the different aeroacoustics model.

Velocity Inlet	
Velocity	From Initialization Table
Static Temperature	From Initialization Table
Turbulence Intensity	0.1
Turbulent Length Scale	0.0056 m
Plenum Base Pressure Outlet	
Pressure	From Initialization Table
Static Temperature	298.15 K
Turbulence Intensity	0.05
Turbulent Length Scale	0.01 m
Plenum Sphere Pressure Outlet	
Pressure	0.0 Pa
Static Temperature	298.15 K
Turbulence Intensity	0.05
Turbulent Length Scale	0.01m

Table 2.16: Boundary conditions for steady-state analysis for Hybrid Methods

2.7.1 Mesh adjustments

The mesh adjustments involved not only the core refined area but also the prism layer cells dimensions and how they were generated by the mesher tool. First, due to the important cell count reduction from DNC to Hybrid methods, the refinement area inside the duct has been extended to cover the entire bend, to give higher accuracy in flow description since it is crucial to properly describe how the flow hits the walls and the flap. Paired with the refinement area extension, also the prism layers were extended over the correspondent surface, hence allowing to obtain a high-fidelity flow description. Figure 2.30 shows the new mesh inside the duct.

From this image it can be observed how the prism layer thickness has been reduced and the surface in which the low y+ approach is applied has been extended around the entire tip of the duct. The most important change is how the cells at walls were generated. In the mesh preparation stages for DNC, the Prism Layer Mesher has been adopted, while for hybrid simulations the Advancing Layer Mesher has been preferred. The main difference between the two is that the advancing layer mesher generates the layers of prismatic cells from the surfaces and towards the core mesh. This approach generates conformal mesh and more uniform cell

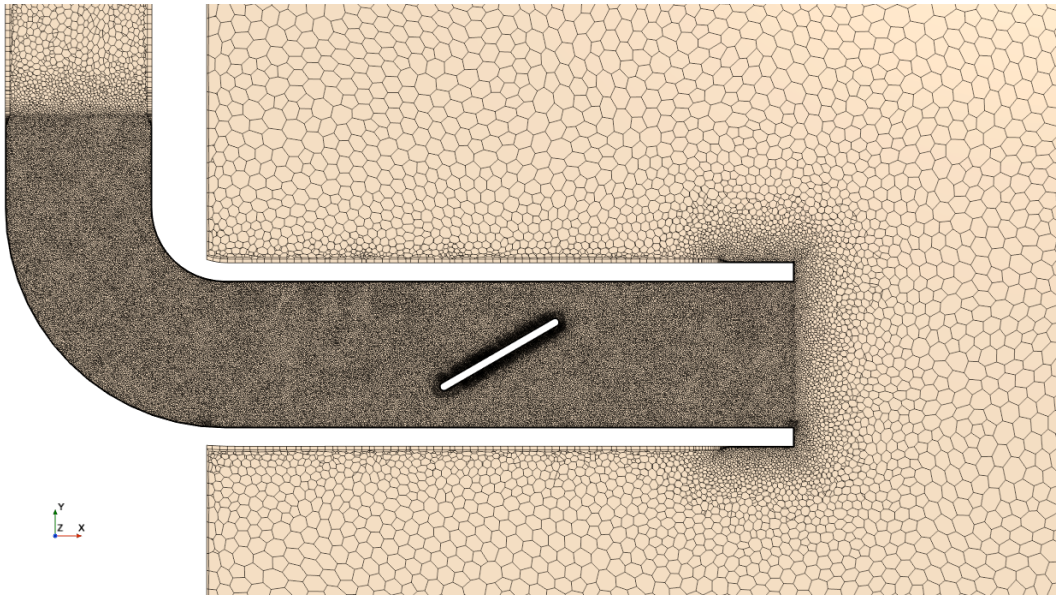

Figure 2.30: Mesh refinement on Duct for Hybrid Methods

layers, especially at sharp edges.

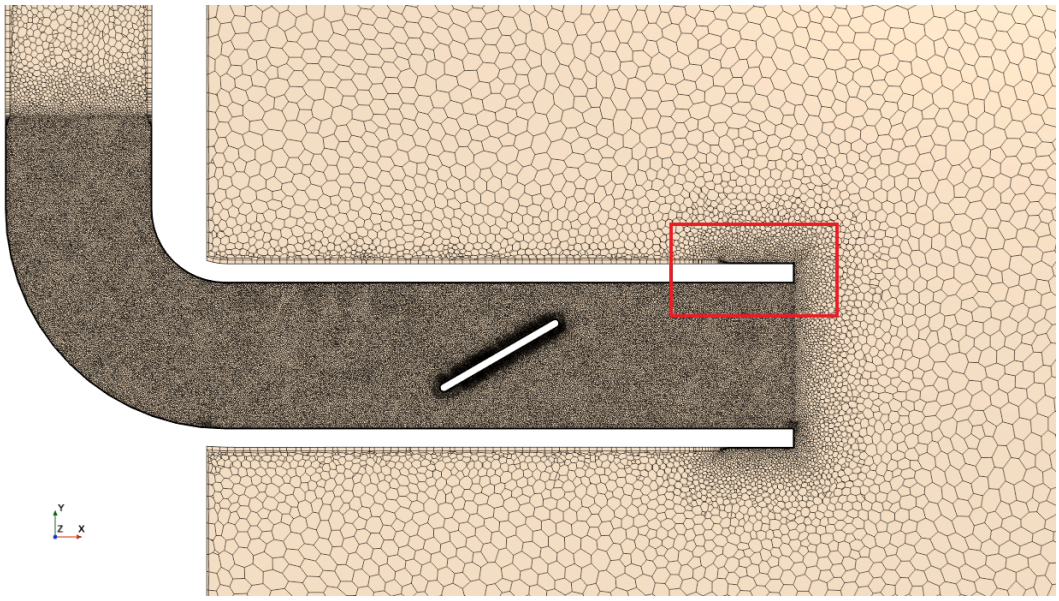

Figure 2.31: Mesh refinement on Duct Edge for Hybrid Methods, examined tip

The images 2.31 and 2.32 focus on the top edge at duct exit and show how the Advancing Layer Mesher was capable of maintaining the 15 layers around the entire

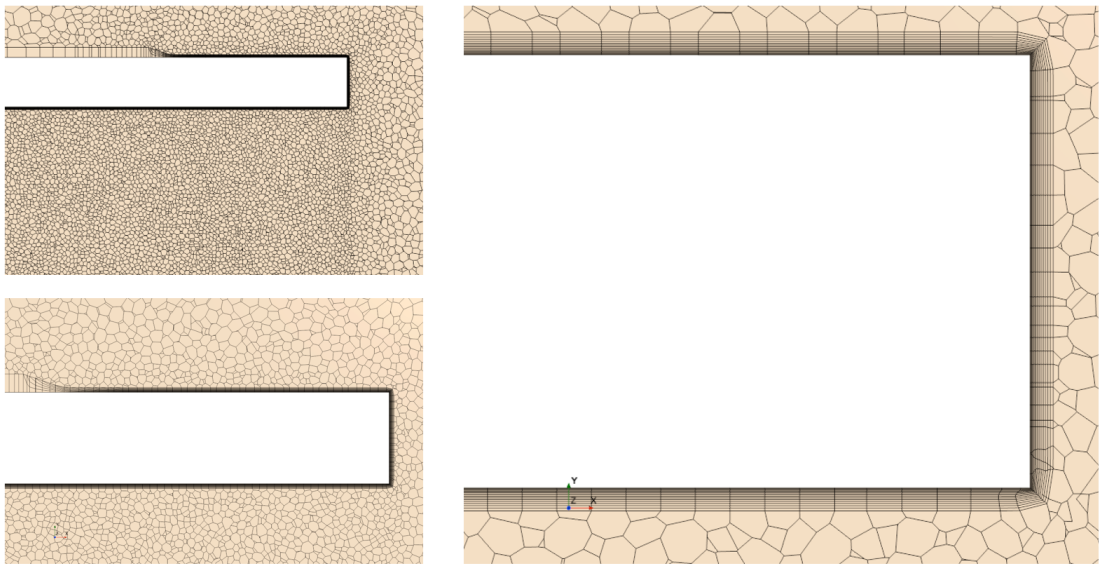

Figure 2.32: Focus on the examined Duct Edge

tip, and avoid collapsing mesh at the sharp edge. The near wall thickness has been further refined to obtain a y+ value below one in every spot of the refinement area. Contrary to DNC strategies, here the main target is the description at walls rather than the jet development so the effort is shifted towards the description of the boundary layer. A further reduction of the boundary layer total thickness required a reduction of the layer thickness also for the surfaces characterised by the high y+ approach (only one wall prism layer), to ensure a smooth transition between layers, as it is depicted in figure 2.33.

The y+ tuning phase was the same described in the equations from 2.12 to 2.17 with a further reduction of the desired y+. Due to the introduction of the fully developed flow at inlet boundary, the velocity inlet has been updated with respect to table 2.3 and the new setup parameters are displayed in the following table 2.17.

Inlet Velocity	7.8307 m/s
Hydraulic Diameter	0.08 m
Kinematic Viscosity at 25°C	1.5520E-05 m^2/s
Air Density at 25°C	1.1839 kg/m^3
Desired minimum y^+	0.09

Table 2.17: Parameters for near wall layer thickness calculation for Hybrid Methods

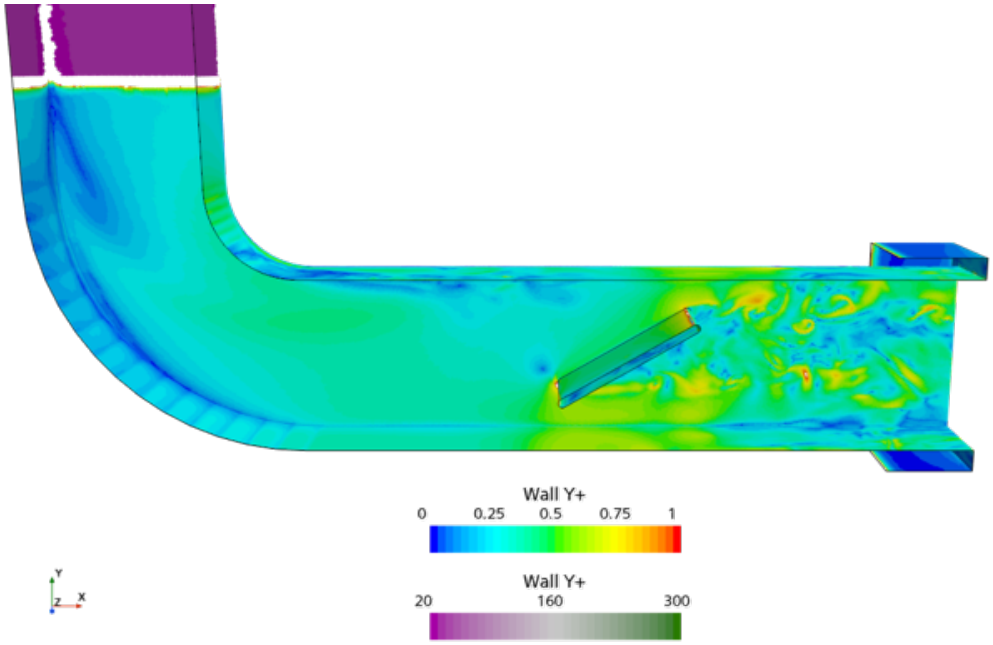

Figure 2.33: Wall y+ for Hybrid Methods Setup

The desired minimum y+ has been set up closer to zero to ensure the results in figure 2.33. This requirement led to major updates in terms of Near Wall Thickness and Total Thickness for the Advancing Layer Mesher, while the other parameters were unvaried. The tables 2.18 and 2.19 respectively resume the settings for both the low and high y+ approaches.

Advancing layer meshing parameters for low y+ approach	
Number of Layers	15
Near Wall Thickness	1.67E-5 m
Total Thickness	5.3E-4 m
Growth Ratio	1.1
Prism Layer Reduction Percentage	1
Gap Fill Percentage	45
Minimum Thickness Percentage	1
Boundary march angle	50 deg

Table 2.18: Advancing Layers parameters for low y+ approach for Hybrid Methods

Advancing Layers parameters for high y+ approach	
Number of Layers	1
Near Wall Thickness	2.5E-3 m

Table 2.19: Advancing Layers parameters for high y+ approach for Hybrid Methods

These updates on the boundary layer description required further adjustments on the surface mesh generation, with appropriate custom controls. On the flap, the surface mesh size has been halved with respect to the duct surface to enhance accuracy in mesh generation, while on the external duct surface the single layer thickness has been further reduced for the sole purpose of allowing a better transition from 15 layers to 1 layer, since no particular effects in terms of aeroacoustics are expected from this external portion of the duct. Table 2.20 shows the custom controls settings. Overall, all the mesh adjustments brought the total number of cells from 5.96 million to 8.3 million.

Surface control on flap	Target surface size	4.0E-4 m
Surface control on duct refinement	Target surface size	8.0E-4 m
Surface control on external duct	Prism layer total thickness	2.0E-3 m

Table 2.20: Custom controls on Duct surfaces for Hybrid Methods

2.7.2 Physics Models

The two hybrid methods share the same Physics models except for the acoustics one, as it can be observed in the following figures 2.34 and 2.35, which in one case is the Lighthill Wave and in the other the Perturbed Convective Wave, therefore a common description for the two is presented in this section.

The first difference with DNC was the choice of the Constant Density model. Working with very low Mach numbers flow opens the possibility to consider the flow as incompressible, improving the performances of the simulation and simplifying the calculations. The Gas model settings were maintained according to previous tests to have uniformity in flow description. About the gradients, the default Venkatakrishnan Limiter Method has been adopted since the results provided are good. However, as it has been made in DNC stages, the Modified Venkatakrishnan Limiter Method can be preferred since it can be less dissipative. The TVB Gradient Limiting and Acceptable Field Variation settings were confirmed from the DNC

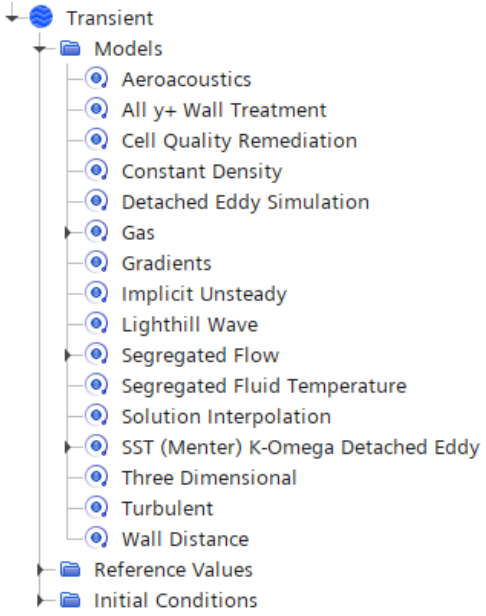

Figure 2.34: Physics Models for Lighthill Method

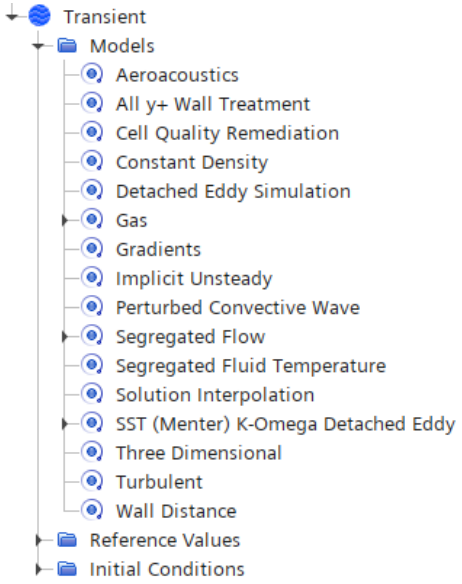

Figure 2.35: Physics Models for PCW Method

setup, without any change. The same happened for the Segregated Flow settings with the MUSCL 3rd-order/CD Convection and an Upwind blending factor of 0.15, since the trade-off between accuracy and robustness of the scheme is balanced. For the SST K-omega model, the DDES formulation option was maintained. This could be switched to IDDES if a smoother transition from RANS to LES is required, but, due to the accuracy in existing mesh, this switch was not implemented for the test case. The Sponge Layer Model is not present anymore, first because it requires Ideal Gas or Real Gas equation to be implemented, then because it would not be useful since the inlet and outlet boundaries are considered as non reflective as default. Table 2.21 resumes the common physics condition settings of between the hybrid Methods:

Two different physics models are adopted for the Acoustics Wave:

- Lighthill Wave
- Perturbed Convective Wave

and the settings options are described in table 2.22.

For both of them the relevant parameter is the sound speed, which was chosen as the same one established at the beginning of the project. About the initial conditions, two different approaches have been used:

Physics conditions		
Gas > Air	Dynamic Viscosity	Sutherland's law
	Specific Heat	Polynomial in T
	Thermal Conductivity	Sutherland's law
Gradients	Limiter Method	Venkatakrishnan
	TVB Gradient Limiting	Enabled
	Acceptable Field Variation	0.15
Segregated Flow	Convection	MUSCL 3^{nd}-order/CD
	Positive Rate Limit	0.2
	Flow Boundary Diffusion	Enabled
	Unsteady Flux Dissipation Correction	Enabled
	Upwind Blending Factor	0.15
	Limiting Acoustic-CFL	4.0
Segregated Fluid Temperature	Convection	2^{nd} order
SST K-omega	Convection	2^{nd} order
	Formulation Option	DDES

Table 2.21: Physics Models in common between Hybrid Methods

Physics conditions		
Lighthill Wave	Far-field Sound Speed	346.59 m/s
	Secondary Gradients	Enabled
Perturbed Convective Wave	Reference Sound Speed	346.59 m/s
	Secondary Gradients	Enabled

Table 2.22: Acoustics Wave model options for Hybrid Methods

- The Lighthill Method has been initialised with steady-state RANS results, presented in section 2.6.
- The PCW Method has been initialised with Lighthill Method results, to speed up convergence and to solve some instability phenomena that were observed

when initialising the simulation from steady-state RANS results.

For both the cases, the exported parameters used to initialise the stimulation are:

- Pressure
- Specific Dissipation Rate
- Static Temperature
- Turbulent Kinetic Energy
- Velocity on its three components (x, y, z)

The instability observed when initialising the PCW Method with steady-state results was eventually resolved by starting the Perturbed Convective Wave solver with some delay and introducing a ramp function for acoustic damping at duct surfaces at the very beginning of the simulation. Future studies could focus on this topic.

2.7.3 Solvers

According to what has been observed for the Physics Models, both methods shared the same solvers settings except for the acoustic wave ones. The core concept of the hybrid methods is that the acoustic wave solver is decoupled from the fluid dynamics one, which means that differences in terms of convergence can be observed and the acoustic solver could diverge even if the fluid dynamics of the system is properly described. Therefore, it is crucial to pay attention to the acoustic wave solver settings, which need to be coupled to a tailor-made mesh for the aeroacoustics analysis. The table 2.23 resumes the common solver settings between the two hybrid methods.

To give an additional speed-up to the simulation around one second per timestep, the Segregated Energy Solver has been frozen, since it has been observed how the Temperature Variation in the domain is in the range of 0.01K, so it can be considered negligible. However, it is suggested to freeze the energy solver once it has been proved that the temperature variations are not significant. The tuning process for the Time Step was strictly coupled with the mesh one since it is necessary to guarantee at least 15 time steps per period, therefore the Time Step size was tuned according to the equation:

$$\Delta t \leq \frac{(1/f)}{15} \tag{2.24}$$

Solvers Settings		
Implicit Unsteady	Time-Step	3.0E-5 s
	Temporal Discretization	2^{nd}-order
Segregated Flow	Implicit Scheme	SIMPLEC
	Velocity Under-Relaxation Factor	1
	Pressure High-Accuracy Temporal Discretization	Optimized 2^{nd}-order (5)
	Pressure Under-Relaxation Factor	1
Segregated Energy	Solver Frozen	Enabled
K-omega Turbulence	Under-Relaxation Factor	0.8

Table 2.23: Solver Settings in common between Hybrid Methods

where f is the highest frequency desired, which is 2000 Hz.

For what concerns the Acoustics solver, two different solvers options are available:

- Acoustic Wave
- Perturbed Convective Wave

The following table 2.24 resumes the main differences between the two solvers.

It is observable that the main difference between the two solvers is related to the parameters for the convergence tolerance which, in both the cases, have been left as default. What has been observed is that the PCW Model required more attention because, at the same initialization, it could lead more easily towards instability when compared to the Lighthill Model. However, referring to the project test case, the Perturbed Convective Wave Solvers converged faster than the Acoustic Wave one with proper settings. It could be useful to set up a start time for the acoustic solver, to avoid the acoustics calculations when the flow inside the domain is not yet stable. Another parameter that can be properly tuned is the Newmark Alpha Parameter, which could vary in the range $[-0.33; -0.05]$ and it is capable of damp spurious high frequencies. It is suggested to switch towards more negative values when approaching test cases with rotating geometries [10].

Acoustics Solver Settings		
Acoustic Wave	Newmark Alpha Parameter	-0.05
	Convergence Tolerance	0.001
	Minimum Convergence Tolerance	1.0E-10
	Inner Iterations	5
	Start Time	0.0s
Perturbed Convective Wave	Newmark Alpha Parameter	-0.05
	Convergence Tolerance	1.0E-5
	Inner Iterations	5
	Start Time	0.0s

Table 2.24: Acoustic Solvers settings for Hybrid Methods

2.7.4 Boundaries

Both the Hybrid Methods feature a default non-reflecting condition for both Velocity Inlet and Pressure Outlet, therefore the setup for boundary conditions was easier than the DNC approach. The Inlet initialisation came from the fully-developed flow simulation and all the other flow boundaries parameter was set-up accordingly to DNC, to maintain a certain uniformity between the two cases. The following table 2.25 resumes the main settings for the flow boundaries.

About the duct walls, the Adiabatic No-Slip Smooth Wall condition was maintained and no Acoustic Damping Specification was given, since the aluminium sheets of the experimental setup were considered as purely reflective. Even if it is not useful for the test case, it is possible to consider the presence of external noise sources or some acoustics damping in the region and they can be properly specified in the Physics Values of the Regions section.

2.7.5 Reports, Monitors and Stopping Criteria

The hybrid methods feature 153 microphones at a distance of 1m from the duct exit, therefore each microphone was provided with a Report, a Monitor and a Monitor Plot. As it has been done for the DNC setup, a group of reports and monitors was set up to control the flow parameters and the calculation time. About the Stopping Criteria, no difference was required with respect to the DNC, except the fact that the probes were not involved anymore in the control chain. The table 2.26 resumes the stopping criteria.

Velocity Inlet	
Velocity	From Initialization Table
Static Temperature	From Initialization Table
Turbulence Intensity	0.1
Turbulent Length Scale	0.0056 m
Plenum Base Pressure Outlet	
Pressure	From Initialization Table
Static Temperature	298.15 K
Turbulence Intensity	0.05
Turbulent Length Scale	0.01 m
Plenum Sphere Pressure Outlet	
Pressure	0.0 Pa
Static Temperature	298.15 K
Turbulence Intensity	0.05
Turbulent Length Scale	0.01 m

Table 2.25: Flow Boundary Conditions for Hybrid Methods

Continuity Criterion	Relative Change: 0.1	AND Logical Rule Stop Inner Iterations
TKE Criterion		
X-Momentum Criterion		
Y-Momentum Criterion		
Z-Momentum Criterion		
Maximum Inner Iterations	8	OR Logical Rule
Maximum Physical Time	2.0 s	OR Logical Rule

Table 2.26: Stopping Criteria for Hybrid Methods

Chapter 3

Results

3.1 DNC results

To examine the results from the Direct Noise Computation it was necessary to properly setup post-processing contour plots and monitor plots with the aim of gaining all the relevant information both for fluid dynamics and aeroacoustics. Several tests have been carried out but, for the sake of simplicity, only the latest results obtained will be displayed in this section, alongside the main issues faced during simulation stages which are a relevant discussion topic. The Direct Noise Computation was expected to be expensive in terms of required resources and it confirmed the expectations, as it can be observed in figure 3.1.

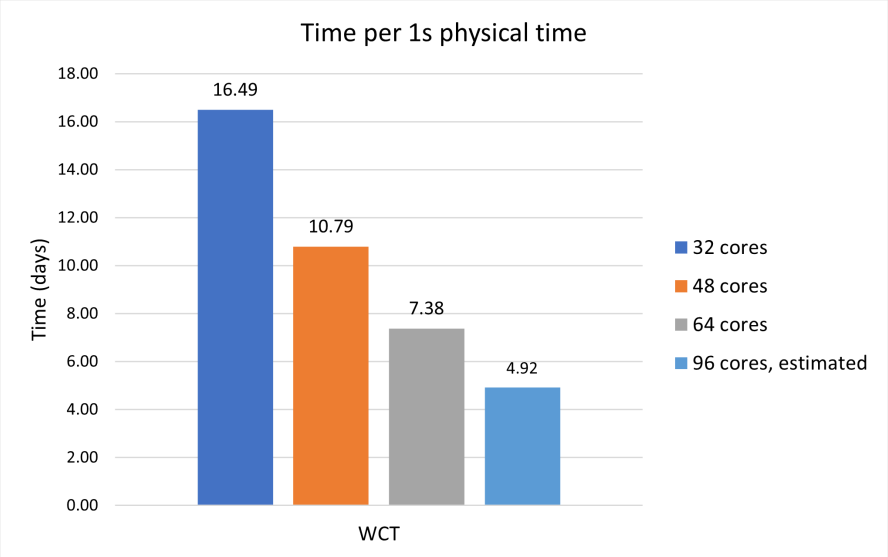

Figure 3.1: Wall clock time of DNC per 1s physical time

The histogram shows wall clock time results for different simulations run on different numbers of CPU cores, with a scalability of 16 cores. As expected, the computational time for the DNC methodology is expensive, and it was not sustainable to run a simulation over a number of cores smaller than 64. Moreover, the setup for DNC is calibrated to a desired frequency of 1000 Hz, meaning that reaching 2000 Hz with DNC would not be feasible, since a further mesh refinement would be required. It is evident how the switch to hybrid methods is necessary from a computational point of view. The results presented in this section come from a simulation that has been run on 64 cores from 0s to 1.635s.

Thanks to Jaeger et al. [6] research, a comparison with experimental data has been made possible, both for fluid dynamics and for Sound Pressure Level (SPL), with the latter obtained from pressure waves captured at probes. In the images 3.2 and 3.3 it is possible to observe the velocity components along the x-axis and y-axis respectively on left and right. From top to bottom, the images show the experimental results that were obtained with PIV and two simulation results that were obtained by Jaeger et al. [6] with Star-CD and Powerflow. The case reported in literature adopted a different reference system, where the x-axis direction in the simulation reference frame is the z-axis direction in theliterature case, and the y-axis direction from simulation corresponds to the minus y-axis direction from literature. However, the reference frame of the simulation environment will be considered as the main one in the following discussion.

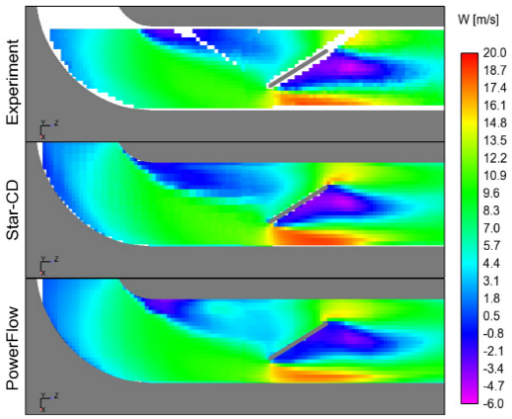

Figure 3.2: Time-averaged velocity component along the x-axis from literature [6]

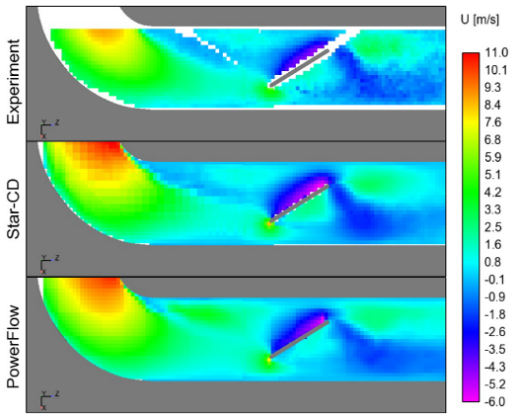

Figure 3.3: Time-averaged velocity component along the y-axis from literature [6]

The goal of the DNC in terms of fluid dynamics was to be aligned with the experimental results, in particular with the description of the detachment and the recirculating areas, as long as the high-velocity zones. Considering the discrepancies

in terms of reference systems, it was important to uniform the colour map and the scalar field range between simulation results and literature reference, to allow a proper comparison from a macroscopic perspective. Moreover, it should be considered that literature results and simulation results are time averaged on different time intervals, and this is the reason why the comparison can be made only from a qualitative point of view, to understand if the macroscopic behaviours of the flow have been described by the simulation. As it can be observed in the figures 3.4 and 3.5, the same contour plots as literature are presented. Referring to the component along the x-axis, the detachment at the elbow was properly described and it was followed by a recirculation zone as in experiments.

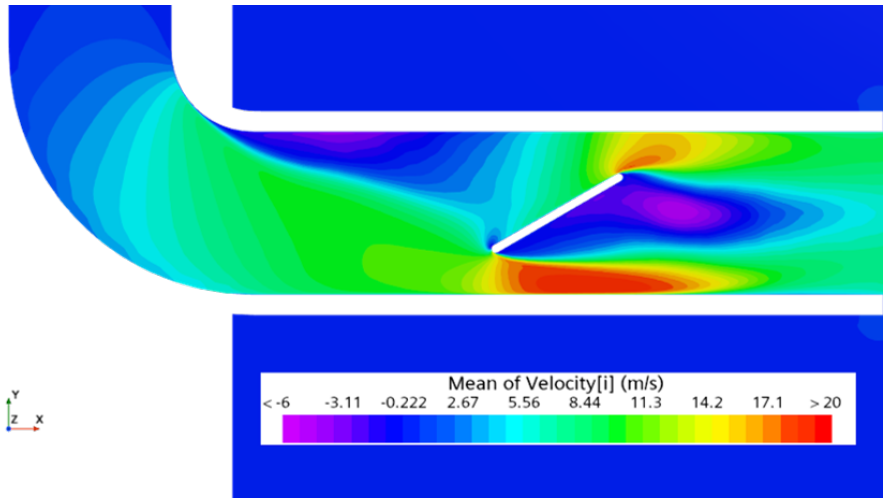

Figure 3.4: Time-averaged velocity component along the x-axis in DNC environment

In simulation results, a negative velocity zone (blue contours) that links the recirculation zone and the bottom tip of the flap was observed, while in figure 3.2 it is slightly observed only in the results from PowerFlow. The behaviour around the flap has been accurately described since the recirculating zone downstream the flap was depicted with high precision and the high-speed zone at the bottom part of the duct was coherent with literature, as long as the pinnacle at the higher flap's tip. Considering instead the component along the y-axis, the simulation results presented high-fidelity with literature reference (figure 3.3) in the flow description both in the area around the flap and at the elbow's detachment point. In particular, the recirculating area on the top surface of the flap was properly described. Some small difference in terms of intensity can be observed in both the velocity components, since the fully-developed flow that has been adopted at inlet boundary is an estimation of the start-up duct presented in the experimental setup in figure 2.2.

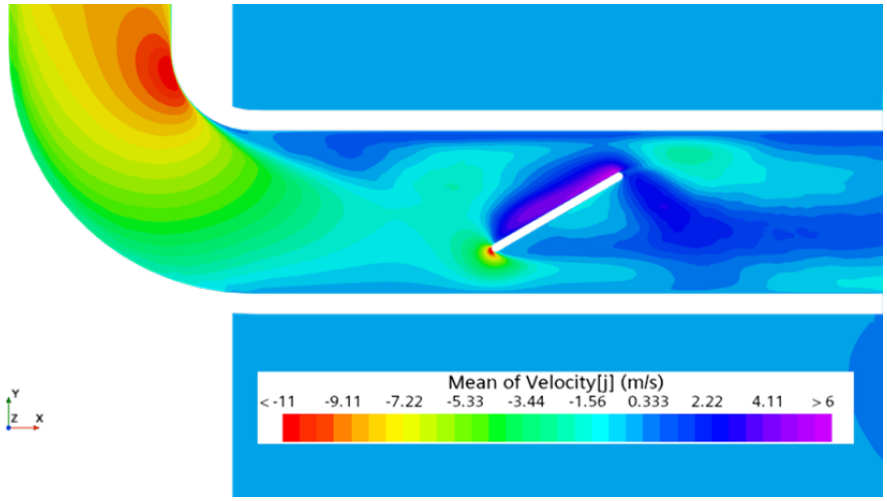

Figure 3.5: Time-averaged velocity component along the y-axis in DNC environment

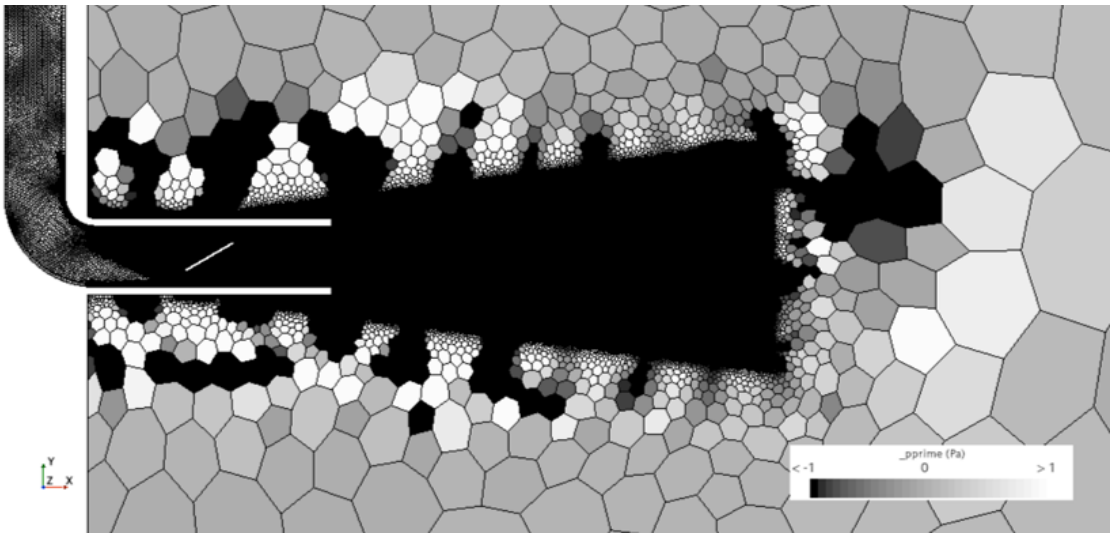

Figure 3.6: Odd-Even Decoupling phenomena

One of the main results related to aeroacoustics is the difference between the pressure value and the field mean pressure p'. This parameter is evaluated from the equation 2.1, which allows to understand the acoustic wave propagation inside the domain. In the early results a non-physical phenomenon was observed, with the name of Odd-Even Decoupling phenomena, as depicted in figure 3.6. This phenomena consists in the formation of acoustic waves that moves in the opposite direction compared to the flow, which are generated by numerical issues. In the

test case, these waves were generated at the very end of the jet refinement area and propagated around the refinement zone. As it can be observed, the mesh grid has been enabled on the contour plot to examine the cells involved in the generation of the numerical waves. Specifically, a group of cells at the transition between the plenum cells and the jet refinement area was spotted as wave propagation sources. Therefore, the choice of smoothing the transition and thus maintaining smaller mesh for a longer portion of the plenum region was inevitable.

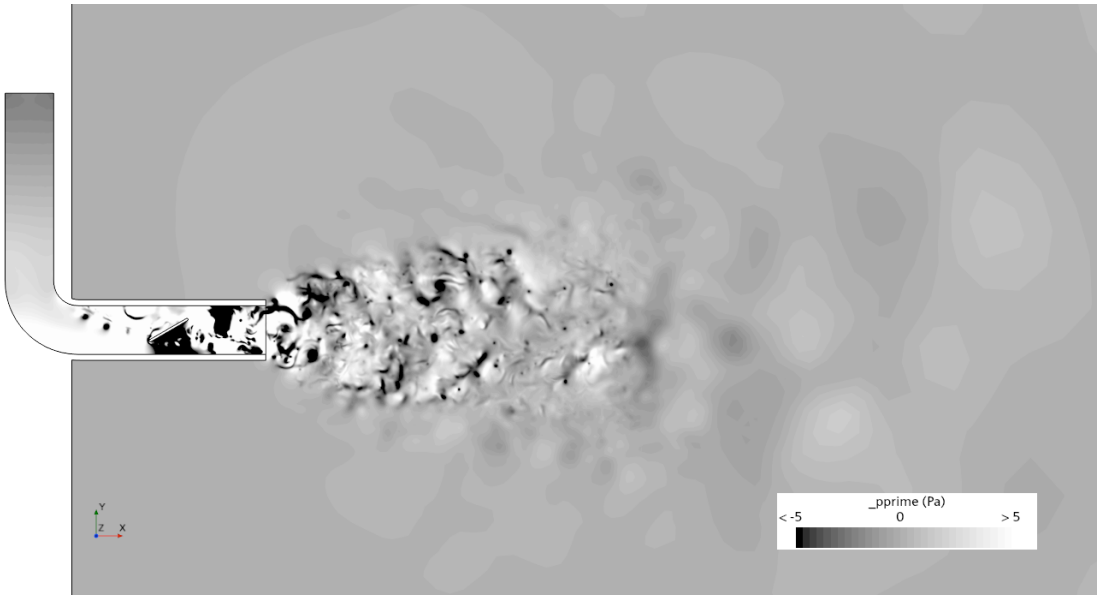

Figure 3.7: p' at1.685 s within the range [-5 Pa; 5 Pa]

The issue was solved by smoothing out the mesh transition and setting a low mesh growth rate as explained in the section 2.4.1, along with the enabling of the UFDC, according to section 2.5.1. No spurious waves were detected in the simulation domain anymore. The figure 3.7 and 3.8 shows the flow propagation from the duct to the plenum and the pressure waves within two different range variations. In the picture 3.8, where the delta of pressure was narrowed to [-1 Pa; 1 Pa], black and white wave fronts are more visibile. In picture 3.9, where the scalar field varied between [-0.1 Pa; 0.1 Pa], the wave fronts are clearly distinguishable, and no spurious waves can be observed.

As stated before, Jaeger et al. [6] provided results in terms of Sound Pressure Level (SPL) plots in the domain of frequencies. Specifically, the signals at microphones 1, 2 and 6 were processed and the results can be observed in figure 3.10. The curve related to the experimental results has been extrapolated to compare it with the simulation results, which where subjected to a sensitivity analysis to find the proper tuning for Fast Fourier Transform (FFT) analysis. Within the

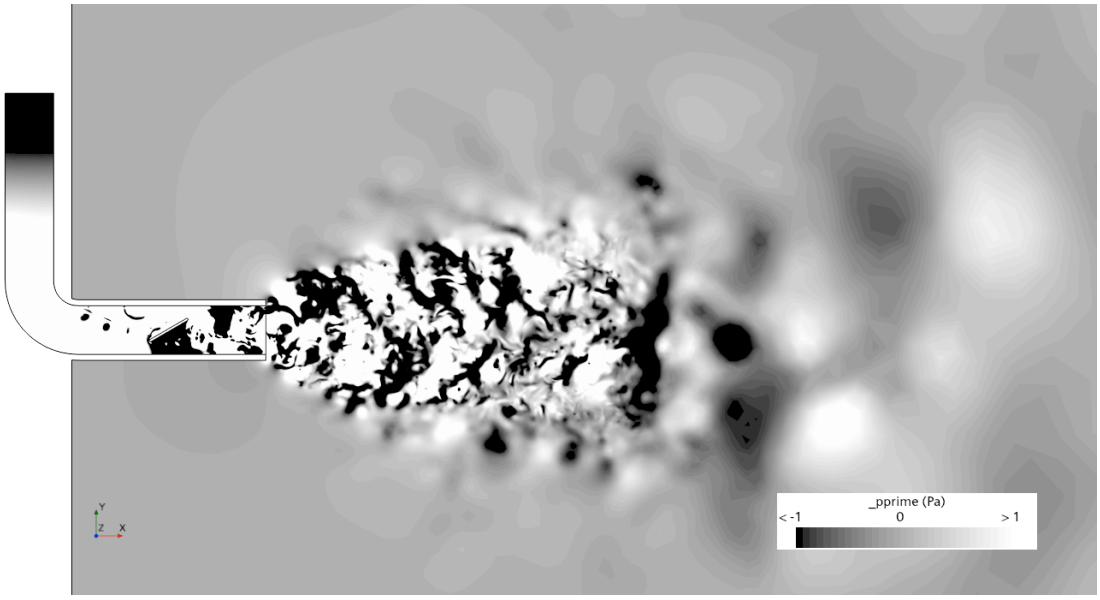

Figure 3.8: p' at 1.685 s within the range [-1 Pa; 1 Pa]

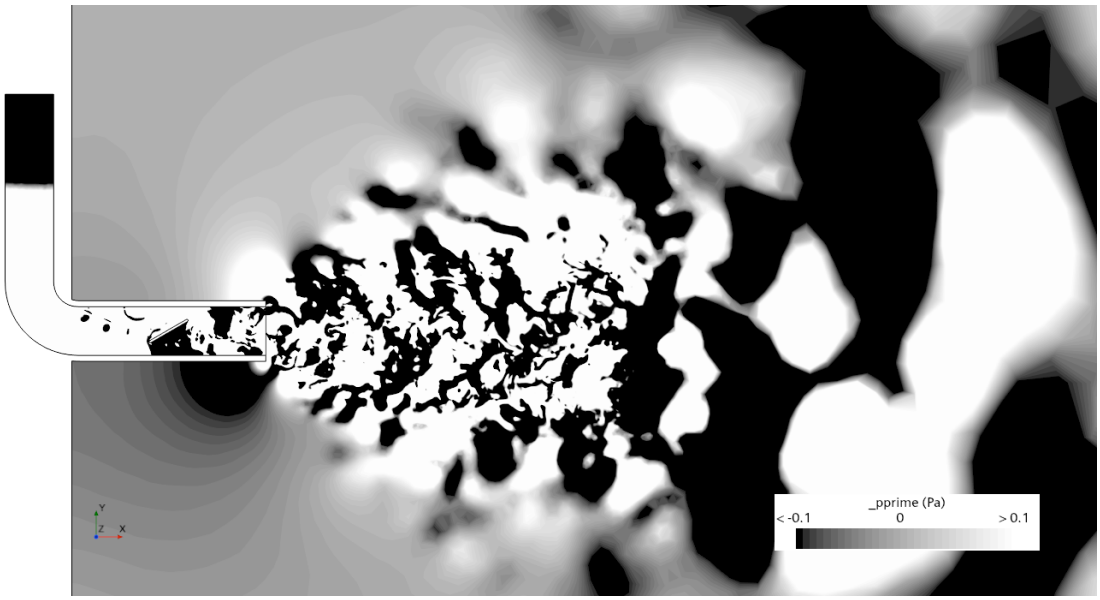

Figure 3.9: p' at 1.6855 s within the range [-0.1 Pa; 0.1 Pa]

Star-CCM+ environment, it was possible to directly extract SPL plots once the main parameters have been inserted:

- The start time and the cut-off time for the specific sampled time

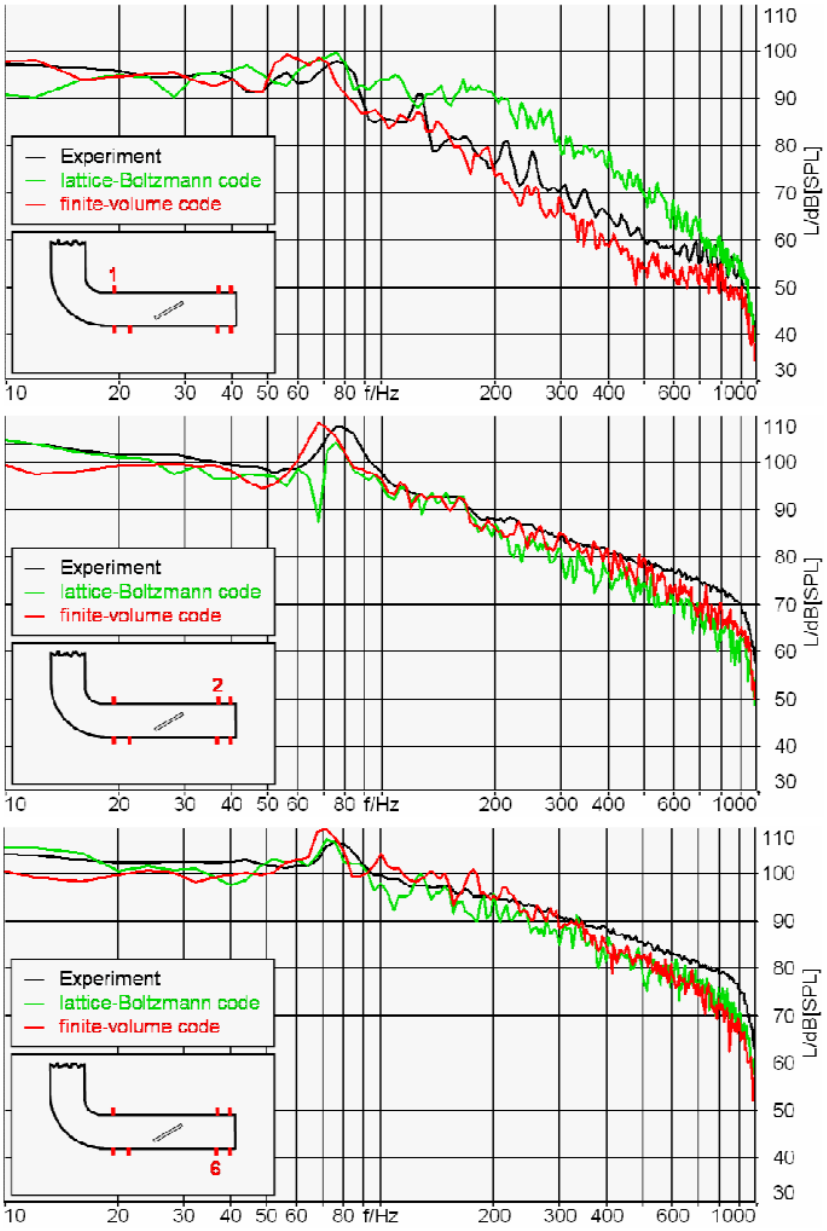

Figure 3.10: SPL plots for microphones n. 1, 2, 6 from literature [6]

- The amplitude function to evaluate, which is the Sound Pressure Level (dB)
- The frequency function which is the frequency (Hz)
- The number of analysis blocks in which the sampled time is divided
- The overlap factor to establish how much the analysis blocks are overlapped

- The window function for the specific weighting technique

For each of the examined probes (figure 3.11), these parameters needed to be set and the adopted settings are presented in table 3.1, and the results obtained are presented in the figures 3.12, 3.13 and 3.14, where a comparison with experimental results has been performed.

Start Time	0.9s
Cut-off Time	1.635s
Amplitude Function	Sound Pressure Level (dB)
Frequency Function	Frequency (Hz)
Analysis Blocks	2
Overlap Factor	50%
Window Function	Hann

Table 3.1: FFT analysis settings

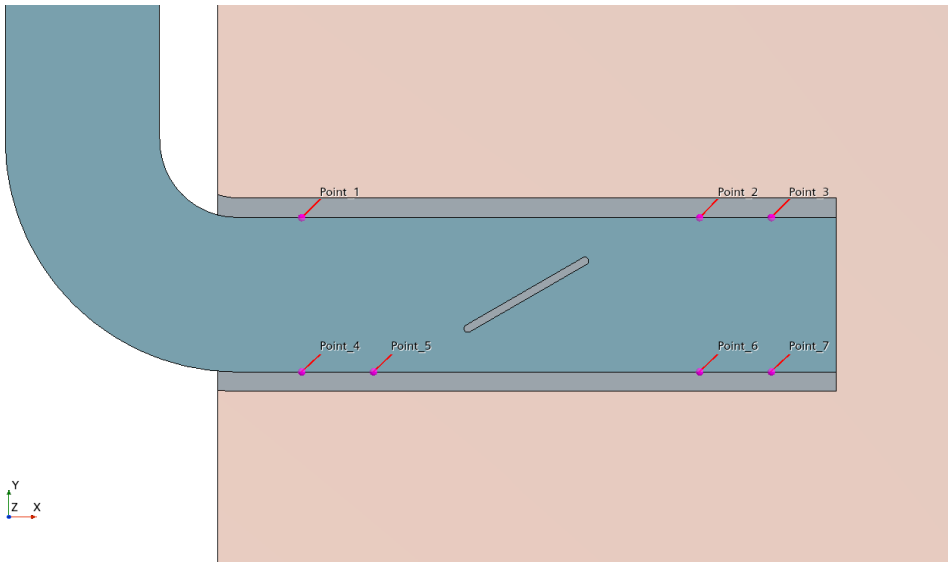

Figure 3.11: Probes positions inside the duct

The plots showed good correlation with the experimental results for the entire frequency range, meaning that the mesh was properly calibrated and the simulations' parameters were accurately set. Some discrepancies were observed at low frequencies (below 100 Hz), especially for the microphone 1 where the highest margin was

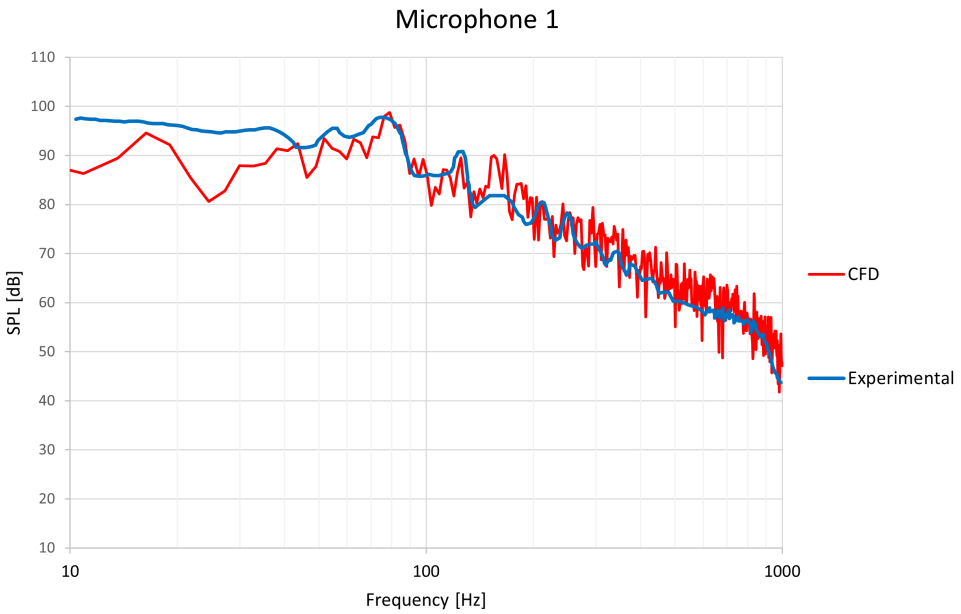

Figure 3.12: SPL plots for microphone 1 of figure 3.11

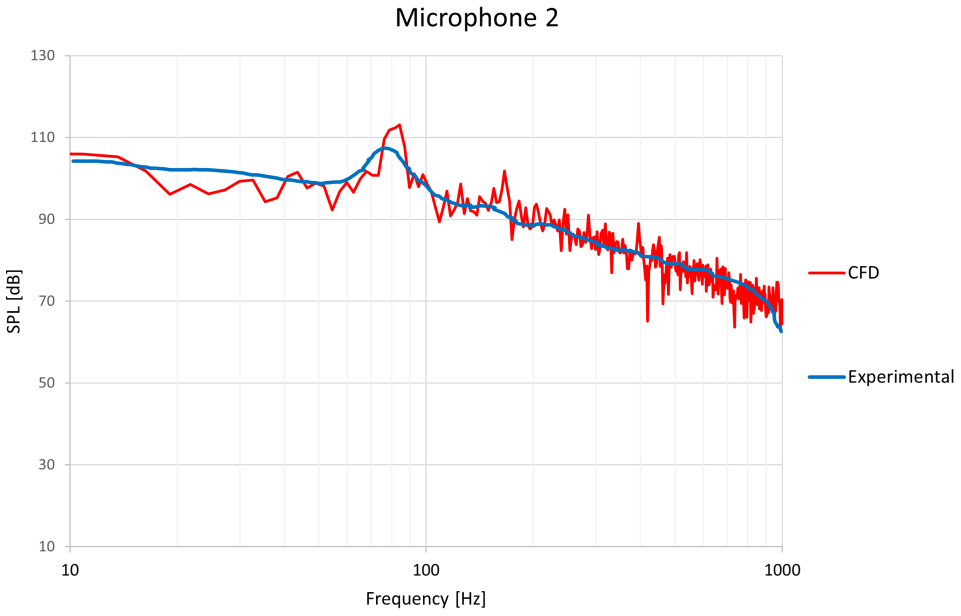

Figure 3.13: SPL plots for microphone 2 of figure 3.11

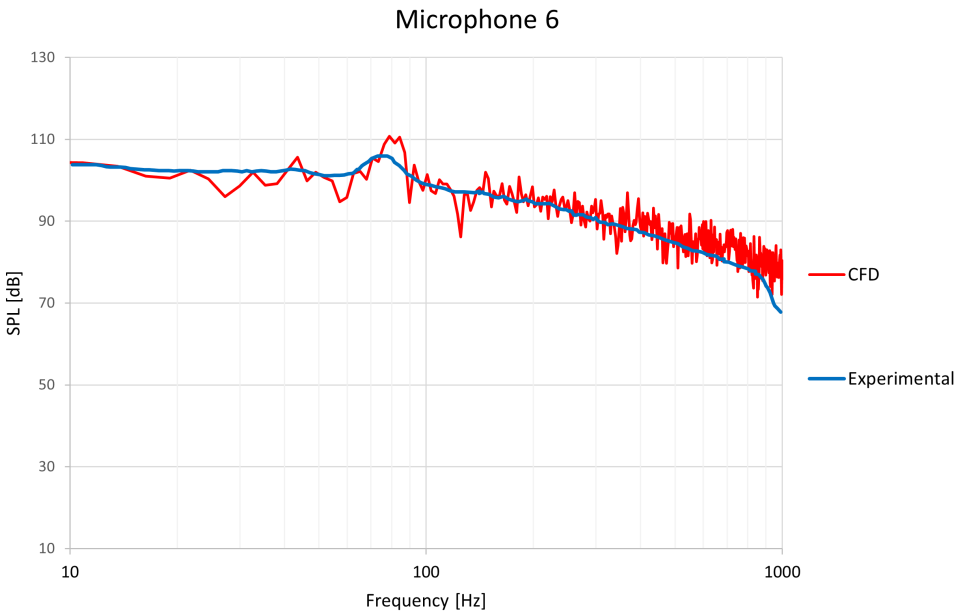

Figure 3.14: SPL plots for microphone 6 of figure 3.11

around 20 dB for waves at 25 Hz. However, due to the small sampled time, it is not possible to get the highest accuracy for very low frequencies, nevertheless the peak around 80 Hz was described correctly for all the microphones. Over the 100 Hz threshold, the CFD curve was very accurate when compared to the experimental one. The CFD curve is more perturbed because it has a higher spectral resolution, while the experimental curve has been averaged in post processing stages with a specific method that was not explained in the paper reference [6].

3.2 Hybrid Methods results

To investigate the aeroacoustics behaviour in the far-field with a desired frequency of 2000 Hz, the hybrid methods based on Lighthill Model and Perturbed Convective Wave model were adopted. Both models provided an important speed-up from the calculation point of view, allowing to perform many simulations and test different setup conditions to find the optimum setup for a standard simulation methodology. For both methods, the final simulations presented in this chapter have been run on 256 cores. The PCW model proved itself to be 15-20% slower, compared to Lighthill model, however it offered the possibility to monitor many field functions, which were useful in refining the simulation setup. During the simulation it has been observed that the time per timestep increased with a linear trend therefore,

to have a proper comparison, both models have been run from 0s to 2s. Figure 3.15 illustrates the time required by the two models to simulate 1s of physical time. Differently from the DNC, the hybrid methods were capable to provide reliable results on a daytime, since less than a day is sufficient to cover more than half a second. This aspect allowed to optimize at best the mesh and the setup by a continuous monitoring of the simulations.

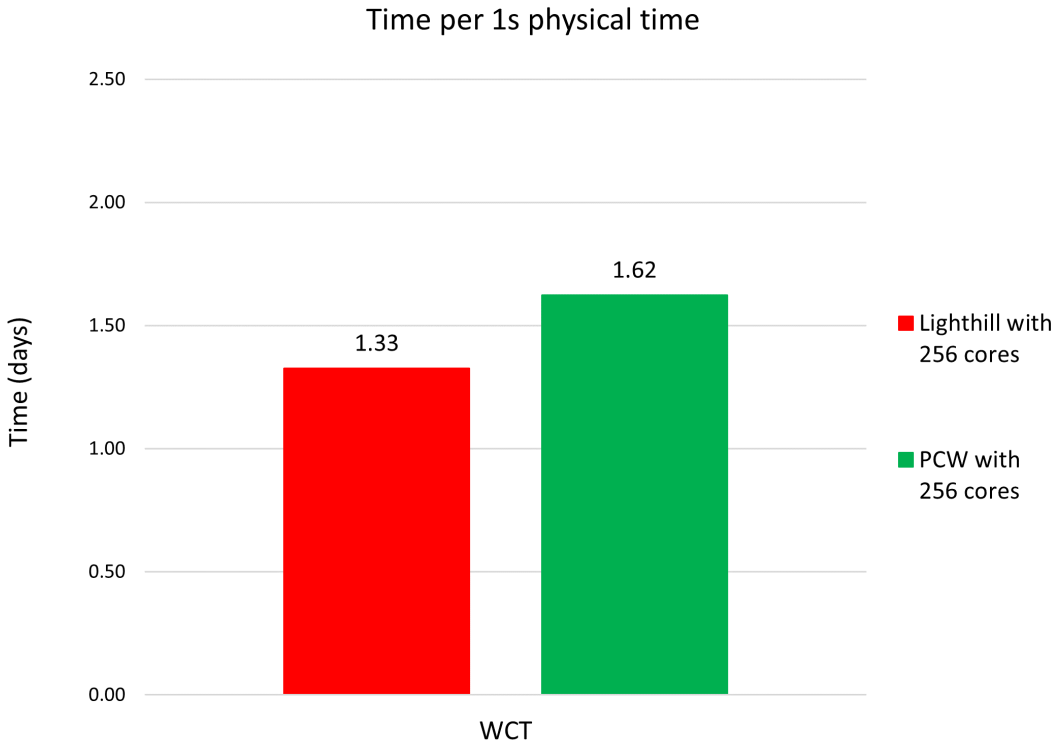

Figure 3.15: Wall clock time of Hybrid methods per 1s physical time

The activity made with DNC provided reliable results, both for aeroacoustics (up to 1000 Hz) and fluid dynamics. The latter has been taken as a benchmark to compare the fluid dynamics description obtained from the hybrid methods. For what concerns the aeroacoustics, the results obtained both from Lighthill and PCW setup have been compared with literature reference [7]. As stated in chapter 2.3, the experimental setup was provided of a matrix of probes to estimate the aeroacoustics behaviour of the simplified HVAC duct in the far-field, up to 2000 Hz. The results obtained from researchers were provided in the form of SPL plots, and from these the experimental curves have been extrapolated to be compared with the simulations' results.

As it can be observed from the figure 3.16, an average curve expresses the

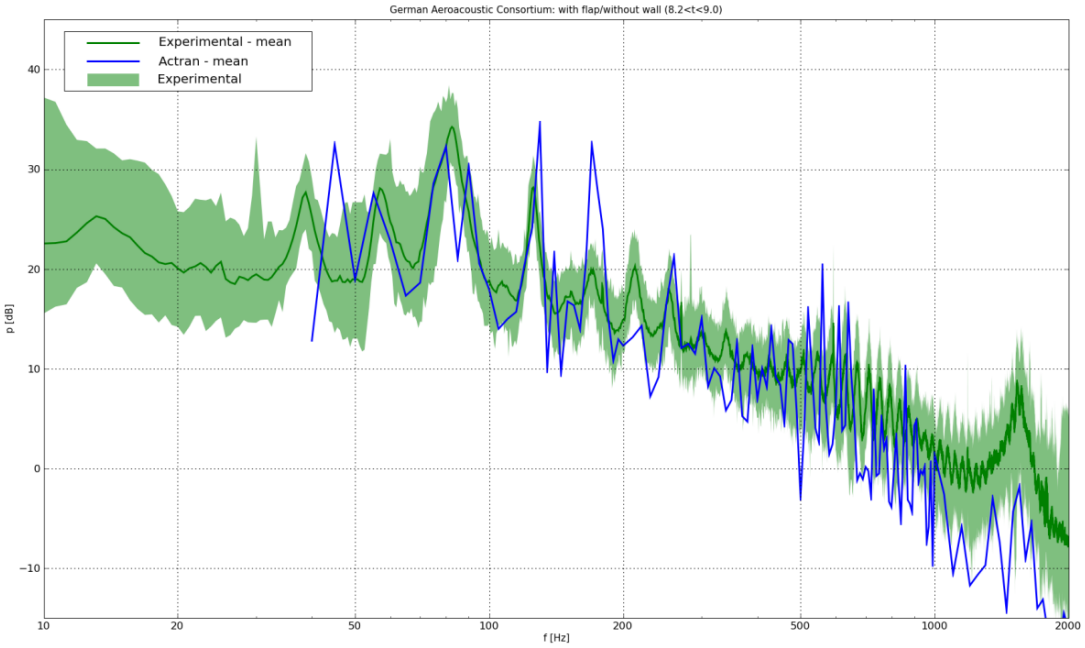

Figure 3.16: SPl plot from literature [7]

mean SPL curve, while a wide band identifies the overall range in which the SPL obtained from each microphone varies. For sake of simplicity, the upper and lower border of this band have been taken as a reference range in which the simulations' results should have been located. The upper border will be referred in the following sections as "Experimental High End", while the lower one as "Experimental Low End". No specific information was given about the weighting method adopted in literature research. The blue curve is referred to the simulations results coming from a different simulation software (Actrtan) [6] and it was not considered. In this project an area-averaged weighting method has been applied to the microphones' matrix. As stated in chapter 2.1, each microphone on the virtual spere surface had a specific surface portion assigned, and this area varied according to the coordinates of the probes' positions. The adopted script is presented in appendix A.1 and it has been developed on Matlab, where the signals of each probe has been uploaded and processed to obtain a single averaged curve for the entire matrix. The obtained curves had high spectral resolutions due to the high sampling time considered, so a further process to damp higher fluctuations needed to be adopted. To smooth out the curve, the algorithm in appendix A.2 based on zero-phase digital filtering was applied. It was based on a Butterworth low-pass filter which, according to a properly tuned cut-frequency, is capable of provide a less perturbated curve, which could be compared easily with experimental results.

3.2.1 Lighthill Method results

The hydrodynamic results in terms of time averaged velocity components were compared to DNC results, to understand if an accurate description was provided. To allow for an easier comparison, the results from DNC in terms of time-averaged velocity components, are presented again in figures 3.17 and 3.19.

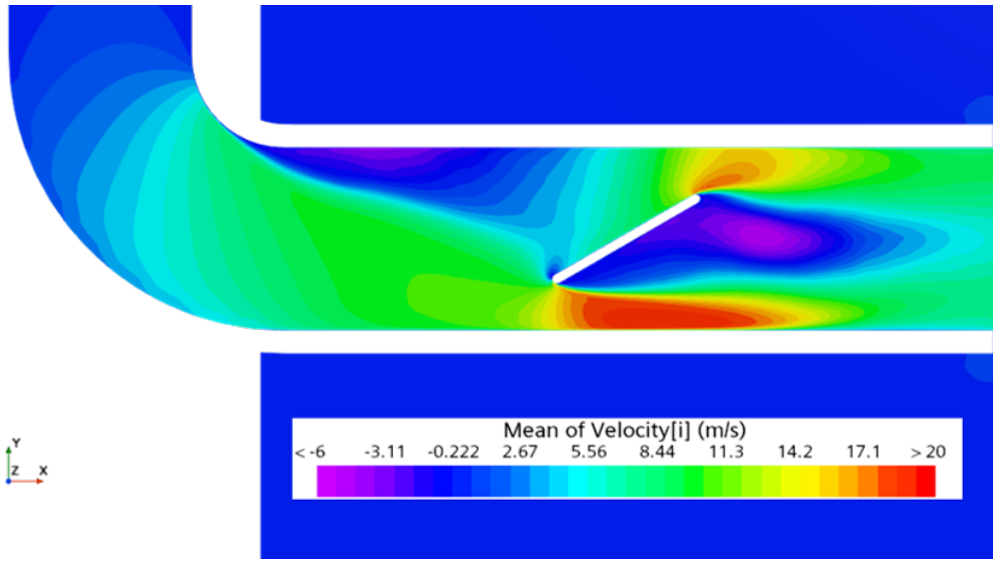

Figure 3.17: Time-averaged velocity component along the x-axis from DNC results

Referring to figure 3.18, where the time-averaged velocity component along the x-axis from Lighthill Model results is displayed, the flow description was closer between the two approaches, with slight differences related to the detachment area after the elbow. The recirculating zone was more marked and the negative velocity zone in blue, close to the bottom tip of the flap, was more intense. For what concerns the high velocity zone, no significant differences were appreciated. The same happened for the recirculating region behind the flap, which was described with high fidelity.

Considering the figure 3.20, where the component along the y-axis of the same field function is presented, some differences were observed for the detachment region, where the positive velocity zone after the elbow is less marked, and it was closer to the one observed in figure 3.3 for the powerFlow case in the literature example [3]. Moreover, the positive velocity zone over the flap surface was more intense, similarly to Star-CD results [6] in the same figure 3.3. The behaviour after the flap and the negative velocity zone correspondent to the lower tip of the flap were accurately described. The negative velocity zone right before the elbow was represented with a slightly higher intensity, again closer to the Star-CD result.

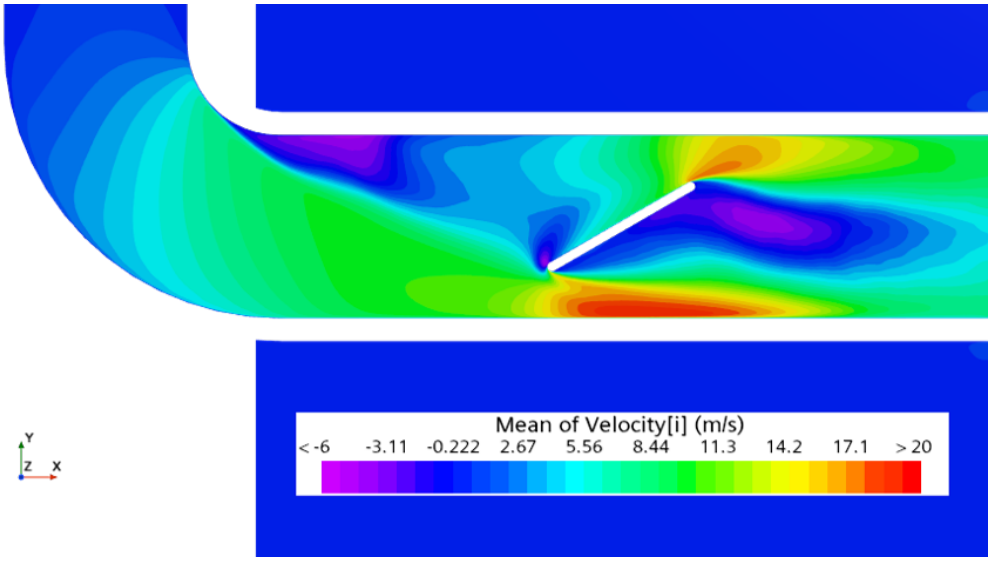

Figure 3.18: Time-averaged velocity component along the x-axis in Lighthill Method environment

However, these differences can be acceptable, considering that many aspects have been varied switching from DNC to Lighthill:

- The refinement area in Lighthill model was extended to fully describe the elbow.
- The refinement at walls and the layer cells generation method have been changed.
- The gas law in hybrid models has been switched to constant density low since it is a mandatory option to implements both the Lighthill Model and the PCW model
- The inlet boundary typology has been switched from freestream to velocity inlet.
- Being the figures time-averaged results, the averaging of different time ranges affected the results.

These aspects, combined with the high-fidelity of the aeroacoustics results that will be presented in the following sections, led to consider these results as reliable ones. Other than the fluid dynamics description, the Lighthill model allows to monitor specific functions related to aeroacoustics. At each of the 153 probes, the Lighthill Pressure was acquired, which is the acoustic term of the pressure perturbation equation 2.2. The Lighthill Pressure fluctuation monitored at each

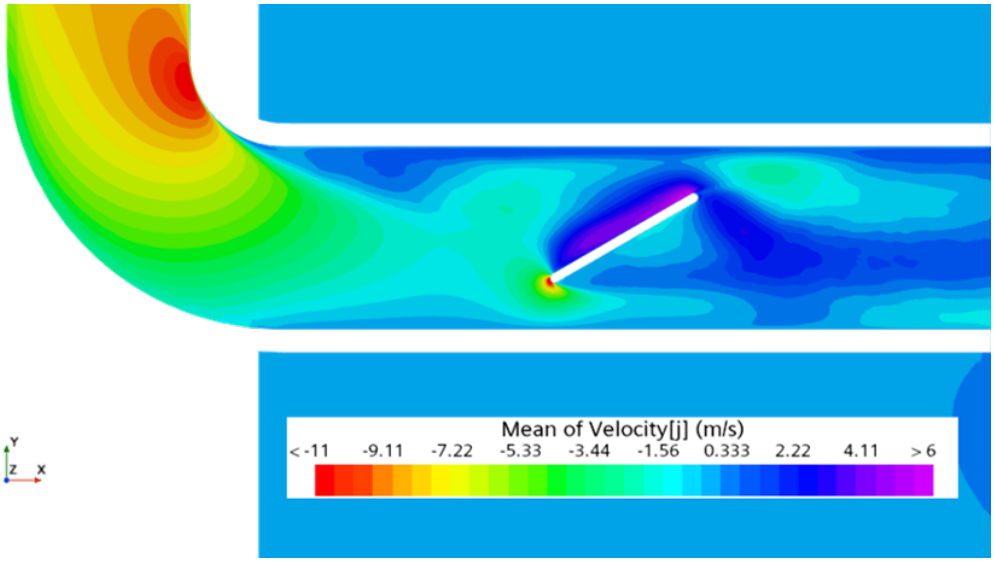

Figure 3.19: Time-averaged velocity component along the y-axis from DNC results

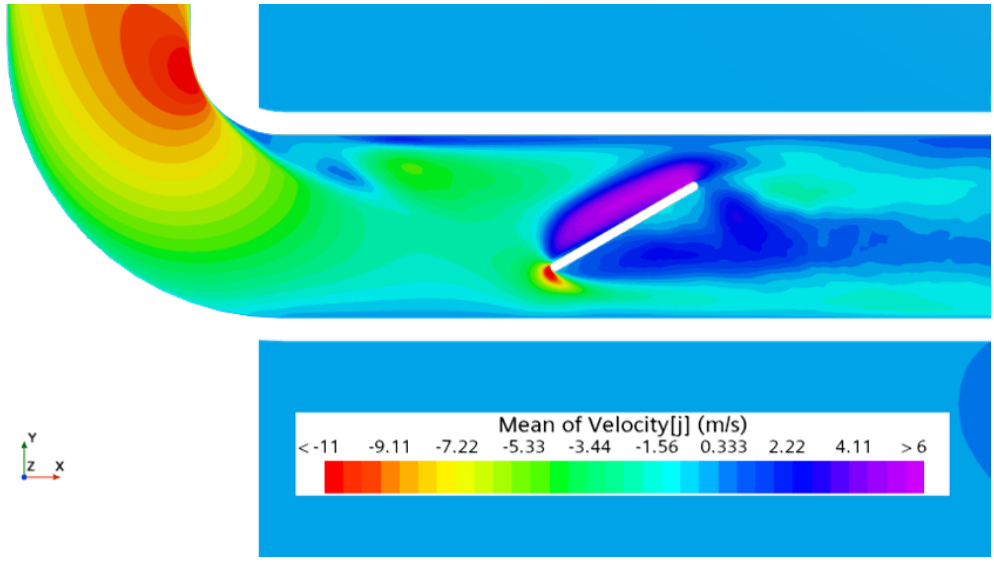

Figure 3.20: Time-averaged velocity component along the y-axis in Lighthill Method environment

probe was post-processed with the algorithm A.1 in Matlab environment, to obtain the SPL curves (coloured in red) in figures 3.21 and 3.22, with the frequency axis respectively in logarithmic scale and in linear scale. The Fast Fourier analysis for Lighthill (and PCW) was object of a sensitivity analysis, by trying a different

number of analysis blocks, and the leading to the final configuration:

- A sampling time of 1.5 s
- Hann window function
- 1 analysis block

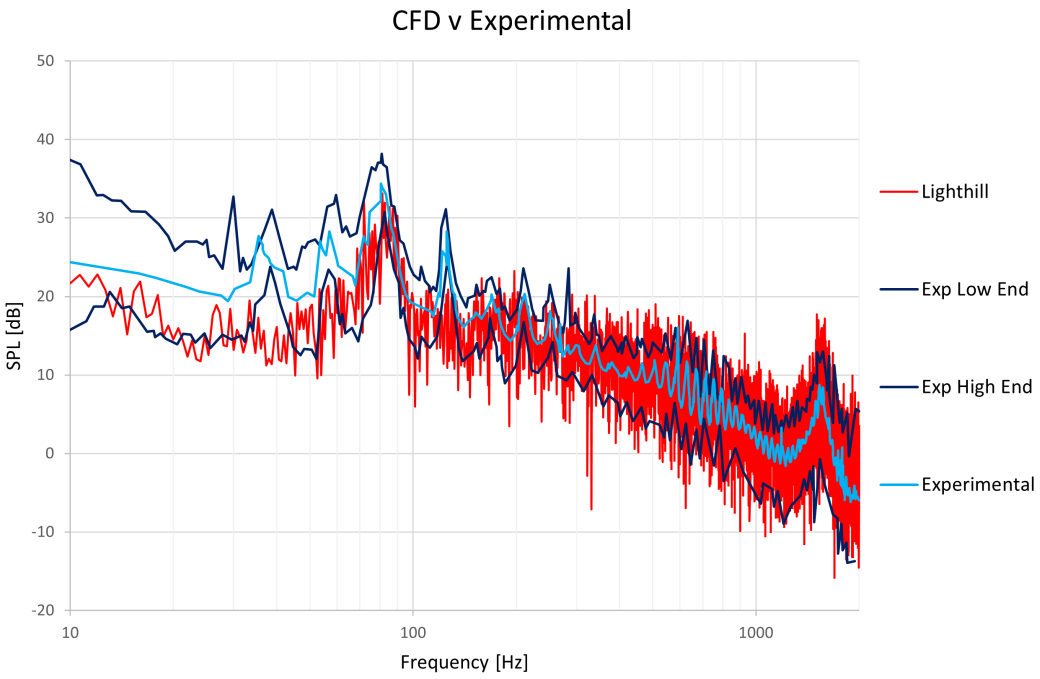

Figure 3.21: SPL plot with logarithmic scale on x-axis from Lighthill Method

Considering the red curves, a very high spectral resolution was obtained, which compromised the comparison with the experimental averaged curves. Since the spectra were examined over a range of 2000 Hz, the curves were plotted both with a logarithmic scale and a linear scale on the frequency axis, to help in the analysis of the different range of frequencies. In the plot with the logarithmic scale, it can be observed that in the frequency range below 100 Hz, the CFD results underestimate by 5-10 dB the sound pressure level, compared to the averaged experimental curve. Considering the figures 3.21 and 3.22, it is clearly visible how the CFD results fitted completely between the low end and high end of the experimental results. Then, to make the comparison easier, the zero-phase digital filtering algorithm, reported in appendix A.2, was applied with two different filter cut-frequency of 500 Hz and 100 Hz. Two different smoothed-out SPL curves are displayed in the figures 3.23 and 3.24. In both the figures it is observable how the CFD results followed closely the

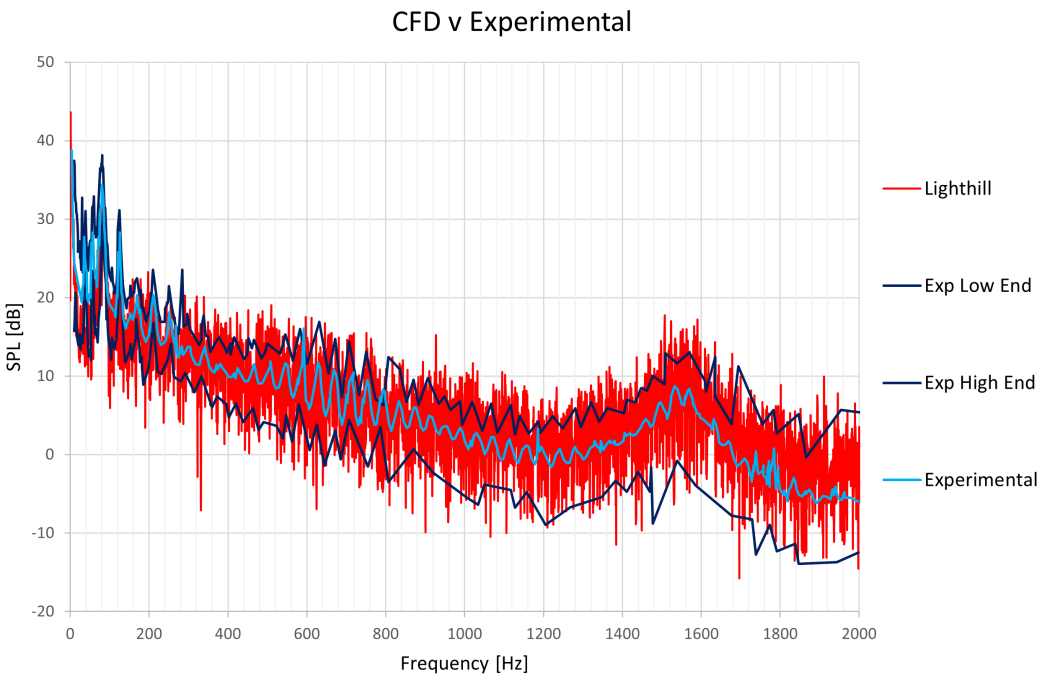

Figure 3.22: SPL plot with linear scale on x-axis from Lighthill Method

average experimental curve in all its descending and ascending trends, especially in the range between 800 Hz and 2000 Hz, that culminates with a peak around 1500 Hz and a final descending trend up to 2000 Hz. From the Sound Pressure Level point of view, the results confirmed the reliability of the methodology developed in the thesis project.

In figure 3.25 it is possible to observe the Lighthill Pressure Time Derivative, which is a field function that allows to understand the wave propagation inside the domain. As in can be observed in the picture, spherical sound waves propagated from the duct exit maintaining the spherical wavefront within a radius of 1 meter. Then, the waves were progressively disrupted by the coarse mesh, up to the end of the plenum. Within the direction of the duct exit, the influence of the hydrodynamic behaviour was observed, since here the Lighthill pressure term is not completely decoupled by the hydrodynamic term due to the presence of the flow turbulences. This aspect is the limiting factor for the aeroacoustics analysis with the Lighthill Model, contrary to what will be observed for the PCW in section 3.2.2, where the complete decoupling was achieved. The field function represented in figure 3.26 is the RMS value of the Lighthill Source that allowed to understand which portion of the geometry were responsible for noise generation at a specific dB value, properly set with an iso-surface. The figure represents the noise source at 70 dB.

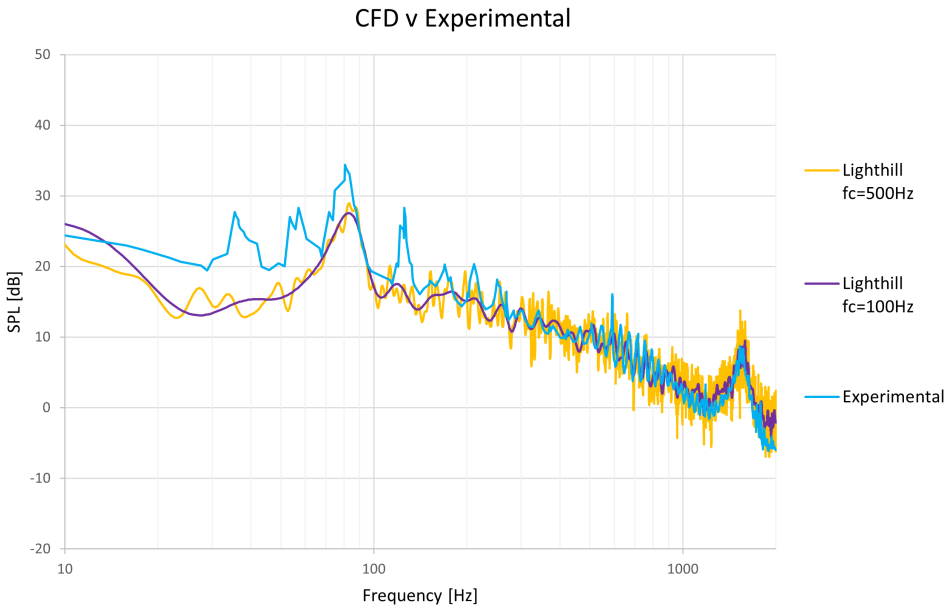

Figure 3.23: Smoothed-out SPL plot with logarithmic scale on x-axis from Lighthill Method results

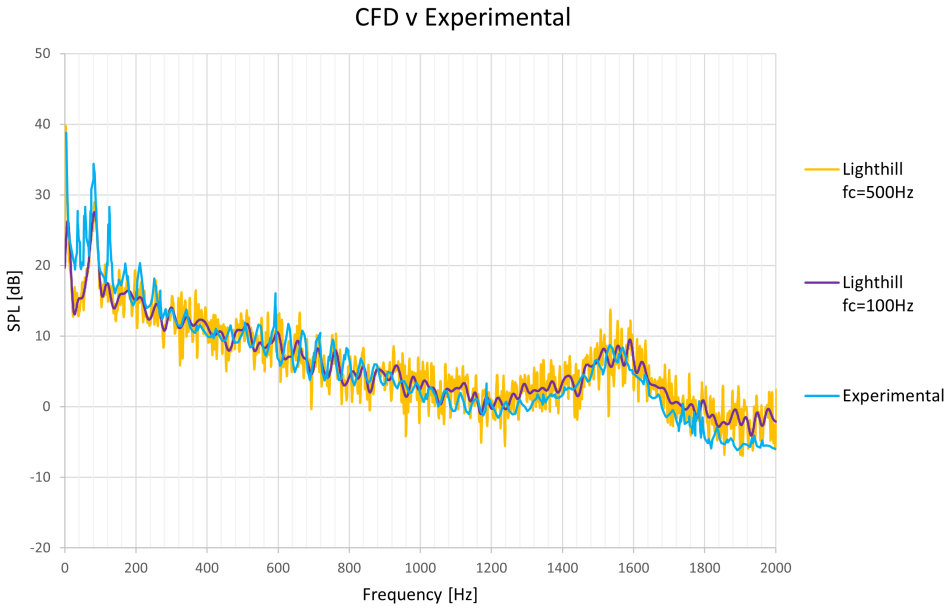

Figure 3.24: Smoothed-out SPL plot with linear scale on x-axis from Lighthill Method results

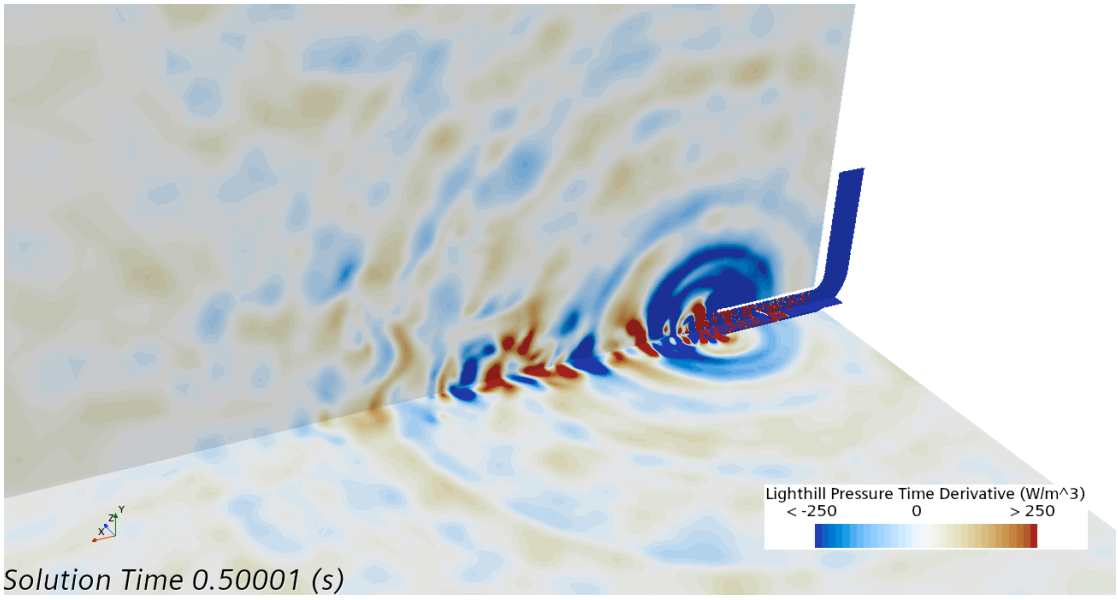

Figure 3.25: Lighthill Pressure Time Derivative at instant $t = 0.5s$

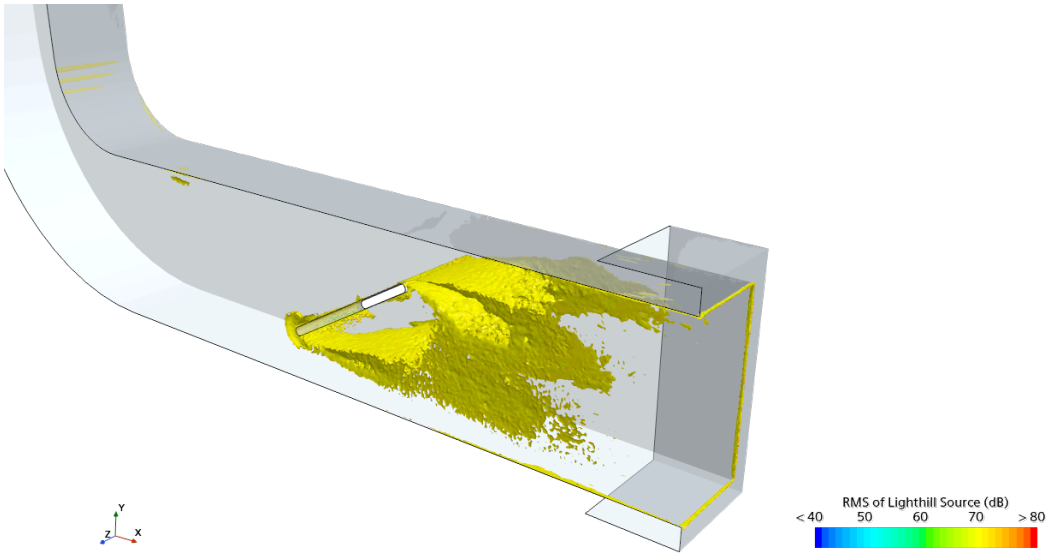

Figure 3.26: RMS of Lighthill Source at sound pressure level $SPL = 70dB$

Overall, the Lighthill Method allowed to obtain interesting results with a quite fast simulation, compared to the computational resources needed to perform a Direct Noise Computation. In fact, it should be considered that the DNC requirements in terms of mesh refinement to get a Mesh Frequency Cutoff at 2000 Hz, would be

unfeasible in terms of number of cells and, as a consequence, in terms of resource needed for computation. It has observed how the hydrodynamic behaviour inside the duct was described with sufficient reliability, but the aeroacoustics results in the far-field were more interesting from the aeroacoustics point of view than the measurements obtained inside the duct in DNC, since they were highly influenced by the hydrodynamics components.

3.2.2 PCW Method results

The perturbed convective wave model integrates more field functions that allow to comprehend better the noise generation at surfaces and to obtain a complete decoupling of the hydrodynamic term and the aeroacoustics term of the pressure perturbation. For the PCW results analysis the same strategy as the Lighthill case was followed. The pure hydrodynamic component was compared with the DNC results in terms of time averaged velocity components along the x-axis and the y-axis, as the pictures 3.28 and 3.30 demonstrates. To easy the comparison, the DNC results are presented again in the figures 3.27 and 3.29.

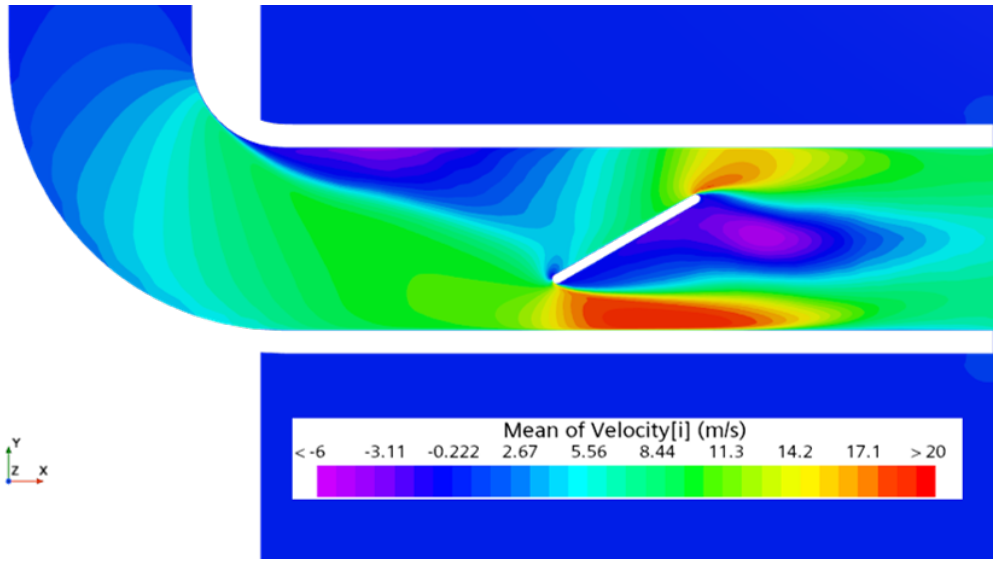

Figure 3.27: Time-averaged velocity component along the x-axis from DNC results

As expected, the time averaged velocity component results are close to Lighthill ones, therefore almost the same differences are observed compared to DNC. Referring to figure 3.28, the negative velocity zone right after the elbow was described correctly, however it was more persistent closer to the lower tip of the flap. For what concerns the high velocity zones at the flap tips, the results were in total accordance with

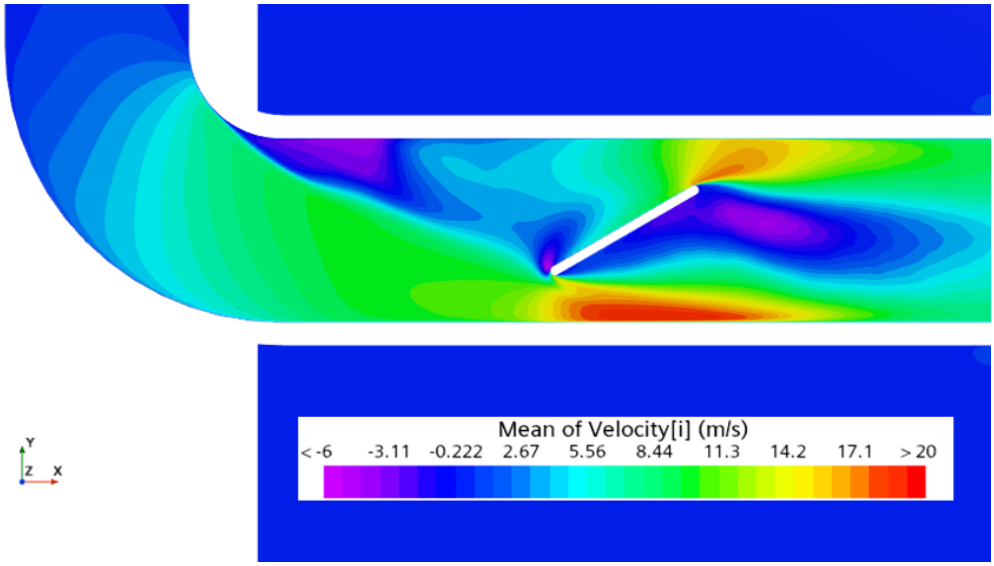

Figure 3.28: Time-averaged velocity component along the x-axis in PCW Method environment

DNC, and the same happened for the recirculating region downstream the flap. Considering the velocity component along the y-axis in figure 3.30, the main difference with DNC was related to the positive velocity region downstream the bend, where the PCW was less intensive than DNC, similarly to what happened with Lighthill Model. The positive velocity region on the flap surface was closer to DNC, more than Lighthill was and the behaviour downstream the flap was described appropriately. The reasons behind these differences were the same of the Lighthill case, hence the results were considered as reliable in accordance with what has been done previously.

For what concerns the sound pressure level spectra, the acoustic pressure has been acquired at each probe position. Then, all the signals were post-processed with the same area-averaging algorithm (appendix A.1) adopted for the Lighthill Pressure. Figures 3.31 and 3.32 shows the SPL results for the Perturbed Convective Wave model, both with logarithmic and linear scale on the frequency axis. To allow a further comparison between the two methods, the settings for the FFT analysis were uniformed to the Lighthill case. In figure 3.31 the range between 10 and 100 Hz shows that the PCW was not capable of get the SPL at probes, since they were completely underestimated. Instead, as it can be appreciated in figure 3.32 with the linear scale, the range after 100 Hz was properly described and the spectrum fitted within the range delimited by the experimental low and high ends. The curves that have been smoothed out showed great accordance with the averaged experimental curve for the entire range between 100 Hz and 2000

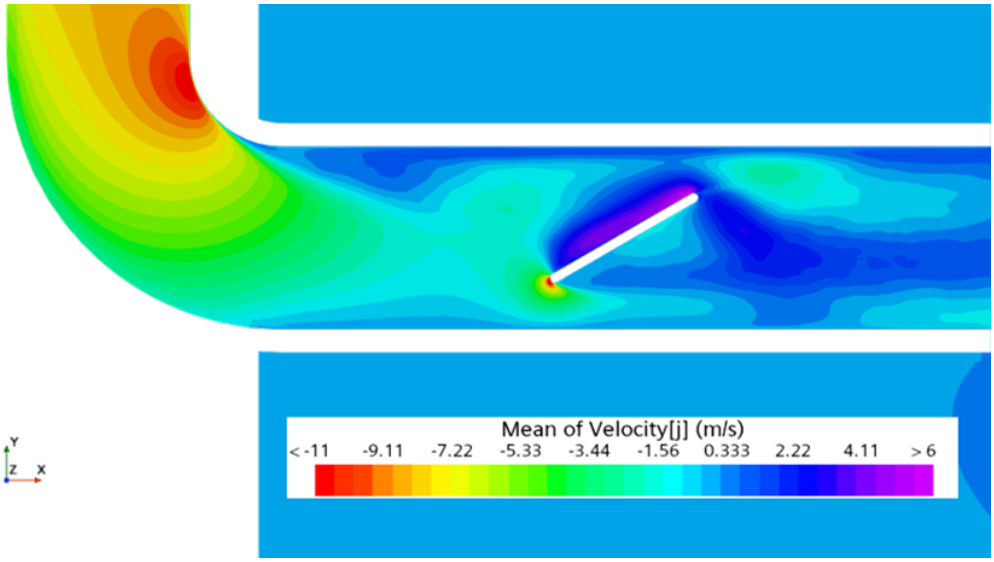

Figure 3.29: Time-averaged velocity component along the y-axis from DNC results

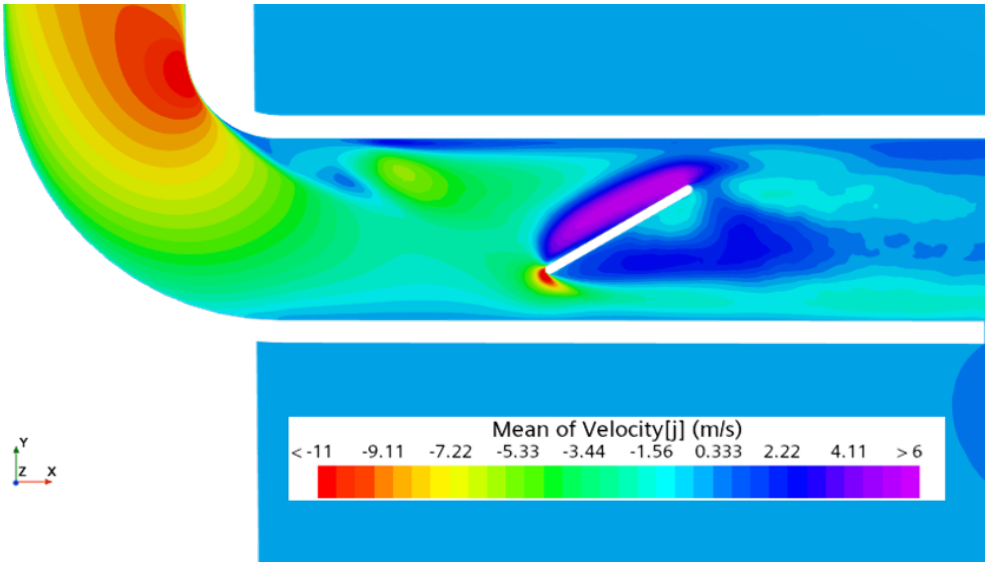

Figure 3.30: Time-averaged velocity component along the y-axis in PCW Method environment

Hz, with accurate description of the ascending and descending trends of the curve. Even though a non-negligible difference was obtained for very low frequency, these results were considered acceptable for the following reasons:

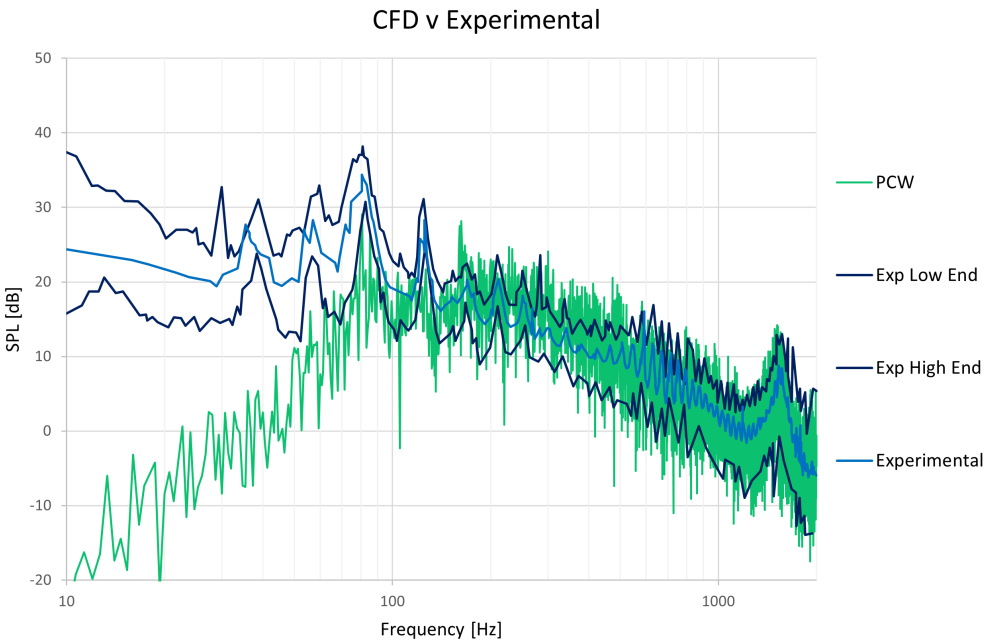

Figure 3.31: SPL plot with logarithmic scale on x-axis from PCW Method results

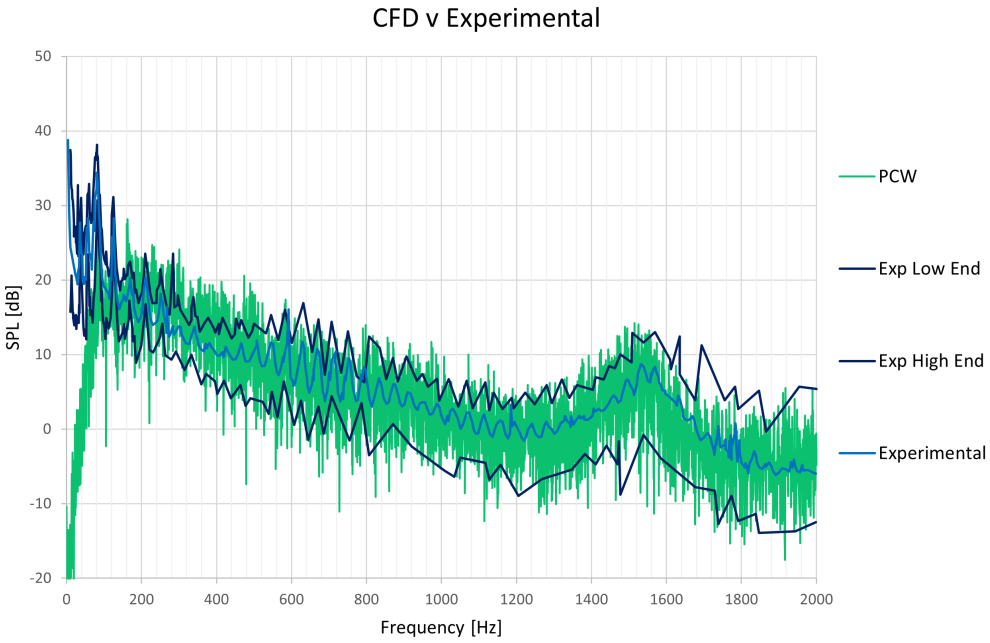

Figure 3.32: SPL plot with linear scale on x-axis from PCW Method results

- The thesis project target was to develop a methodology for the aeroacoustics analysis at high frequencies in the far-field, and the results showed high-fidelity over 100 Hz
- To study the high frequency range, the mesh and the setup of the simulation have been calibrated towards this direction and this aspect could have influenced the description at very low frequency.

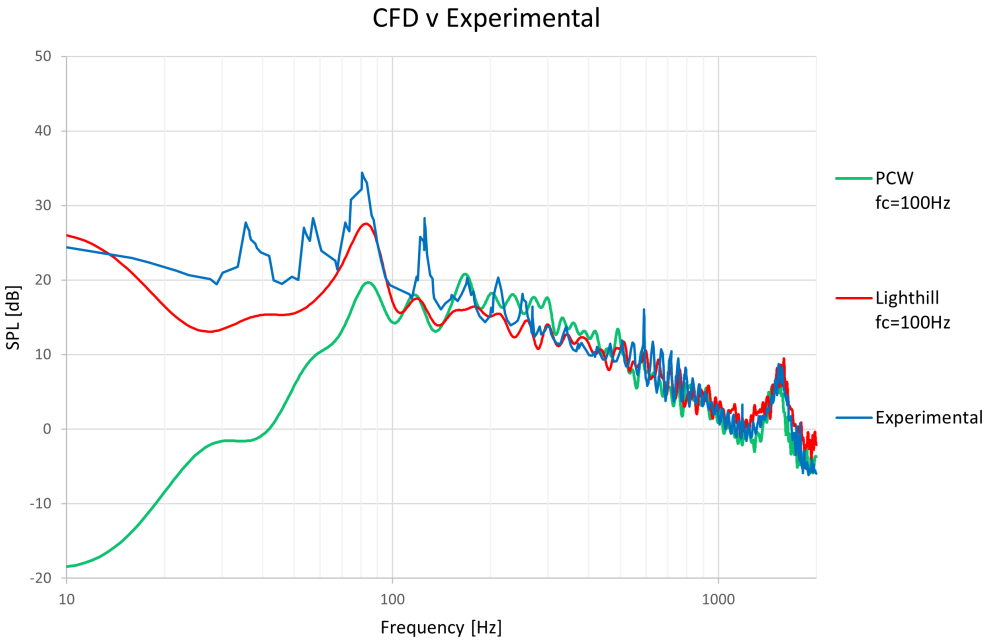

Figure 3.33: SPL comparison with logarithmic scale on x-axis

Therefore, the results were considered sufficiently accurate to validate the methodology with the Perturbed Convective Wave model. The figures 3.33 and 3.34 show a comparison of the Lighthill and PCW results in terms of SPL. To make the comparison clearer, only the averaged experimental curve and the smoothed-out curves from CFD simulations, with a cut frequency of 100 Hz, have been plotted. At low frequencies, the Lighthill model clearly showed higher accuracy. Instead, looking at high frequencies in the plots with linear scale on the frequency axis, the curves were closer. The PCW model presented higher accuracy in the valley between 1000 Hz and 1400 Hz and in the plateau description after 1800 Hz. However, the Lighthill model was more accurate in the descending ranges between 200 Hz and 1000 Hz and from the peak at 1600 Hz to the plateau at 1800 Hz. To summarize, these differences were estimated to the utmost within 2-3 dB for the PCW Method in the range [1500 Hz; 1800 Hz] and for the Lighthill Method in the

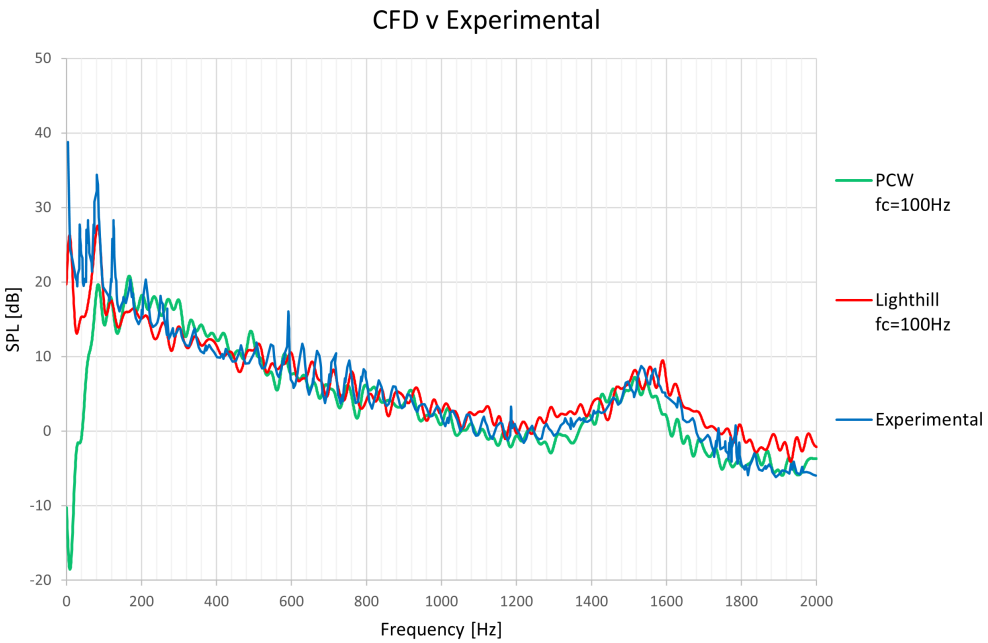

Figure 3.34: SPL comparison with linear scale on x-axis

range [1800 Hz; 2000 Hz]. Nevertheless, the overall trend was captured in both the cases, hence both the methodologies were considered reliable in terms of SPL evaluation.

The PCW approach allowed to monitor many field functions at cost of a reduced speed in simulation by 15-20% compared to the Lighthill model. Moreover, it performed a complete decoupling between the Acoustic Pressure and the Incompressible Pressure Fluctuation, which can be studied in the figures 3.35, 3.36 and 3.37. In the first two images related to the Acoustic Pressure, the spherical waves propagating from the duct exit were clearly observed and, contrary to the Lighthill model, no influence of the hydrodynamic pressure was present in the exit direction from the duct. The waves maintained the spherical form up to the end of the refinement area and then started to degrade towards the pressure outlet. In figure 3.36 the waves moving towards the inlet can be clearly observed. These waves were correctly let through the inlet boundary without any reflection, proving the efficiency of the default non-reflecting conditions for the flow boundaries. For what concerns the incompressible pressure term in figure 3.37, its development inside the duct was observed. It is clearly visible that the pressure fluctuation derived from turbulences of the flow were remarkable after the interaction of the latter with the flap.

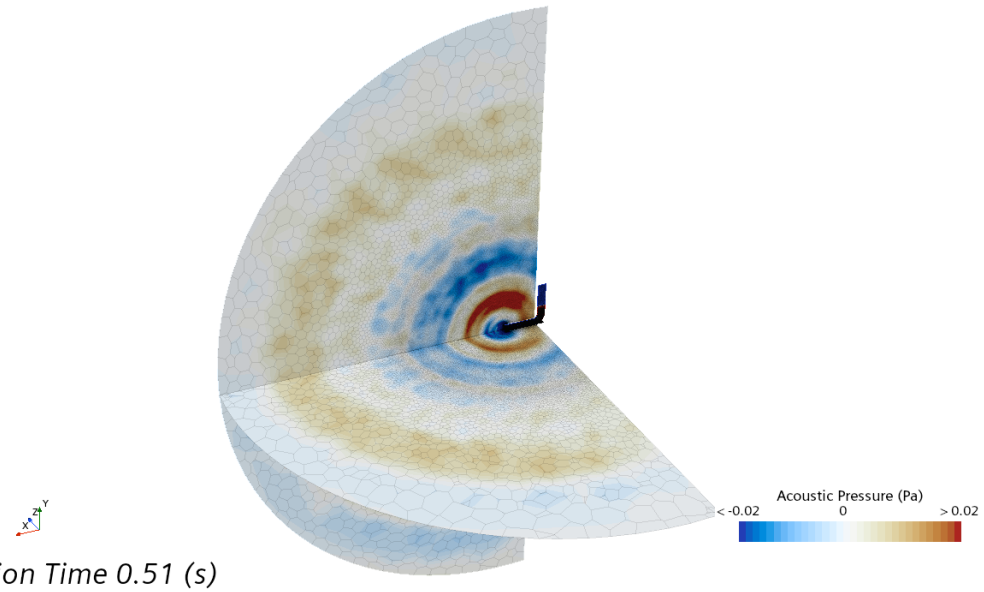

Figure 3.35: Acoustic Pressure inside the plenum from perspective point of view at $t = 0.51s$

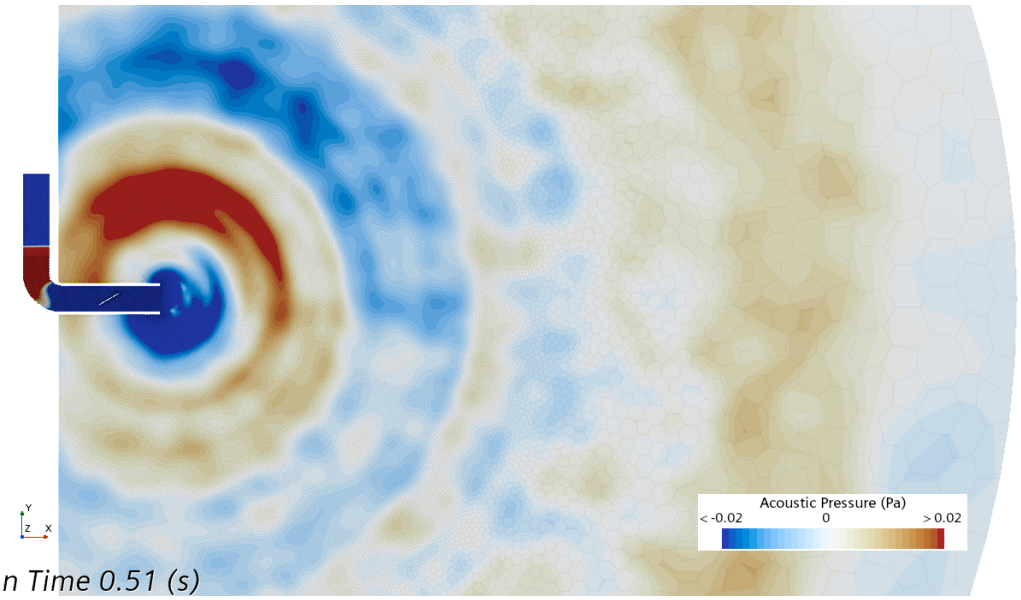

Figure 3.36: Acoustic Pressure inside the plenum on XY plane at $t = 0.51s$

Another field function that has been examined was the acoustic velocity, presented in figure 3.38, which expressed the zones inside the duct where the acoustic

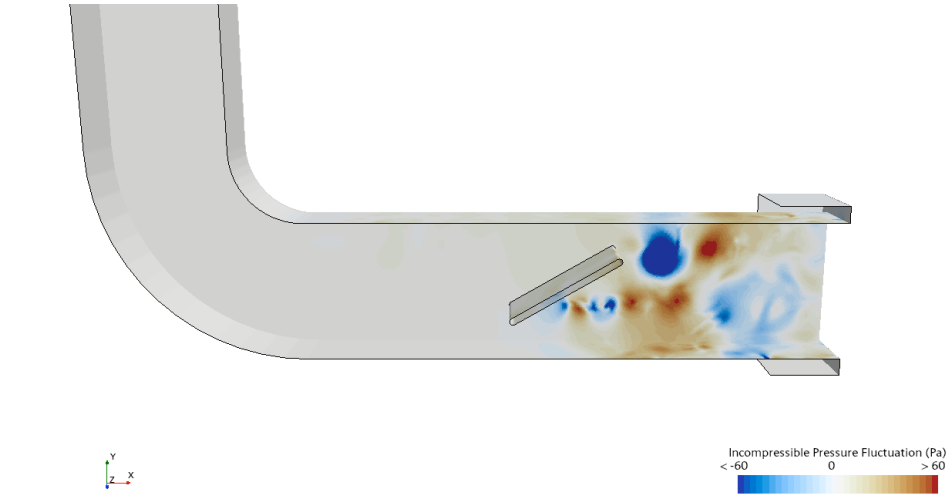

Figure 3.37: Incompressible Pressure Fluctuation at $t = 0.51s$

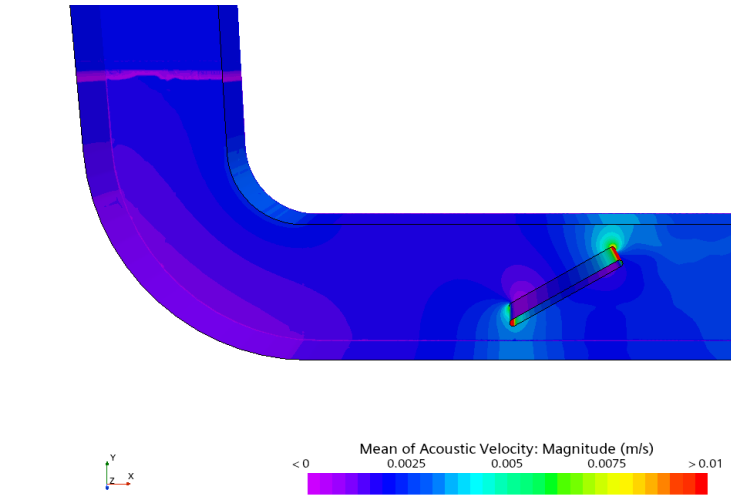

Figure 3.38: Mean of Acoustic Velocity at $t = 0.51s$

perturbation propagation was more significative. The mean value has been examined because it indirectly locates the zones on duct surface which are more responsible for the noise generation. From the early results obtained with this field function, it was understood the necessity to refine with higher accuracy the sharp edges of the duct and the flap surface.

The PCW model gives the possibility to actively monitor the acoustic source (figure 3.39) with a proper field function, and for the test case the internal duct

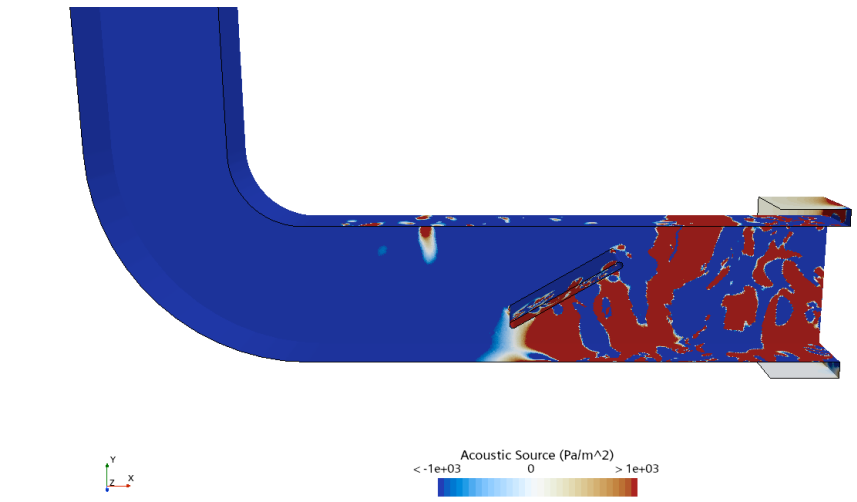

Figure 3.39: Mean of Acoustic Velocity at $t = 0.51s$

surface has been examined, to understand how the noise generation is distributed on the latter. Overall, the PCW allowed to perform a deeper aeroacoustics analysis with the available field functions, which were able to give useful information about the generation of the aeroacoustics phenomena, thus allowing further refinements and settings adjustments, which have been applied also on the Lighthill model setup, to improve its results.

Chapter 4

Conclusions

The aim of the thesis project was to develop a reliable methodology for 3D-CFD aeroacoustics analysis of HVAC systems, to improve the user experience in vehicle cabin and to guarantee proper comfort levels for drivers and workers inside the vehicle or tractor cabin. In particular, the main task was to provide a high-fidelity description of the Sound Pressure Level (dB) in the far-field, to emulate the real acoustic phenomena that develops over the distance between the vents and the head of the driver. Since it was focused on HVAC applications, the main prerogative behind the entire project was to work with flows at low Mach number, specifically not higher than 0.2, up to when the constant density law for gases can stand. The project explored also the noise generation at the surfaces of the examined HVAC duct, to understand not only how much noise is generated, but also which geometrical characteristics were relevant for noise generation. Therefore, the methodology target was being able to provide insights when adopted on a real test case and, eventually, to suggest design modifications.

The main drawback faced during the entire thesis project was related to the computational time and resources required, despite the geometry was a simplified version of an HVAC duct with a moderate number of cells (17.5 M for DNC, 8.3M for Hybrid models). Preparing the methodology to be implemented on a real test case, it comes that the main challenge faced in the development process was to find an optimum trade-off between computational resources requirements and the simulation accuracy. For this reason, the switch from DNC to hybrid methods has led to an important speed-up (in the order of days) alongside high-fidelity of the results, both in terms of fluid dynamics and aeroacoustics analysis.

As a consequence, the main focus during the project development was to calibrate a proper mesh setup, capable of capture all the desired results while being conservative in terms of total number of cells. This trade-off brought some issues especially for the DNC tests, where it was not feasible to extend the analysis to 2000 Hz, because of cores availability limitations. In fact, to refine the DNC mesh

to get a desired frequency of 2000 Hz, it would imply at least an halving of the adopted cell size in the refinement area, with the attempt to target 2000 Hz with the Mesh Frequency Cutoff. The effort requested was unfeasible considering the available resources. However, the DNC obtained significative results up to 1000 Hz, guaranteeing high-fidelity with literature results [6]. Moreover, it provided a reference for the successive tests with hybrid methods in terms of hydrodynamics description.

Switching from DNC to Hybrid Methods extended the possibilities for the aeroacoustics analysis, enabling a study in the far-field and putting the focus on the noise generation, thanks to the introduced decoupling between the aeroacoustics and hydrodynamics. The availability of reliable experimental results in terms of sound pressure level in the far-field [6] and an accurate fluid dynamics description from the DNC results, allowed to tune properly the setup for the hybrid methods. All the critical aspects related to the mesh description at surfaces and at edges where examined and proper countermeasures were found. Significative results were obtained from the sound pressure level point of view, alongside high-fidelity with the experimental results aforementioned. From the computational point of view, the speed-up compared to DNC was remarkable, since both the Lighthill Method and the PCW Method were able to provide significative results over 1 second of physical time in less than two days of simulation on 256 cores.

To conclude, the hybrid methods proved themselves to be very competitive in the field of 3D-CFD aeroacoustics simulations, providing important insights about noise generation and propagation, accurate results and optimizing the needs in terms of resources. To further validate the methodology, more investigations can be done on complex geometries and real production cases, to give an actual extent about the reliability of both the Lighthill Model and Perturbed Convective Wave Model when dealing with rotating geometries, porous media and complex HVAC architectures.

Appendix A

Appendix

A.1 Appendix A

```
%% import SPL at diffrent frequency at different microphones
addpath("path")
m=cell(153,1);
x=1502; %last row to read from the table which corresponds to the
    highest desired frequency

for i=1:153

    name_file = sprintf('Mic_%d.csv',i); %name of each probe
    table = readtable(name_file, 'Delimiter', ',');
    m{i,1} = tabella(1:x, :);

    m{i}{1,1} = 0.001; %correction of the first value 0 to be able
    to generate log plots
end


%% import microphone position

radius = 1; %sphere radius

addpath("path2")
pos = readtable('micpos.xlsx'); %matrix with microphones positions

%% spheric surface area partioning

% A = r^2 * deltaTheta * sin(theta) * deltaPhi
%where r = radius, phi is the angle on the latitude

deltaTheta = 0.1745329;
```

```
deltaPhi = 0.1745329;

A=table();

for i=1:153

    col1 = i; %theta
    col2 = (radius^2)*deltaTheta*deltaPhi*sin(pos{i,2}); %phi
    row = table (col1, col2);
    A= [A;row];

end
%% check on area

A_tot = sum(A{:,2}) %almost equal to 1/4 of a sphere

%% weighting of spl plots

spl = cell(153,1);

for i=1:153
    for j=1:x
        spl{i}{j,1} = m{i}{j,1};
        spl{i}{j,2} = m{i}{j,2}*A{i,2};

    end
end

%% sum of all the weighted spl at same frequency
frequency = zeros(x,1);
sum = zeros(x,1);
frequency= spl{1}(:,1);

for i=1:153
    for j=1:x
        sum(j,1) = sum(j,1) + spl{i}{j,2};
    end
end

W_spl = table (frequency, sum);

%% divide by the overall area to get the averaged curve

for i=1:x
    W_spl(i,2)=W_spl(i,2)./A_tot;
end

%% export table

```

```
writetable(W_spl, "area_averaged_SPL.xlsx");
```

Listing A.1: Area-averaging algorithm

A.2 Appendix B

```
%Signal smoothening script

addpath("path");
spectrum = readtable("area_averaged_SPL.xlsx");

freq = spectrum.frequency; %frequencies
dB = spectrum.somma; %dB

fc =500; %Cut frequency for butterworth filter

fs = 2*2000; %Sampling frequency (2000Hz) multiplied by 2

order = 10; %filter order

[b,a] = butter(order, fc/(fs/2), 'low'); %low-pass butterworth
   filter

smooth_dB = filtfilt(b,a,dB);

figure
plot(freq,dB,'b',freq,smooth_dB, 'r');
xlabel('Frequency [Hz]');
ylabel('dB');
title('Signal smoothing');
legend("D1-29-V12","D1-29-V12 Zero-Phase Filtering");

Smooth_D = table (freq, smooth_dB);
writetable(Smooth_D, "area_averaged_SPL_RESAMPLED_500.xlsx");

freqz(b,a,[],fs)

subplot(2,1,1)
ylim([-100 20])
```

Listing A.2: Zero-phase digital filtering

Bibliography

[1] European Environment Agency. «Transport and environment report 2022 Digitalisation in the mobility system: challenges and opportunities». In: (July 2022), pp. 12–33. DOI: 10.2800/47438 (cit. on pp. 1–3).

[2] European Environment Agency. *Infographics*. URL: https://www.eea.europa.eu/signals-archived/signals-2022/infographics (cit. on pp. 1, 2).

[3] International Energy Agency IEA. «Global EV Outlook 2024». In: (2024). URL: https://www.iea.org/reports/global-ev-outlook-2023 (cit. on p. 3).

[4] Noise Technical Committee ISO/TC 43 Acoustics Subcommittee SC 1. *ISO 5128:2023 Acoustics - Measurement of interior vehicle noise*. URL: https://www.iso.org/obp/ui#iso:std:iso:5128:ed-2:v1:en (cit. on p. 4).

[5] Matthias Tautz. *Aeroacoustic Noise Prediction of Automotive HVAC Systems*. FAU University Press, 2019 (cit. on pp. 4, 5).

[6] Anke Jäger, Friedhelm Decker, Michael Hartmann, et al. «Numerical and Experimental Investigations of the Noise Generated by a Flap in a Simplified HVAC Duct». In: *29th AIAA/CEAS Aeroacoustics Conference*. Vancouver B.C, May 2008 (cit. on pp. 5–7, 13, 14, 16, 17, 20, 24, 64, 67, 69, 72, 74, 75, 92).

[7] Stéphane Caro, Yves Detandt, et al. «Validation of a New Hybrid CAA Strategy and Application to the Noise Generated by a Flap in a Simplified HVAC Duct». In: *30th AIAA/CEAS Aeroacoustics Conference*. Miami FL, May 2009. DOI: 10.2514/6.2009-3352 (cit. on pp. 6–9, 16, 73, 74).

[8] Axel Kierkegaard, Alastair West, and Stéphane Caro. «HVAC noise simulations using direct and hybrid methods». In: *22nd AIAA/CEAS Aeroacoustics Conference*. May 2016. DOI: 10.2514/6.2016-2855 (cit. on pp. 6, 8–10).

[9] Christophe Bailly, Christophe Bogey, and Olivier Marsden. «Progress in Direct Noise Computation». In: (July 2010). DOI: 10.1260/1475-472X.9.1-2.123 (cit. on p. 19).

[10] Siemens. *Simcenter STAR-CCM+ User Guide* (cit. on pp. 20, 60).

[11] Joscha Piepiorka and Otto Von Estorff. «Numerical Investigation of hydrodynamic/acoustic splitting methods in finite volumes including rotating domains». In: *23rd International Congress on Acoustics*. Aachen, Germany, Sept. 2019. DOI: 10.2514/6.2016-2855 (cit. on p. 21).

[12] Jacopo Rossi Ferrini. «Development of CFD simulation methods to resolve acoustic characteristics of the flow». Master Thesis. Turin: Politecnico di Torino, Mar. 2021. URL: https://webthesis.biblio.polito.it/18286/ (cit. on pp. 36, 47).

[13] Cong Wang. «Numerical Investigation of Flow Induced Noise in a Simplified HVAC Duct with OpenFOAM». Master Thesis. Stockholm: KTH Engineering Sciences, 2013. URL: https://kth.diva-portal.org/smash/get/diva2:652385/FULLTEXT01.pdf (cit. on p. 36).